MEASUREMENTS WITH OPTICALLY LEVITATED MICROSPHERES

A DISSERTATION
SUBMITTED TO THE DEPARTMENT OF PHYSICS
AND THE COMMITTEE ON GRADUATE STUDIES
OF STANFORD UNIVERSITY
IN PARTIAL FULFILLMENT OF THE REQUIREMENTS
FOR THE DEGREE OF
DOCTOR OF PHILOSOPHY

Alexander Rider

May 2019

Abstract

I discuss the development of optically levitated microspheres as a tool for precision measurements and tests of fundamental physics. Micron-scale dielectric spheres are trapped by the radiation pressure at the focus of a Gaussian laser beam, where the optical suspension enables thermal, electrical, and mechanical isolation from the surrounding environment at high vacuum. Forces and torques can be measured from changes in the angle and polarization of light both transmitted through and reflected by the trapped particle. Additionally, the charge of the particle can be controlled with single electron precision. We have used these methods for the following three purposes: to search for fractionally charged particles and dark energy, to develop measurement techniques for surface potentials, and to construct an electrically driven micro-gyroscope.

Acknowledgments

I would like to thank my advisor, Prof. Giorgio Gratta, for giving me the opportunity to work in an excellent group that he filled with excellent people. Giorgio is a great advisor to work with because he is full of new ideas and cares about the quality of research. He enjoys actively participating in our research projects, and I am always impressed by his creativity and energy.

I joined the Gratta lab in June 2013 and began working on the optical levitation experiment with a postdoc, Dave Moore. Dave is an excellent teacher, and I have him to thank for many of my skills. Charles 'Chas' Blakemore joined the experiment in 2015 as a graduate student. Chas contributed a great deal to the experiments in the following chapters and it would be impossible to separate our contributions. Chas is the best. Akio Kawasaki came in 2017 as a postdoc and focused on developing the next version of the system. Nadav Priel and Alexander Fieguth, who arrived in the second half of 2018, have focused their efforts on improving the new system.

I would like to acknowledge other members of the Gratta group who helped me fit in and learn what it takes to succeed as a graduate student, including Karl Twelker, Scott Kravitz, and Dan Fudenburg. They taught me everything from how to use CF flanges to LaTeX. The postdocs Thomas Brunner, Igor Ostrovskiy, and Alexis Schubert taught me a lot and generally enriched my experience at Stanford. The machinists, Karlheinz Merkle, John Kirk, Mehmet Solyali, and Matthew Chuck helped me refine my machining skills and reminded me about shop safety (thanks to you guys I still have all my fingers!) as well as making many of the parts used in the following experiments. The staff at the Stanford Nanofabrication Facility (SNF), along with Qidong Wang from the Chinese Institute of Microelectronics (IME) taught me how

to fabricate the devices used in some of the following work.

A couple of Stanford classes greatly impacted my research and education. John Fox's analog electronics (AP 207) and digital electronics (AP 208) classes developed my understanding of electronics through hands-on experience and asking John many questions. The expertise that I gained from John was instrumental to the work in the following chapters. Bob Byer's modern optics (EE 268) and laser laboratory (AP 304) classes were also indispensable to allow me to develop the expertise required for the work in the following chapters.

Finally, I would like to acknowledge my family. My parents, David and Mary Rider, taught me curiosity and persistence that prepared me for a Ph.D. program. Thank you for your support during this time. My sisters Stephanie and Elizabeth helped teach me how to work with other people. And my wife Anna has given me the companionship, editing, and occasionally the kick in the butt I needed to produce the work in the following chapters.

Contents

List of Tables

List of Figures

Chapter 1

Introduction

1.1 Physics with Force Sensing

We can describe observations in terms of the four fundamental forces of nature: gravitation, electromagnetism, the strong nuclear force, and the weak nuclear force. Particle physics in the 20^{th} and 21^{st} centuries has focused on characterizing these interactions by producing and detecting particles. This approach has worked extraordinarily well for developing the Standard Model of Particle physics, which describes electroweak and nuclear forces.

Before the development of cosmic ray detectors and eventually particle accelerators in the 20^{th} century, experiments focused on characterizing interactions by measuring transfers of classical momentum. Due to the accessible length sales of electromagnetism and gravitation, these forces were the first to be characterized. Henry Cavendish famously used a torsion balance to determine the strength of the gravitational interaction and 'weigh the Earth' [2]. Electromagnetism was also first characterized by force sensing experiments when Coulomb used a torsion balance to determine the nature of the interaction between static electric charges [21]. At length scales longer than $\sim 10^{-8}$ m, force sensing experiments are still the most sensitive technique for laboratory experiments characterizing gravitational interactions.

Although the concept of characterizing interactions by measuring exchanges of classical momentum is old, there are still many important observations that can be

made by applying modern technology to improve force sensing experiments. The following thesis describes the development of force sensing techniques using optically levitated particles analogous to these foundational experiments.

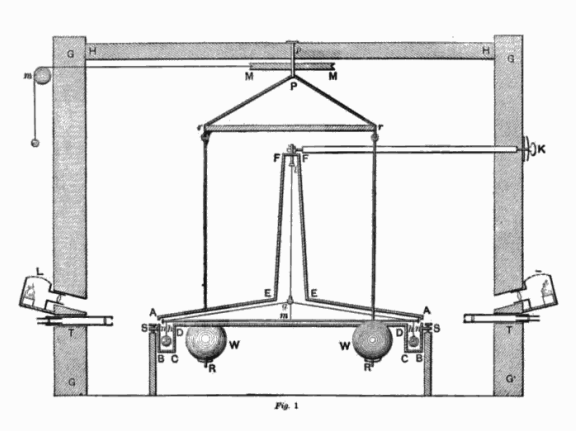

Figure 1.1: A cross section of the torsion balance used by Cavendish to weigh the Earth taken from Figure one of Ref. [2]. This measurement was the first laboratory measurement of a gravitational interaction. Two smaller 0.73 kg lead spheres are placed at the ends of a 1.8 m wooden rod suspended by a wire to form a torsion balance. Two larger 158 kg spheres are placed next to the smaller spheres to exert a gravitational force and twist the torsion balance. After measuring the torsional spring constant from timing the period of oscillation, Cavendish could infer the force of gravity by measuring the angular displacement of the torsion balance caused by the presence of the larger spheres.

1.2 Optical Levitation

In the canonical force sensing experiment, an interaction can be characterized by measuring the momentum transferred to a test mass. This procedure would be straightforward if it were not for Earth's gravity. Consider Cavendish's experiment testing the gravitational interaction between two 5 cm diameter, 0.73 kg lead spheres suspended on a torsion balance and two stationary 30 cm, 158 kg spheres. A schematic representation of the Cavendish experiment is shown in Figure 1.1. The gravitational interaction between the spheres is given by Newton's Law of Gravitation

$F_G = \frac{-Gm_1m_2}{r^2} = 1.7 \times 10^{-7}$ N. Compare this force to the strength of the gravitational interaction between one of the suspended spheres and the Earth $F_g = mg = 7.2$ N. The ∼8 order-of-magnitude difference between the interactions poses a challenge for laboratory experiments.

To overcome this immense difference in scale, a test mass must usually be suspended. For example, in atomic force microscopy, a tip is suspended by a silicon cantilever to detect the atomic interactions between the tip and a sample. LIGO must also suspend test masses at either end of an interferometer using fused silica fibers to detect the minute strain caused by gravitational waves. In both cases, the performance of the test mass suspension is a critical factor affecting the sensitivity of the entire experiment [22, 23].

Most experiments with test masses use mechanical suspensions, which tend to electrically, mechanically, and thermally couple a mass to the outside environment. An attractive alternative is to use radiation pressure from a laser to support a test mass. Light carries linear and angular momentum, which can be used to manipulate and suspend objects [24]. The linear momentum flux or force, carried by a laser beam is $\mathcal{P}_{opt}/c$ where $\mathcal{P}_{opt}$ is the optical power, and c is the speed of light [25]. Optical levitation and manipulation excel at micro-manipulation and has been applied to objects as diverse E. Coli and atoms [26–28].

In recent times, interest in optical levitation has grown for testing fundamental physics. Optically levitated microspheres have been suggested as a candidate system for performing quantum-limited measurements and ground state cooling [4, 29], as well as high-frequency gravitational wave detection [30]. Charged microspheres could also be used to measure deviations from Maxwell's equations caused by a photon mass [31].

This thesis shows the development of techniques with optically levitated test masses with the end goal of testing gravity at the micron-length-scale of the test mass. Application of optically levitated microspheres to gravity at these length-scales has been proposed in Ref. [32].

1.3 Testing Gravity

Of the four known fundamental interactions, gravity is the force that has been studied for the longest time. Nonetheless, there are substantial theoretical problems with our description of gravity which motivate experiments testing gravity in new regimes. Along these lines, the original goal of the work in the following chapters was to develop a technique to test gravity at micron length-scales.

Tests of gravity at micron length-scales are motivated by the fact that a microscopic theory of gravity is one of the most important open problems in fundamental physics. Although General Relativity provides a well-tested framework for describing gravity at large distances, it has not been combined with the Standard Model of particle physics to form a consistent microscopic theory of gravity. If a microscopic theory of gravity could be developed and tested, it would have profound implications [33, 34].

Many theories attempting to provide a consistent microscopic framework for gravity predict deviations from the inverse square law at a length scale shorter then 1 mm [34, 35]. Gravitational interactions are difficult to measure at these length scales because they are weaker than electromagnetism. For example, the gravitational attraction between an electron and proton in a hydrogen atom is $\sim 10^{40}$ times smaller than their electromagnetic attraction.

Forces arising from new theories of gravity [34, 35] are often parameterized by a Yukawa potential

$$V(r) = -\frac{Gm_1m_2}{r}\left(1 + \alpha e^{-r/\lambda}\right), \tag{1.1}$$

between two point masses. G is Newton's Constant, m_1 is the first point mass, m_2 is the other point mass, α is the strength of the interaction, and λ is the length scale of the interaction. There have been numerous experiments searching for Yukawa deviations from Newtonian gravity with λ ranging from cosmological to atomic length scales [36–40]. The excluded parameter space is shown in Figure 1.2.

The exponential scaling means that only mass within λ participates in the interaction, so that a test mass with length scale $r \lesssim \lambda$ placed within a separation $s \lesssim \lambda$ will experience the greatest acceleration from the interaction. For this reason Ref. [32]

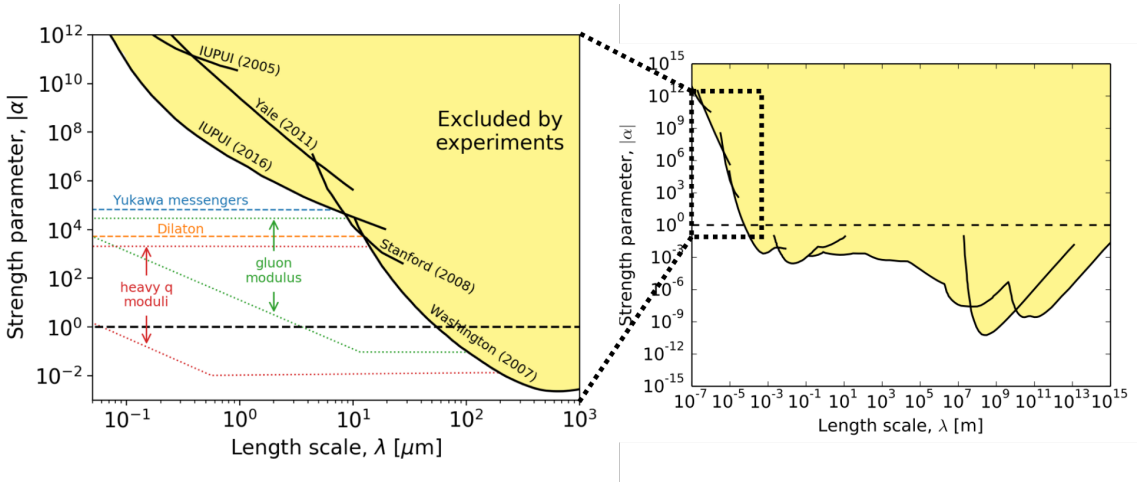

Figure 1.2: Right: The 95% exclusion limits for Yukawa deviations from Newtonian Gravity over length scales ranging from light years to 100 nm. The strongest constraints are at the length scale of the earth moon spacing from lunar ranging. Left: Detail of the sub-mm region of parameter space. Specific experiments and theories are noted.

proposes using ~ 1 μm optically levitated test masses to test deviations from gravity at the same length scale.

1.4 An Intuitive Picture of Optical Trapping

Optical trapping and suspension are only practical for relatively small objects. A fraction of the incident optical momentum flux in a trapping beam, $\mathcal{P}_{opt}/c$, is transferred to a dielectric object. This fraction is denoted by Q, the trapping efficiency. Q would be maximized for a perfect reflector with a value of 2 because the force on the mirror would be twice the incident momentum flux, while a perfect absorber would have $Q = 1$. The 2.4 μm radius spheres levitated throughout this work have an axial trapping efficiency close to $Q \sim 0.1$ [3]. With the trapping efficiency taken into account, balancing the force of gravity takes $\mathcal{P}_{opt} = c\,m\,g/Q$, where c is the speed of light, m is the mass, g is the acceleration due to earth's gravity, and Q is the axial trapping efficiency. Levitating an 85 pg dielectric sphere [41] then takes $\sim$2.5 mW

of optical power, which is easily achieved. It is interesting to note that the size of spheres that can be levitated is limited in practice by optical absorption, which causes silica microspheres larger than ~ 20 μm grown with the Stöber process to heat up and evaporate when levitated in vacuum [42].

While it is easy to show that a laser beam produces enough radiation pressure to levitate a small object, it is less obvious that the optical interaction should form a stable equilibrium. The interaction between light and dielectric particles is relatively easy to model in the limiting cases where the particle is either much larger or much smaller than the wavelength of light. When a dielectric particle is much larger than the wavelength of light, ray optics may be used, and when the particle is much smaller than the wavelength of light, the optical interaction may be treated as Rayleigh Scattering [43]. For the measurements in the following chapters, silica spheres with radii similar to the wavelength of light are used, so Mie Scattering Theory [44] must be used. A number of software packages exist to solve Mie scattering [3].

To illustrate the kind of computations possible with the software package discussed in Ref. [3], Figure 1.3 shows a simulation of the radial restoring force on a microsphere for conditions similar to those used in the following chapters. Some features of the optical trap are apparent. For instance, radial displacements less than 1 μm cause a restoring force proportional to the displacement of the microsphere, which forms a stable equilibrium well approximated by a harmonic potential. Non-linearity caused by radial displacements greater than ~ 1 μm has been observed in Ref. [45] in agreement with the simulation. Displacements larger than this do not necessarily eject the microsphere, but non-linear behavior is apparent. Uncertainty in microsphere and trapping beam parameters limit the utility of this simulation for making quantitative predictions. Computational limitations also make it difficult to determine how trap behavior scales.

It is possible to construct a simple qualitative model of the optical trap by viewing the microsphere as a convex lens which reflects, focuses, and deflects the trapping beam. While this idealization cannot be used to make exact quantitative predictions, it is useful for establishing how trap parameters scale, and providing intuition about how different traps and imaging schemes work. The optical processes important for

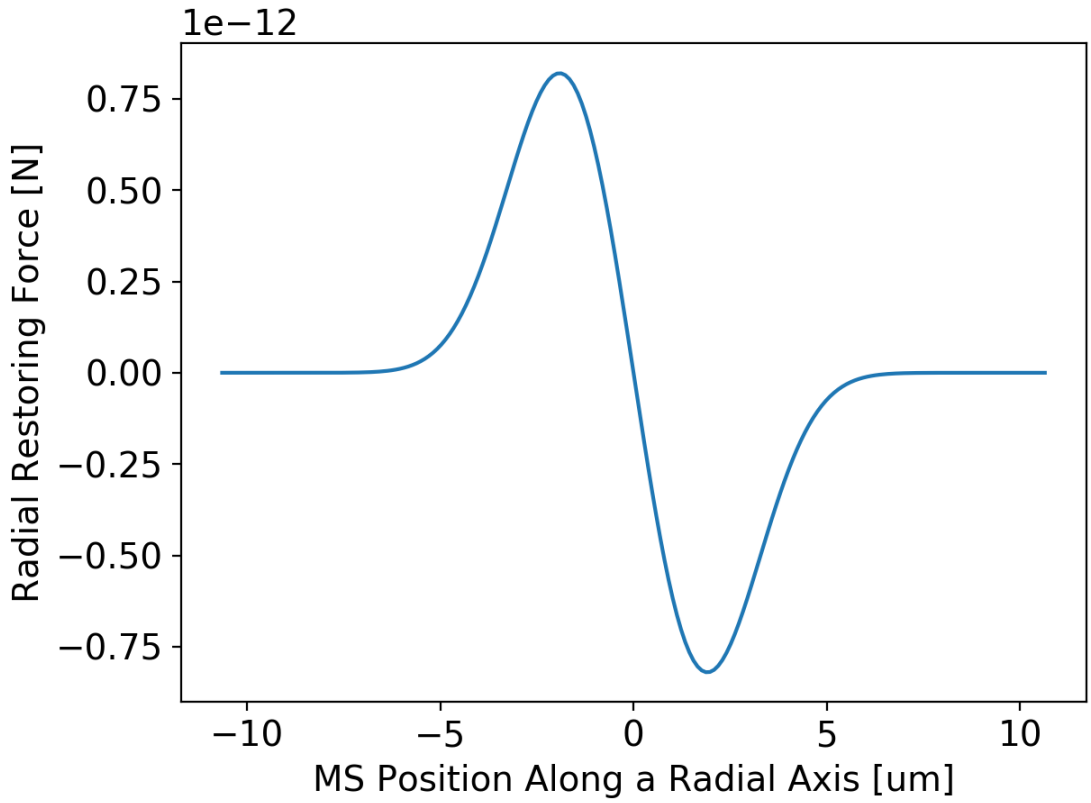

Figure 1.3: The radial restoring force on a 2.4 μm, n = 1.44 diameter microsphere at the focus of a 1.5 mW 1064 nm, 0.12 numerical aperture Gaussian beam computed with the software package discussed in Ref. [3]. These conditions are similar to the nominal conditions used in the traps discussed in the following chapters. In practice, uncertainty in the properties of the microsphere and trapping beam make the utility of this type of calculation limited.

trapping are illustrated in Figure 1.4.

The reflected beam is created by the change in index of refraction between the n≈1.3 microsphere [41] and the surrounding vacuum, which reflects $\sim$ 2% of the incident light. For the traps discussed in the following, the radiation pressure due to reflection is responsible for a significant fraction of the axial force. The force from reflected light is strong enough to push the microsphere out of the trap without the force from Earth's gravity serving as a counterbalance.

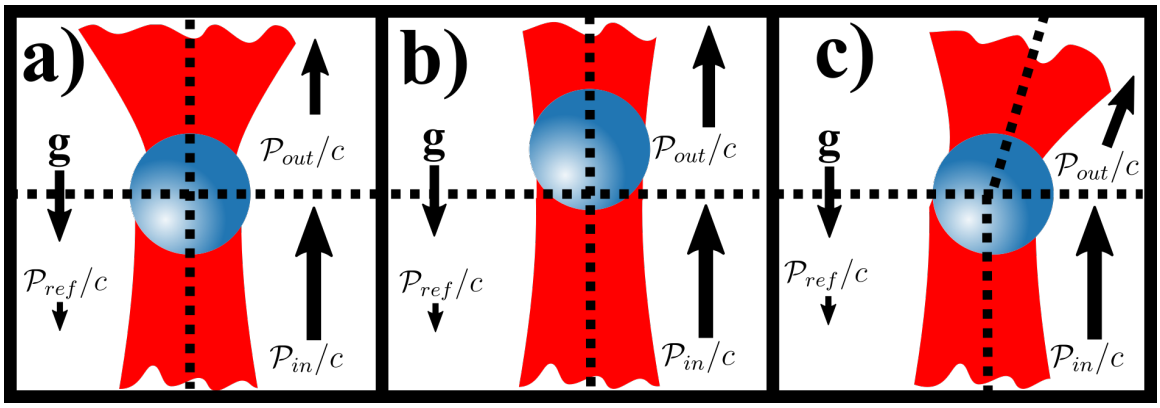

Figure 1.4: a) The microsphere at the equilibrium position. The radiation pressure is equal and opposite to the force of the Earth's gravity because the presence of the microsphere alters the axial optical momentum flux by reflection as well as changing the divergence of the outgoing laser beam. b) The microsphere is displaced upward which results in a decrease of the divergence of the outgoing laser beam, and an increase in the axial outgoing momentum flux. Since momentum is conserved, the increased optical momentum flux pushes the microsphere back to its axial equilibrium point. c) The microsphere is displaced from its radial equilibrium, which deflects the outgoing laser beam creating a radial optical momentum flux. Because momentum is conserved, the force paired with this momentum flux pushes the microsphere back towards the center of the beam.

As the microsphere moves in the axial direction, it acts like a lens and changes the focus and divergence of the transmitted laser beam, as shown in Figure 1.4 b). A collimated beam carries more optical momentum in the direction of propagation than a rapidly diverging beam of the same power. If the microsphere transforms the beam into one that diverges less, the difference in momentum flux must produce a force pushing back against the direction of propagation. The change in transmitted laser beam divergence, and therefore axial force, can create a restoring force and a stable axial equilibrium. However, this restoring force is often quite small relative to the radial restoring force and active feedback must be applied to fix the axial position of the microsphere.

Deflection of the transmitted laser beam caused by microsphere displacements forms a stable radial equilibrium. If the microsphere is displaced in one direction by

an amount Δx, the transmitted beam will be angled by $\Delta\theta \sim \Delta x/f_{ms}$ where f_{ms} is the effective focal length of the microsphere. The angled beam has a radial component with optical force $F_x = (\mathcal{P}_{opt}/c) \times \Delta\theta$. This force restores the microsphere back to the optical axis of the trapping beam with a radial spring constant $k_r = F_x/\Delta x = \mathcal{P}_{opt}/(cf_{ms})$, where $\mathcal{P}_{opt}$ is the trapping beam power, and c is the speed of light. It is interesting to determine the implied f_{ms}. The trap described in the following chapters has a resonant frequency $\omega_0 \sim 2\pi\times400$ Hz with a microsphere mass of 85 pg, which gives a radial spring constant $k_r = m\omega_0^2 = 5 \times 10^{-7}$ N/m with a levitation power of 1.5 mW. This gives a focal length of ~ 10 μm, which is twice the focal length expected from geometric optics for a spherical lens with the same radius and index.

1.5 Trapping Microspheres

In order to perform experiments, a microsphere must be placed where a stable equilibrium exists. This is complicated by two factors. The first is the small volume where a microsphere can be stably trapped. To achieve the radiation pressure required to support a microsphere, tightly focused beams with waists $w_0 \lesssim 10$ μm and Rayleigh ranges $z_R \lesssim 300$ μm are used, which define a trapping volume $V_{trap} \lesssim 100$ pL.

The second factor complicating microsphere trapping is the fact that microspheres have a large surface area per unit mass, which means that accelerations as great as $\sim 10^7$g are required to overcome the van der Waals attraction between a microsphere and a substrate. This acceleration can be estimated as follows. Atoms on a sphere with radius r_{ms}, within a distance r_0 of the substrate will bond to atoms on the substrate. For $r_{ms} \gg r_0$, this corresponds to a disc with radius $r_d = \sqrt{2r_{ms}r_0}$ of atoms on the substrate binding to the sphere. There are $N_b = \pi r_d^2/r_0^2 = 2\pi r_{ms}/r_0$ atoms in this disc. If we assume a binding energy E_{vdw} =0.1 eV, and a bond radius of $r_b = r_0$, then a force $F_{vdw} \sim N_b E_{vdw}/r_0 = 2\pi E_{vdw} r_{ms}/r_0^2$ will be required. For $r_0 = 1$ Å and r_{ms} =2.4 μm this corresponds to a 2.4×10^{-5} N $\sim 10^7$ g for 85 pg microspheres.

To overcome the small probability of catching an individual microsphere and the adhesion between the microspheres and a substrate, a microsphere catching technique

that used a piezo-electrically actuated glass substrate to suspend a film consisting of microspheres over the optical trap was implemented. The piezoelectric actuator was driven over a range of frequencies from 150-300 kHz sweeping through resonances of the glass substrate. On resonance, the glass surface could obtain accelerations sufficient to release a cloud of $\sim 10^4$ microspheres for the size and type of microspheres used in the following chapters. The probability of catching an individual microsphere was found to be ∼1-10% per cloud, depending on the conditions. The implementation of microsphere launching used in this work is shown in Figure 1.5.

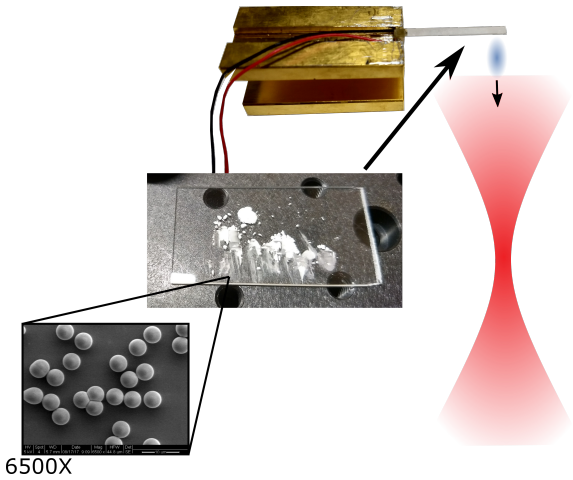

Figure 1.5: A schematic representation of our microsphere launching technique. The bottom left shows a high-resolution scanning electron microscope (SEM) image of 2.4 μm microspheres grown using the Stöber process. To the naked eye, these microspheres look like a white powder which can be adhered to the piezo-electrically actuated glass launcher with van der Walls forces. A cloud of $\sim 10^4$ microsphere can be released when the piezoelectric actuator is swept through a resonance of the glass substrate, which has a ∼1-10% chance of trapping a single particle at the focus of the laser beam.

1.6 Measuring Displacements

The same optics that form a stable equilibrium for a trapped particle can also be used to measure displacements. The canonical radial imaging setup is shown in Figure 1.6.

When an incident laser beam is directed onto a microsphere displaced by Δx, the transmitted light is deflected by an angle $\Delta\theta = \delta x / f_{ms}$, as discussed previously. This light is collected by another lens of focal length f_l, and imaged into a displacement $\Delta d = f_l \Delta\theta$. If this collimated beam is directed onto a segmented photodetector, where the radial displacement Δx can be inferred from the difference in photo-current between the left and right segments.

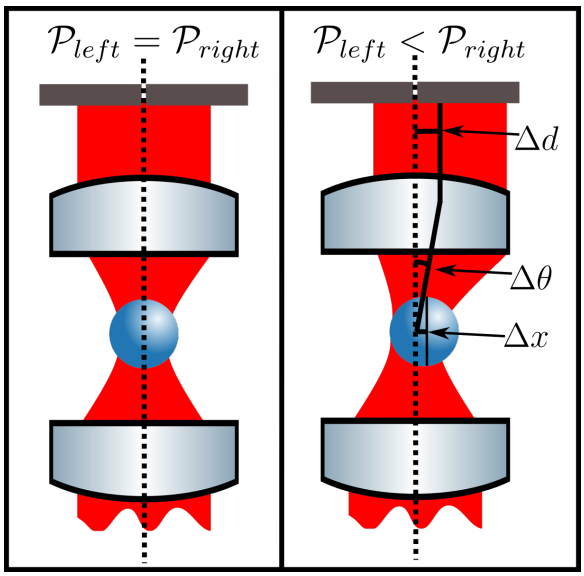

Figure 1.6: The microsphere to the left sets at the equilibrium position. Light transmitted through the microsphere is recollected by a lens and projected onto a segmented detector. When the microsphere is at the equilibrium position, the optical power is balanced between the segments of the detector. The microsphere to the right is displaced by Δx and the transmitted light is deflected by $\Delta\theta$. The light is recollected and the deflection produces a displacement of $\Delta d = f \times \Delta\theta$, which can be measured with a segmented detector.

There are several techniques that have been demonstrated for measuring the axial displacements of trapped particles. The technique used in Refs. [42, 46, 47] employed an auxiliary laser beam orthogonal to the main trapping beam to measure the axial displacements as radial displacements. The disadvantage of this technique is that it requires an auxiliary beam precisely aligned with the trapping beam. Furthermore, the auxiliary laser beam severely restricts the mechanical access to the trapped

microsphere and may contribute to backgrounds for precision force measurements.

The technique employed in Ref. [4] exploits the change in the divergence of the transmitted beam caused by axial displacements of the microsphere. As the divergence of the transmitted beam decreases, the transmission of light through a spatial filter after the trap also decrease, as shown in Ref. 1.7. This technique is good for high numerical aperture traps where changes in the axial position of the microsphere have a large effect on the divergence of the transmitted beam.

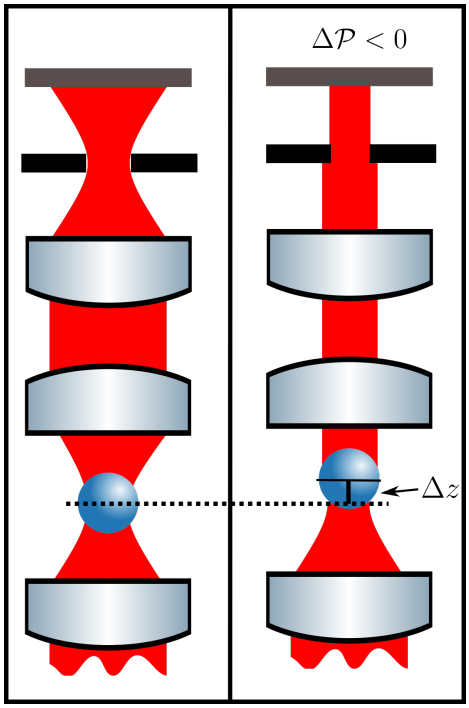

Figure 1.7: A conceptual demonstration of the axial imaging technique used in Ref. [4]. The light transmitted through the microsphere is collected and refocused by a pair of lenses. The transmission of light through an aperture is modulated by changes in the transmitted beam divergence. Axial displacements of the microsphere can then be inferred by measuring the transmitted power on a detector.

A third technique for measuring axial displacement was developed in Ref. [17]. This technique makes use of the beam reflected back by the microsphere by collecting the counterpropagating light with a Faraday isolator to form an interferometer with the microsphere at the end of one arm. Displacements of the microsphere can then

be measured from the change in optical path length of reflected light. This technique enables an axial position measurement which is referenced to the wavelength of the light and only requires a single beam.

1.7 Noise

Every measurement has sources of intrinsic and instrumental noise. For force measurements with optically levitated microspheres, intrinsic noise sources include thermal noise due to collisions between the microsphere and residual gas molecules, radiation pressure noise due to quantum fluctuations in the optical field holding the sphere, and imaging shot noise. These fundamental sources of noise are estimated in Ref. [29], and a detailed derivation of the thermal noise due to dissipation from residual gas is given in Ref. [18]. A detailed calculation of the shot noise for a version of the imaging system discussed in the following chapters is done in chapter 4. Sources of instrumental noise are numerous and poorly understood, but include electronics noise, laser power fluctuations, scattered laser light, and vibration. It is also possible that fluctuations in rotational and internal degrees of freedom could contribute to noise, particularly if the microspheres are not ideal uniform spheres.

1.8 Feedback Stabilization

In order to reduce the thermal noise due to collisions between residual gas and a microsphere, the trap is operated at high vacuum. This is complicated by the fact that optical traps become unstable when the dissipation from residual gas is removed [48]. Since the trap potential depth is finite, and there is a source of translational heating, the microspheres have a finite lifetime in the trap at high vacuum if there is no feedback stabilization. For the trap described in the following papers, the spring constant is $\sim 5 \times 10^{-7}$ N/m, and the trap size is ~ 1 μm. This implies a trap depth of $kx^2/2 \approx 1$ eV. Without the dissipation from residual gas, the lifetime of a microsphere in the trap is $\sim$10 s, which gives a $\sim$0.1 eV/s translational heating rate. Ashkin attributed this heating to thermal forces arising from temperature gradients across

the microsphere due to optical absorption [48–50].

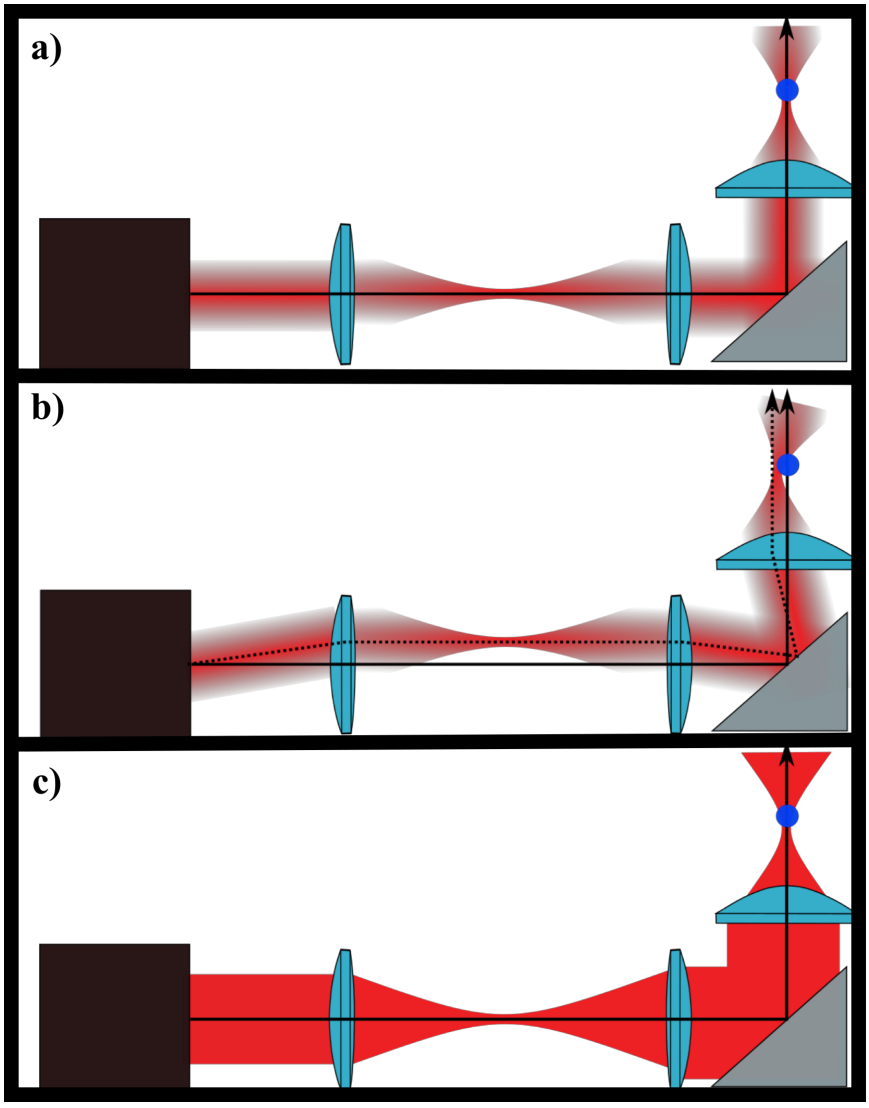

Figure 1.8: The feedback implementation used in the following chapters. An optical system represented by a black box can produce deflection and intensity modulation of the trapping laser beam. Radial feedback forces are generated by angling the trapping beam in the Fourier plane of the trap which produces a deflection in the trapping focal plane. Axial feedback forces are generated by modulating the power of the trapping laser beam.

Ashkin was the first to demonstrate feedback stabilization of a microsphere at high

vacuum pressures [49]. Since then, feedback stabilization and cooling of microspheres has been demonstrated in Refs. [1, 46, 51, 52]. An actuation force must be applied to remove energy from the microsphere for feedback stabilization to work. In Ref. [49] an electric feedback force was applied to charged microspheres, while Ref. [51] applied feedback forces with the radiation pressure from auxiliary laser beams. The following chapters use the feedback system shown in Figure 1.8 where radial feedback forces are applied by displacing the trap and axial feedback forces are applied by power modulating the trapping beam. This technique has the advantage that it can work on neutral particles and does not require additional beams.

Every feedback loop must be closed by calculating the appropriate feedback force from an error signal. In the following work, the feedback loop is closed by digitizing the displacement of the microsphere with an analog to digital converter (ADC) and digitally calculating the appropriate feedback force in a field programmable gate array (FPGA) sampling at ~ 500 kHz. Digital feedback offers flexibility that enables precise control of the feedback level and bandwidth in real time. In the following work, derivative feedback is applied to all three degrees of freedom to provide a dissipating force and stabilize the trap. The axial degree of freedom also receives proportional and integral feedback to fix the vertical position of the microsphere.

1.9 Overview of Applications of Optical Levitation

The following chapters show the development of optical levitation technology and applications of optical levitation to tests of fundamental physics. The first work demonstrates charge control of optically levitated microspheres and applies this to test the neutrality of matter [53]. After developing the ability to manipulate the charge of microspheres, stray electric field control was implemented by trapping the microsphere inside a Faraday cage. The Faraday cage enabled the search for the Chameleon interaction [47]. Next, a heterodyne imaging scheme was developed, which allowed three-dimensional imaging with a single laser beam with greater immunity to scattered light [17]. The removal of the auxiliary laser beam and rejection of scattered light made it possible to measure the electrostatic interaction between a charged

microsphere and 'patch' potentials on a gold film deposited on a nanofabricated device [45]. After the patch potential measurement, the rotational degrees of freedom of optically levitated microspheres were explored by applying torques using an electric field [54]. Finally, a calibration independent technique for *in situ* mass measurements of optically levitated microspheres was demonstrated [41]. The rest of this thesis discusses the advances in these areas by making ample use of previously published work written with the author's essential contributions.

Chapter 2

Search for Millicharged Particles

2.1 Statement of the Author's Contributions

This chapter closely follows what was published in Ref. [46]. The work shown here is important because it demonstrates charge control and operation of the trap at high vacuum pressures using feedback. The Author of this thesis played a role in all aspects of this work but made particularly significant contributions involved in developing the optical system used for actuating the microsphere, implementing the feedback calculation in the FPGA, designing the optomechanics inside the vacuum chamber, assembling the optical system, as well as collecting and analyzing the data.

2.2 Introduction

Millicharged particles, i.e., particles with charge $|q| = \epsilon e$ for $\epsilon \ll 1$, have been proposed in extensions to the Standard Model that include new, weakly coupled gauge sectors (e.g. [55]). It is possible that millicharged particles are a component of the universe's dark matter [56, 57]. If millicharged particles exist, they could have been produced in the early universe [58] and may have formed stable bound states that can be searched for in terrestrial matter today [5, 59].

Constraints on millicharged particles exist from astrophysical and cosmological

observations [60, 61] as well as laboratory measurements [62–66]. However, such limits are typically sensitive to the mass of the particles and do not provide significant constraints for particles with mass $m_\chi \gtrsim 1$ GeV [60]. In contrast, searches for millicharged particles bound in bulk matter are typically insensitive to the the mass of the new particle and can probe masses $\gg 1$ GeV, but suffer from significant uncertainty on the relic abundance in terrestrial materials. The terrestrial abundance depends on the binding and ionization rate of the particles in the early universe, as well as subsequent enrichment or depletion processes [59].

Previous bulk matter searches using magnetic levitometers [6, 67–69] or high-throughput Millikan oil drop techniques [5, 70–72] focused on searching for free quarks with $\epsilon = 1/3$, and did not have sensitivity to single fractional charges with $\epsilon \lesssim 0.1\ e$. In this work we present results from a search for particles with $\epsilon \gtrsim 10^{-5}\ e$ in bulk matter using optically levitated microspheres in high vacuum [73]. At high vacuum, residual dissipation of the microsphere motion from gas collisions becomes small, and measuring the motion of the microsphere in three dimensions allows extremely sensitive force detection [32, 73]. Previous work has demonstrated the trapping of microspheres in vacuum and cooling of the center-of-mass motion, which is necessary to keep the microsphere stably trapped at low pressures [1, 74, 75].

2.3 Experimental Techniques

We have developed a system for trapping and cooling dielectric microspheres with diameters $\gtrsim 1\ \mu$m in vacuum using a single, vertically-oriented laser beam [24, 51]. This optical setup allows long working distances between the focusing optics and trap location (few mm to few cm) and active feedback cooling of the microsphere's motion through modulation of the trapping laser intensity and position. This cooling is used to stabilize the microsphere in the trap once dissipation due to residual gas collisions is insufficient to balance the heating of the microsphere's mechanical motion by the laser [51].

A schematic of the experimental setup is shown in Fig. 2.1. A 300 mW diode laser ($\lambda = 1064$ nm) is spatially filtered and passes through a 2-axis acousto-optic

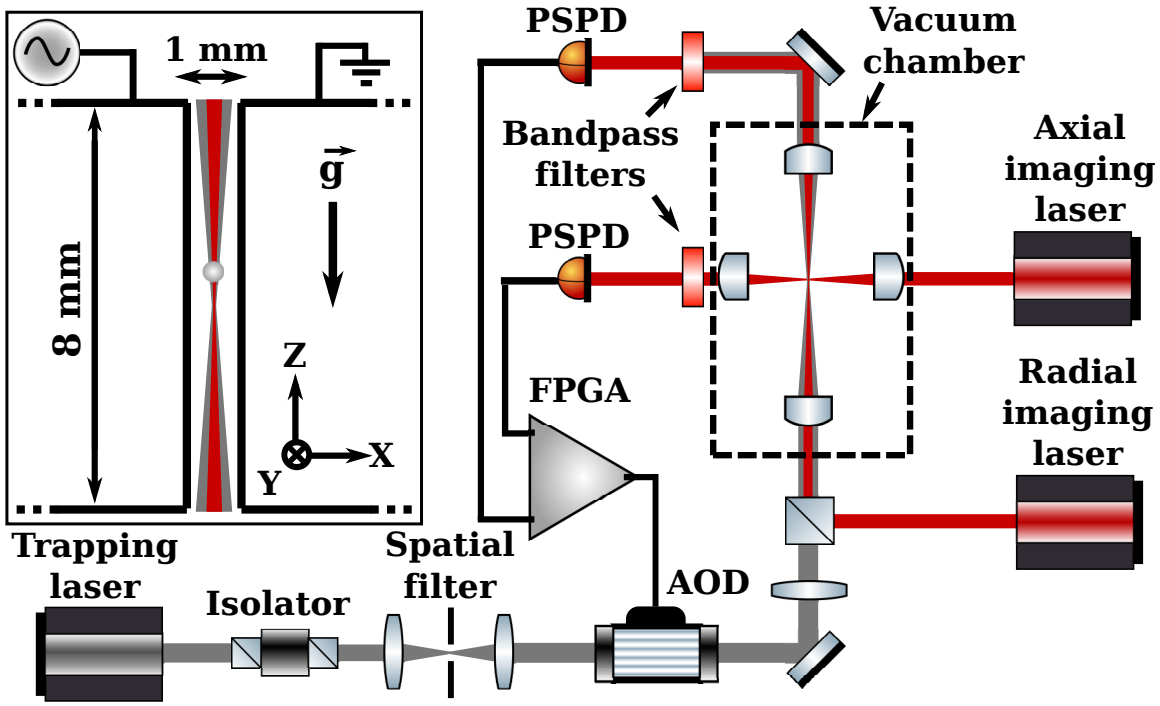

Figure 2.1: Simplified schematic of the optical layout described in the text. The inset (top left) shows a cross-section of the electrodes surrounding the trapping region.

deflector (AOD). Inside the vacuum chamber, the beam is focused and recollimated by a pair of aspheric lenses with focal lengths f=11 mm. The resulting optical trap is centered between the flat faces of two cylindrical electrodes with diameter $d = 8$ mm and separation $s = 1$ mm. Assuming an offset < 100 μm from the center of the electrodes, this configuration gives an expected electric field gradient at the microsphere location $|\nabla \mathbf{E}/\mathbf{E}| \lesssim 4 \times 10^{-4}$ mm^{-1} [76]. In the following discussion, we define X as the direction parallel to the electric field, while gravity points in the -Z direction.

Two 20 mW diode lasers ($\lambda = 650$ nm) are used to provide 3D imaging of the microsphere's position. The first of these lasers is co-aligned with the trapping beam after the AOD and passes through the same optics used to orient and focus the trapping laser. The transmitted light from this laser is imaged onto a lateral effect position

sensitive photodetector (PSPD) [1] to determine the position of the microsphere in the 2 degrees of freedom (DOF) perpendicular to the trapping beam axis (i.e. the X and Y axes). The second imaging laser passes through an orthogonal set of lenses and is used to image the position of the microsphere along the Z axis. A field programmable gate array (FPGA)-based feedback loop modulates the amplitude and steering of the trapping beam using the AOD, which allows feedback to be applied to all three orthogonal DOF. An additional lens is placed after the AOD such that deflections of the beam angle at the AOD provide displacements of the trap [77].

This work uses 5.06 ± 0.44 μm diameter silica microspheres (with masses, $m = 0.14 \pm 0.03$ ng) manufactured by Bangs Laboratories [2]. Microspheres are loaded into the trap in $\sim$50 mbar of dry nitrogen, where there is enough gas damping that the trap is stable without feedback. The microspheres are applied to the bottom surface of a glass cover slip positioned above the trapping region and a piezoelectric transducer is used to vibrate the cover slip, releasing the microspheres to fall under gravity [24, 51]. A small fraction of these microspheres fall through the trapping laser focus and become trapped.

Once a microsphere is trapped, the pressure in the chamber is reduced to 2 mbar and feedback cooling is applied. The pressure in the chamber can then be lowered to the base value of 2×10^{-7} mbar. We have demonstrated stable trapping of a single microsphere at this pressure for more than 100 hr. Although effective temperatures < 10 mK have been demonstrated for levitated microspheres in vacuum in our setup and elsewhere [1, 74, 75], cooling to $T_{eff} \sim 1$ K is more than sufficient for the force measurements presented here.

The minimum resolvable force in a 1 s integration is $\sigma_F = \sqrt{\sigma_{diss}^2 + \sigma_{im}^2}$, where $\sigma_{diss} = \sqrt{4k_B T_{eff} m\Gamma}$ [51, 73] denotes the corresponding fluctuations due to the total dissipation of the microsphere motion, Γ. Here k_B is Boltzmann's constant and m is the mass of the microsphere. The additional noise term, σ_{im}, denotes noise sources that are not associated with damping, such as imaging noise. When $\sigma_{im} \ll \sigma_{diss}$, the application of feedback cooling does not significantly affect the signal-to-noise of the

[1] Thorlabs PDP90A, http://www.thorlabs.com
[2] https://www.bangslabs.com/

measurement [78, 79] since both the signal and noise are attenuated by the feedback. In this case, if the dissipation, Γ, is limited by residual gas collisions, $\sigma_F \propto \sqrt{P}$ for gas pressure P [29]. For our measurements the force sensitivity is pressure limited for $P \gtrsim 10^{-3}$ mbar, while it is limited to $\sigma_F = 5 \times 10^{-17}$ N Hz$^{-1/2}$ at lower pressures by laser fluctuations and imaging noise. We are working to reduce these non-intrinsic sources of noise and reach pressure limited noise at 10^{-7} mbar, which is 2 orders of magnitude lower than the current sensitivity.

The microspheres typically have a net charge of 100–1000 e after loading the trap. To remove this charge, a fiber-coupled Xenon flash lamp is used to illuminate the electrode surfaces near the microsphere. Empirically we have found that UV flashes from the Xe lamp nearly always charge the microsphere in the negative direction, consistent with photoelectric ejection of e^- from the electrode surfaces. Hence, it is necessary to trap only microspheres with an initial net positive charge. When loading the microspheres directly from the glass cover slip, we have found that the initial charge is typically negative, but positive charges can be obtained by applying a thin layer of plastic between the glass surface and the microspheres (for these results, Scotch brand tape is used).

Once a microsphere is stably trapped at low pressure, an AC voltage with $V_{peak} = 100$ mV and $f = 40$ Hz is applied to the electrodes. The charge of the microsphere is inferred from its resulting motion while the Xe flash lamp is used to quickly reduce the net charge to $\lesssim +10$ e. While this coarse discharging is done with a voltage drive at a single frequency, the data at $< \pm 10$ e are taken with a broad frequency excitation to ensure that any observed signal has the correct frequency response. A frequency comb containing all prime integers between 20 and 200 Hz is used, which has good frequency coverage around the microsphere resonant frequency of $f \sim 150$ Hz. Since only prime frequencies are used, harmonics generated by potential non-linearities can be identified. After the microsphere has been discharged to a net charge $\lesssim +10$ e, the drive voltage is increased to $V_{peak} = 10$ V, which is sufficient to observe individual steps of 1 e in the microsphere charge with high signal-to-noise, but low enough that the microsphere is not pushed out of the trap (the measured trap depth is $\sim$1 eV). The microsphere is then slowly discharged to a net integral charge of 0 e, while calibrating

the signal amplitude at each charge step. Once the microsphere is neutralized, the voltage is increased to $V_{peak} = 500$ V to increase sensitivity to small residual charges, and data are taken for a total integration time $\tau \approx 5 \times 10^4$ s. Finally, the voltage is again reduced to 10 V and additional calibration data are taken as the microsphere is charged to $\sim -5\ e$. An example of this discharging and measurement process is shown in Fig. 2.2.

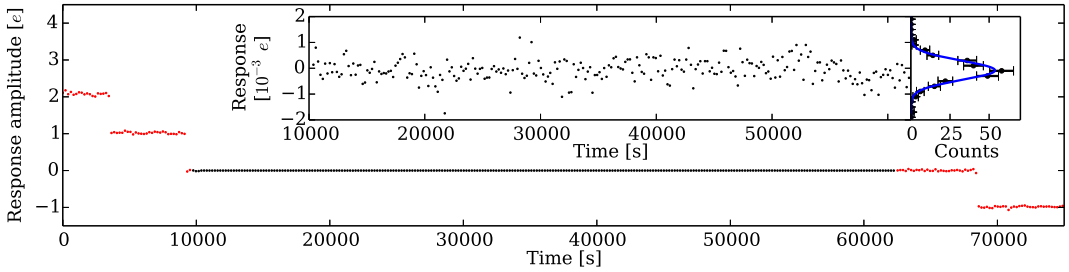

Figure 2.2: (Color online) Measured position response in the X direction versus time as a microsphere is discharged. The red (light) points show the calibration data at 10 V, while the black (dark) points indicate the data taken at 500 V with a net integral charge of 0 e. Each point represents the response to the drive measured in a single 100 s integration, after calibrating in units of e using the discrete steps observed during discharging. (inset) Zoomed-in view of the nominally neutral data and a Gaussian fit to the residual response.

For each data set, the X, Y, Z, and sum signals from the PSPDs are digitized at a sampling rate of 5 kHz using a 16-bit analog-to-digital converter (ADC). The drive signal is also directly recorded after passing through a resistive voltage divider with a measured gain of $(4.6 \pm 0.1) \times 10^{-3}$, and digitized on a separate 12-bit ADC to prevent electrical cross-talk to the position signals. A common trigger is used to synchronize acquisition of the drive and position signals, ensuring that the phase of the drive relative to the start of the data acquisition is identical for each 100 s cycle of the frequency comb. Data from each cycle are individually recorded to disk.

2.4 Data and Results

Data were taken for 10 microspheres to quantify variations between microspheres and to increase the total mass tested. The manual nature of the current loading sequence makes it impractical to measure a substantially larger number of microspheres. For each microsphere, the calibration data taken at a residual charge of 1 e are used to determine the expected response to the drive signal, which includes both the transfer function of the microsphere's motion in the trap as well as any effects of the readout electronics on the measured position response. The amplitude of the response for each 100 s cycle is then estimated using the optimal filter constructed from this response template [80]. This amplitude estimator is applied to the data at each net charge, and the measured single e steps in the response are used to calibrate the residual response for each microsphere. The amplitude estimator is linear within 5% for response amplitudes $\leq 5\ e \times 10$ V, so non-linearity in the response is negligible for the smaller residual motion of a neutral microsphere driven at 500 V.

The residual response measured at a net integral charge of 0 e for each of the microspheres is shown in Fig 2.3. Roughly half of the microspheres show a statistically significant residual of $(10-100)\times10^{-6}\ e$, while the remaining microspheres show a larger response of $(100-1000)\times10^{-6}\ e$. For the microspheres with measured residuals $\lesssim 100\times10^{-6}\ e$, this response is found to vanish when the electrodes are grounded at the input to the vacuum chamber, but all other wiring connections are identical. The residual also vanishes when the drive signal is connected to the electrodes but there is no microsphere in the trap. These checks indicate that the residual responses from $(10-100)\times10^{-6}\ e$ are likely to result from actual motion of the microspheres in the trap due to the drive voltage. However, this motion differs from the calibrated response of a microsphere with a net charge $\sim 1\ e$, being typically offset by $45-90°$ relative to the direction of the electric field. In contrast, the calibrations for all microspheres with charges between $\pm10\ e$ align with the nominal direction of the electric field within $< 5°$, limited by residual misalignment of the imaging axes to the field. For the microspheres with larger measured residuals, in some cases the residual response does not completely vanish when the microsphere is removed from the trap,

suggesting that the residuals may be at least partly due to cross-talk from the drive signal to the position measurement.

Given the misalignment of the microspheres' motion relative to the expected response, the measured residuals are not evidence of a net residual fractional charge. Such residuals could be consistent with a permanent, microsphere-dependent electric dipole moment that couples to the translational DOF through asphericities or other inhomogeneities. Future work may allow the reduction of this residual by spinning the microspheres around the Z-axis at high frequency, averaging over inhomogeneities [6]. The residual motion varies with each microsphere, and provides a systematic limit to the sensitivity to small charges that dominates the statistical error for integration times $\tau \gtrsim 10^3$ s.

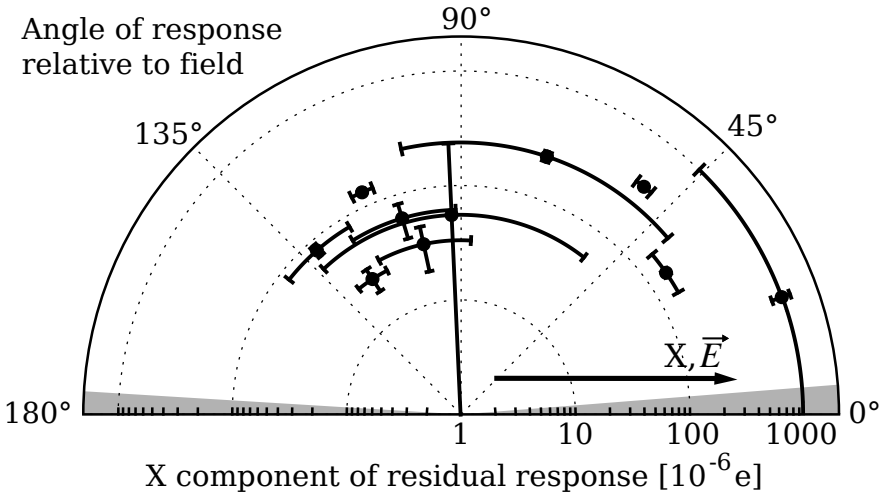

Figure 2.3: Measured residual response in the direction of the electric field for each microsphere at a net integral charge of 0 e. Both the X component of the overall residual response as well as the smallest angle in 3D between the direction of the microsphere motion and the X axis are shown. The gray band denotes the envelope of the measured response angles for all microspheres at net charges between ± 10 e. While the microspheres show a statistically significant residual response, the measured angle of this response with respect to the field is typically inconsistent with the expected response for a residual net millicharge.

We conservatively calculate limits on the abundance of millicharged particles by assuming that the component of the residual response in the direction of the electric

field could be due to a net fractional charge. The resulting limit on the abundance per nucleon, n_χ, of particles with charge $\pm\epsilon e$ is shown in Fig. 2.4, and compared to previous limits from oil drop [5, 70] and magnetic levitometer [6, 67, 69] experiments. The gray shaded region denotes the parameter space directly excluded by the present results assuming the residual on each microsphere could be due to a single millicharged particle.

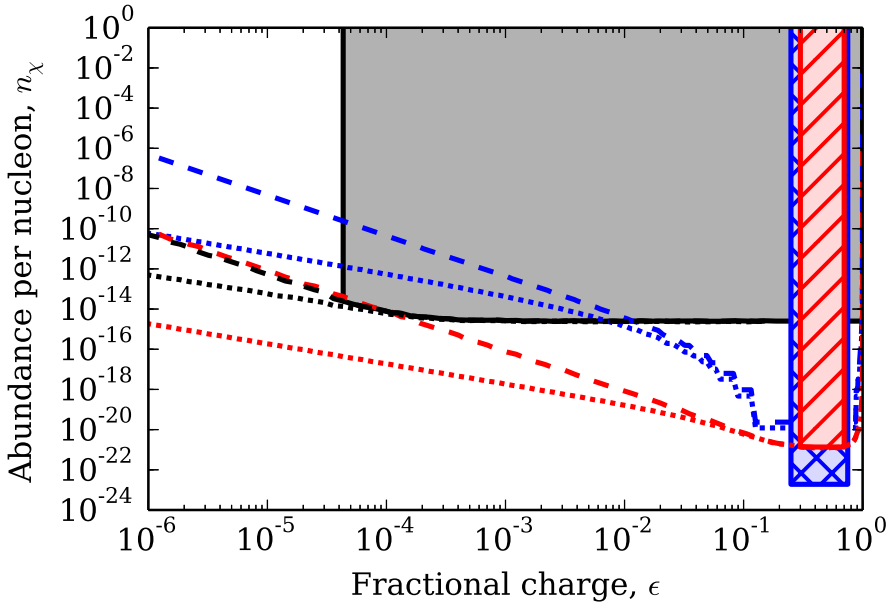

Figure 2.4: (Color online) Limits on the abundance of millicharged particles per nucleon, n_χ, versus the fractional charge, ϵ. The results from this work (black, solid fill) are compared to previous results from oil drop (blue, cross-hatched) [5] and magnetic levitometer (red, hatched) [6] experiments. The filled regions denote parameter space that is excluded at the 95% CL for which a single particle of fractional charge ϵ could be observed by each experiment, and correspond to the published limits from Refs. [5] and [6]. The lines extending from each region show our calculation of the upper limits below the single particle threshold assuming either equal average numbers of positive and negative particles (dashed), or a single sign of particles (dotted).

For the general case, where multiple millicharged particles could be bound to the microspheres, the distribution of the number of millicharged particles per microsphere is calculated for each value of n_χ. This distribution is calculated assuming Poisson statistics and either that the average number of positive and negative millicharged

particles is equal (dashed lines in Fig. 2.4), or that only particles of a single sign are trapped in bulk matter (dotted lines in Fig. 2.4). To be conservative, the likelihood of a non-zero net charge is taken to be unity below the mean residual measured for each microsphere, and to fall off with the measured Gaussian error above the mean residual. The likelihood marginalized over the distribution of the number of millicharged particles is then calculated, and a combined likelihood, L_{tot}, over all microspheres is formed. The 95% confidence level (CL) upper limit for n_χ is determined from L_{tot} following Wilks' theorem [81].

Although Refs. [5] and [6] published limits only above their single particle thresholds of $\epsilon \gtrsim 0.1$, we have calculated the analogous limits from these experiments below this threshold for comparison. For Ref. [6], we use the reported residual charge and errors for each levitated ball to calculate the limit following the same technique as for our data above. For Ref. [5], the total mass was divided into $\sim 4.3 \times 10^7$ individual droplets, and only the distribution of the measured residuals for these droplets was reported. Following the procedure in [5], we calculate the 95% CL limit on n_χ from this distribution given that no droplets were observed with $|q| > 0.25\ e$. As shown in Fig. 2.4, the limits below the single particle threshold fall off more quickly for Ref. [5] than for Ref. [6] or our results. This occurs because the total mass tested in [5] was divided into many small droplets, which reduces the probability that a single droplet will contain multiple millicharged particles.

As shown in Fig. 2.4, the present results provide the first direct search for millicharged particles in bulk matter with sensitivity to single particles with $5 \times 10^{-5} < \epsilon < 0.1$. Over this full range, the upper limit on the abundance per nucleon is at most $n_\chi < 2.5 \times 10^{-14}$ at the 95% CL for the material tested, while it improves to $n_\chi < 3.6 \times 10^{-15}$ for $\epsilon \gtrsim 10^{-3}$. For $\epsilon < 5 \times 10^{-5}$, constraints on the abundance per nucleon are less stringent since multiple millicharged particles per microsphere would be required to give an observable charge. Previous results from [6] can also constrain some or all of this region, depending on the assumed ratio of positive to negative particles. However, given the residual systematic effects seen in all such searches, the single particle sensitivity of this work is necessary to distinguish a signal from backgrounds since the expected discrete distribution of particles can be directly observed.

Future work to reduce the systematics described above may significantly improve the sensitivity of this technique.

2.5 Conclusion

In addition to providing the first direct search for single millicharged particles with $\epsilon < 0.1$ in bulk matter, this work also represents the first application of sub-aN force sensing using levitated microspheres in vacuum to search for new particles or interactions. The method demonstrated here for discharging microspheres with single-electron precision is applicable to future work using optically levitated microspheres since it provides an absolute calibration of the force sensitivity and a means of eliminating electrostatic backgrounds that depend on net charge. In particular, these techniques and further improvements may also allow significant increases in sensitivity to short range forces [32, 73], including searches for non-Newtonian gravitational forces at micron distances.

Chapter 3

Search for Screened Interactions

3.1 Statement of the Author's Contribution

The following chapter closely follows what was published in Ref. [47]. This work is important because it demonstrated the ability to measure a force between the microsphere and a nearby object. The author of this thesis contributed significantly to all aspects of this work but made particularly significant contributions to the design of the optomechanical system in the vacuum chamber, the design of the vacuum system, construction of the experiment, as well as data collection and analysis.

3.2 Introduction

Observations indicate that the universe is expanding at an accelerating rate [82–84]. This acceleration can be explained by the presence of 'dark energy' throughout the universe [33]. Although the nature of dark energy is unknown, one possibility is that it consists of a scalar field that couples to mass [85, 86]. Astrophysical measurements of the dark energy density imply an energy scale of $\Lambda = 2.4$ meV, corresponding to a length scale of $\hbar c/\Lambda \sim 80\,\mu$m.

It might be possible to detect the presence of a scalar field constituting dark energy by searching for new interactions between objects separated by distances below the dark energy length scale [12, 85–87]. In many cases, the resulting forces can

be substantially larger than Newtonian gravity at short distances [86, 88]. The most sensitive previous searches for violations of Newtonian gravity at or below the dark energy length scale employed macroscopic test masses or a conductive shield between the probe and test masses to minimize electromagnetic backgrounds [12, 38, 39, 89, 90]. Although these experiments place stringent constraints on deviations from Newtonian gravity, it is possible to construct theories of dark energy involving new forces that could have avoided detection due to the geometry and scale of previous experiments [14, 86, 88, 91]. For these screened interactions, recent searches using microscopic test masses such as atoms [7, 8] or neutrons [9–11] often provide the strongest constraints.

Several screening mechanisms have been proposed to evade existing experimental constraints on scalar interactions in the laboratory and solar system [86]. A specific example is the chameleon mechanism [92, 93], in which the effective mass of the chameleon particle (corresponding to the inverse length scale of the interaction) depends on the local matter density. At cosmological distances where the matter density is low, the chameleon field would mediate a long range interaction that explains the accelerating expansion of the universe [94]. However, most laboratory experiments are carried out in regions of high matter density, where the forces arising from the chameleon interaction are suppressed.

3.3 Experimental Techniques

This work presents a search for screened interactions below the dark energy length scale using optically levitated μm-size dielectric spheres as test masses. Levitated microspheres in high vacuum [4, 95–102] can be used to detect forces $\ll 10^{-18}$ N [53, 100, 103–105], and in many cases their small size avoids screening effects.

The test masses used in this work consist of amorphous silica microspheres with radius $r = 2.5$ μm and mass $m = 0.13$ ng [1] levitated in a single-beam, upward-propagating 1064 nm laser trap [53, 106]. The radiation pressure from the laser counters Earth's gravity and acts as an optical spring pulling the microsphere to the

[1] Bangs Laboratories, Inc., http://www.bangslabs.com

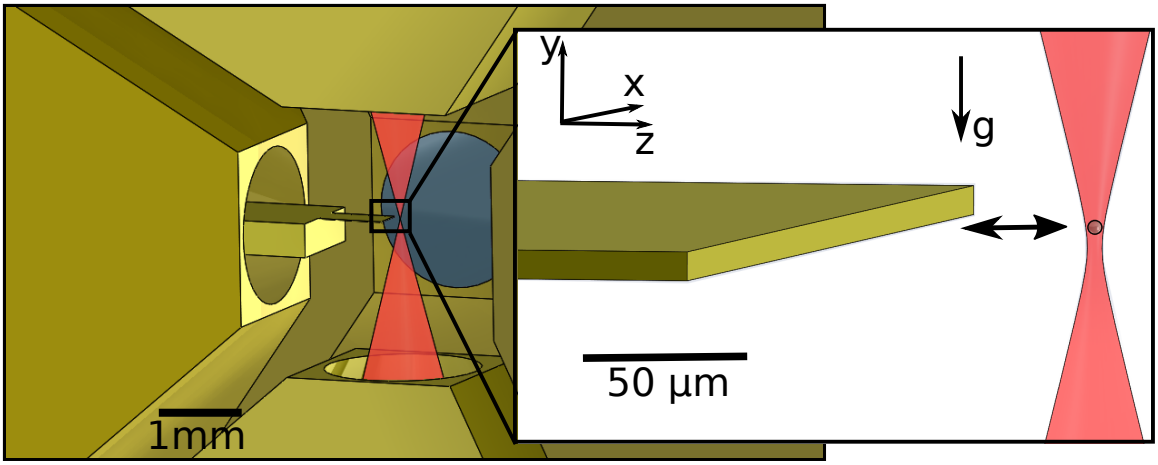

Figure 3.1: (left) Schematic of the optical trap and shielding electrodes. The electrode in the foreground is removed to show the inside of the trap. (right) Zoom in on the region near the trap. A 5 μm diameter microsphere is suspended at the focus of an upward propagating laser beam. The 10 μm thick Au-coated Si cantilever is positioned at ∼20–200 μm separations from the microsphere and oscillated in the z direction using a nanopositioning stage.

center of the Gaussian beam [107]. The resonant frequencies of the trap are $\sim$ 150 Hz for the 2 degrees-of-freedom orthogonal to the Earth's gravity and $\sim$ 100 Hz for the degree-of-freedom parallel to Earth's gravity. The position of the microsphere is measured by focusing secondary 650 nm Gaussian laser beams on the microsphere and imaging the pattern of scattered light onto a position-sensitive photodiode (PSPD). For small displacements from the center of the trap, the PSPD produces a differential current that is a linear function of the position of the microsphere.

When the microspheres are loaded into the optical trap, they typically have an electric charge of $\sim 100e$ [53]. The charge is measured by monitoring the response to an oscillating electric field. Microspheres are discharged with UV radiation from a Xenon flash-lamp. As shown in [53], clear charge quantization can be observed at the end of the discharging cycle, providing a force calibration for the system.

The microspheres are levitated inside of a vacuum chamber to reduce the force noise coming from collisions with residual gas. Due to reduced gas damping, the trap becomes unstable below 0.05 mbar. To stabilize the trap, active feedback is applied

by measuring the microsphere's position and modulating the position of the trap. Measurements are performed at pressures below 10^{-6} mbar where the noise for force measurement is limited to 2×10^{-17} N Hz$^{-1/2}$ by imaging noise. The optical setup and calibration methods are improved versions of those discussed in [53].

A schematic view of the apparatus is shown in Fig. 7.1 where a coordinate system is defined. The microsphere coupling is probed with a silicon cantilever with dimensions 500 μm $\times$ 2000 μm $\times$ 10 μm and a 500 μm thick handle, fabricated from a silicon on insulator (SOI) wafer using optical photolithography and plasma etching. The 10 μm dimension is oriented so that the cantilever clears the Gaussian beam waist of the laser and the 500 μm dimension is approximately centered on the trap in the x direction. A 200 nm gold shielding layer was evaporated onto the cantilever to minimize its electrostatic interactions with the microsphere. The cantilever is mounted on a 3-axis nanopositioning stage used to control its spacing from the microsphere with a precision of 3 nm and a travel of 80 μm [2]. The trap and cantilever are electrically shielded inside a cube consisting of six gold-plated electrodes separated by 4 mm, whose potentials are controlled by external digital-to-analog converters (DACs). The nanopositioning stage is mounted on a piezo motor driven stage with 12 mm travel in the z direction to provide coarse positioning.

3.4 Data and Results

To measure electrostatic interactions between the cantilever and the microsphere, each shielding electrode was set to a nominal potential of 0 V while the cantilever was biased to a non-zero potential. The z position of the nanopositioning stage was driven with an 18.3 Hz sine wave over its full 80 μm travel. The microspheres were aligned with the center of the cantilever in the y direction by determining the position at which the maximum electrostatic response was seen as the cantilever was swept in the z direction at fixed bias. The microsphere and stage positions were recorded in 50 s long integrations. Data were acquired for coarse stage positions with closest approach of 20, 60, 100, and 150 μm. This procedure was repeated for each of three

[2]Newport, product number: NPXYZ100SGV6, http://www.newport.com

Table 3.1: Dipole moments and polarizabilities measured for each microsphere.

Microsphere	p_{0z} [$e\,\mu$m]	α/α_0
#1	151 ± 6	0.21 ± 0.13
#2	89 ± 10	0.00 ± 0.33
#3	192 ± 30	0.25 ± 0.14

microspheres considered in this work.

To eliminate low frequency drifts, the microsphere positions were first mean subtracted. The data were then averaged in 10 μm cantilever position bins and calibrated to force units using the single-charge-step calibration discussed previously. Data at neighboring coarse-stage positions were matched in the 30–40 μm overlap region. The measured electrostatic force versus spacing between the cantilever and the microsphere is shown in Fig. 3.2.

Although electrically neutral microspheres are used, they still contain $\sim 10^{14}$ charges and interact primarily as electric dipoles. The force on a microsphere with dipole moment $\mathbf{p}$ is given by $\mathbf{F} = (\mathbf{p}\cdot\nabla)\mathbf{E}$ [43], where $\mathbf{p} = \mathbf{p}_0 + \alpha\mathbf{E}$ consists of a permanent dipole, $\mathbf{p}_0$, and an induced dipole, $\alpha\mathbf{E}$, for polarizability α. The latter term incorporates any dipole induced by an electric field, including the linear dielectric response as well as any non-zero surface charge mobility. Figure 3.2 shows a fit to the model $\mathbf{F}\cdot\hat{z} \equiv F_b(z) = (p_x\partial_x + p_y\partial_y + p_z\partial_z)E_z \approx p_{0z}\partial_z E_z + \alpha E_z\partial_z E_z$.

A finite-element method (FEM) was used to solve for $\mathbf{E}$ within the geometry of the trapping region. Dipole moments and polarizabilities were extracted by fitting the microsphere responses at non-zero cantilever bias to $F_b(z)$. The results of this fit for each microsphere are shown in Table 3.1. The dipole moments are measured in units of $e\,\mu$m and the polarizabilities are reported relative to $\alpha_0 = 3\epsilon_0\left(\frac{\epsilon_r-1}{\epsilon_r+2}\right)(\frac{4}{3}\pi r^3)$ assuming $\epsilon_r \sim 3$ and $r = 2.5$ μm. The reported values of polarizability, which are smaller than α_0, could arise from systematics in the determination of a small induced dipole on top of a much larger permanent dipole, an unexpectedly low value of ϵ_r, or a smaller than expected volume.

Following the measurement of the electrostatic interaction at a given coarse stage

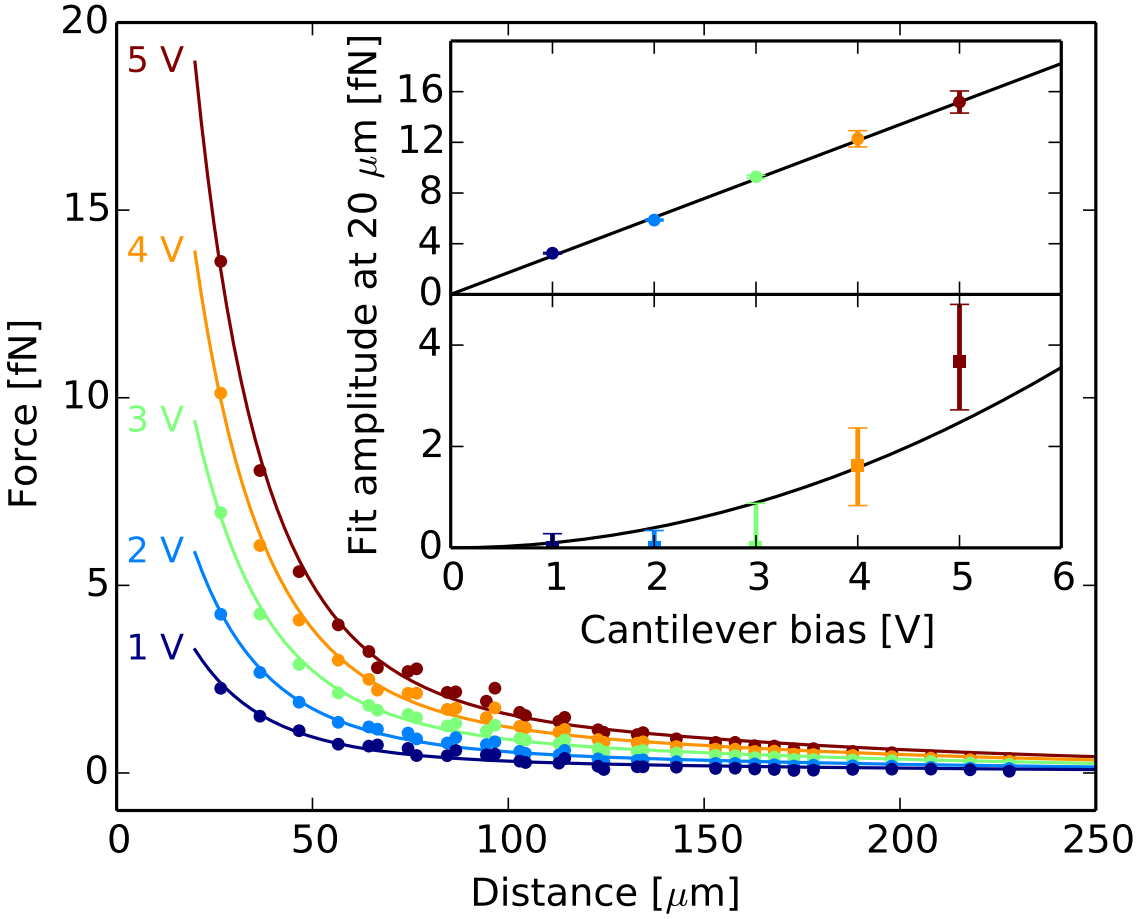

Figure 3.2: Measured response of microsphere #1 versus distance from the cantilever face as the cantilever is swept in z with a constant bias of 1,2,3,4, and 5 V. The data points are shown as dots and the best fit model as solid lines. (inset) Amplitude of the fit component $\propto \partial_z E_z$ (top) and the fit component $\propto E_z \partial_z E_z$ (bottom). Fits to the expected linear and quadratic dependence on the voltage are also shown (solid lines).

position, the cantilever was set to a nominal potential of 0 V, and twenty additional 50 s long integrations were acquired to search for new screened interactions. This procedure was then repeated to obtain three 1000 s measurements at each coarse stage position in order to quantify time dependent variation in the measured response over a period of several hours. The standard deviation of the repeated measurements

at each position bin was included as an additional systematic error.

The measured force versus position for each of the three microspheres is shown in Fig. 3.3. A small residual force $\lesssim 10^{-16}$ N can be seen for each microsphere. This response is consistent with electrostatic forces resulting from the permanent electric dipole moment of the microspheres coupling to the electric field produced by potential differences between the cantilever and shielding electrodes of $\lesssim 30$ mV. Contact potentials of this scale are expected to arise between connections to the electrodes in the vacuum chamber and external electronics.

The data shown in Fig. 3.3 can be used to set constraints on new screened interactions at distances of the order of the dark energy length scale, with a sensitivity that is limited by the presence of the residual electrostatic backgrounds. As a concrete example, we consider the presence of a non-relativistic, steady-state chameleon field, ϕ, that mediates a force between the microsphere and cantilever. Following [8, 88, 91], we assume an inverse power law form of the effective potential $V_{\rm eff}(\phi) = \Lambda^4[1 + (\Lambda/\phi)^n] + (\beta\rho/M_{Pl})\phi$. Here, Λ is the scale of the chameleon self interaction, often chosen at the dark energy scale $\Lambda \sim 2.4$ meV. The coupling to matter of density ρ is determined by the scale $M = M_{Pl}/\beta$ where M_{Pl} is the reduced Planck mass and β is unitless. Although other power laws are possible, $n = 1$ was chosen as a characteristic example for this search.

Similar to the electric field calculation described above, an FEM was employed to solve the non-linear equation of motion $\nabla^2\phi = \partial_\phi V_{\rm eff}$ in the geometry described previously. The residual gas pressure of $\sim 10^{-6}$ mbar was included, but has negligible effect on ϕ for values of the matter coupling considered in this work. Boundary conditions were set to the equilibrium value of the field within the cantilever and electrodes, following the detailed treatment of matter-vacuum interfaces in [8].

The resulting chameleon force on a microsphere in the z direction was calculated as $F_c(z, \beta, \lambda) = \lambda(\beta\rho/M_{Pl}) \int_V (\partial_z\phi)\, dV$ where ρ and V are the density and volume of the microsphere and λ is a screening factor [8, 91]. In the region of parameter space where $\rho r^2 < 3M_{Pl}\phi/\beta$, the microsphere is unscreened and $\lambda = 1$. However, when β becomes sufficiently large, the force on the microsphere is suppressed by $\lambda < 1$ [8, 91].

The data for each microsphere were fit to a model $F(z) = A_c F_c(z, \beta, \Lambda) + A_b F_b(z) +$

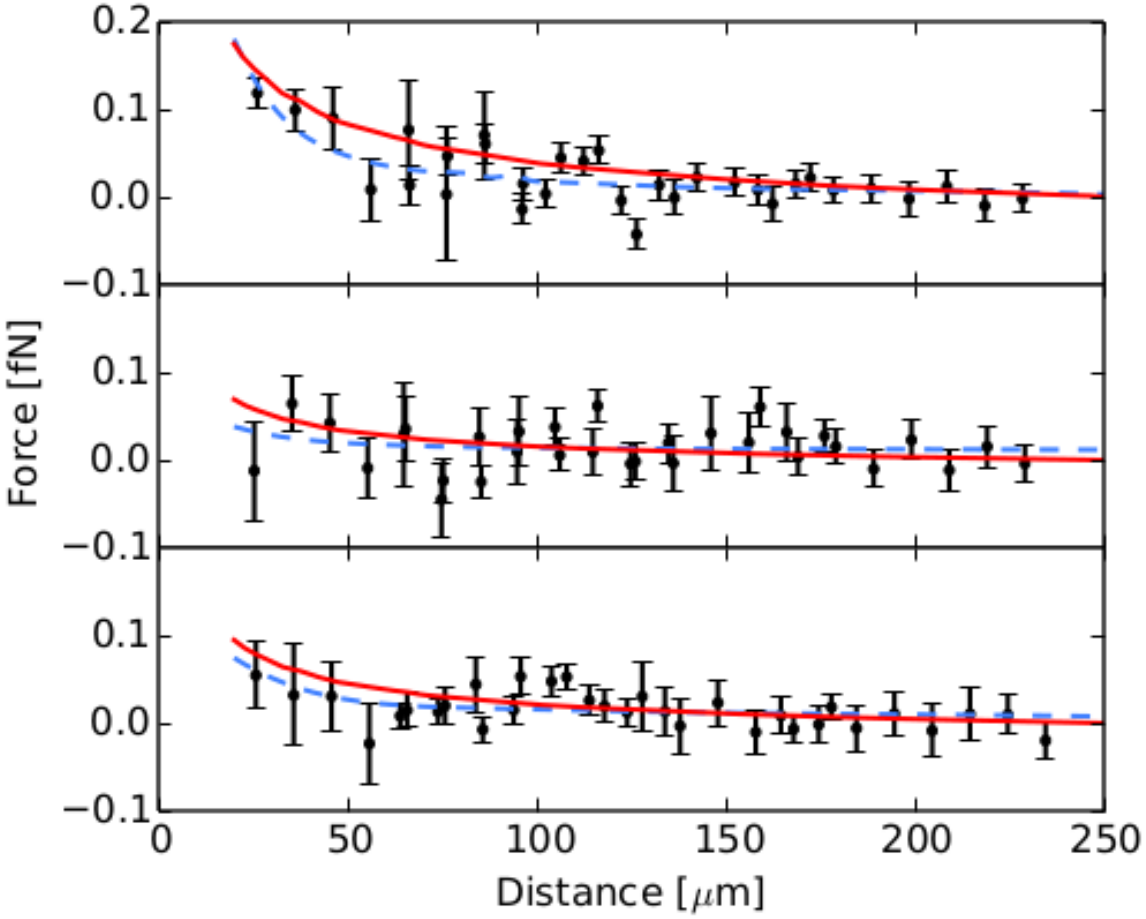

Figure 3.3: Measured response for microspheres #1 (top), #2 (middle), and #3 (bottom) versus distance from the cantilever face as the cantilever is swept in z with a nominal bias of 0 V. The best fit electrostatic background-only model (dashed) and the amplitude of a chameleon force at the 95% CL upper limit for $\Lambda = 10$ meV (solid) are also shown.

A_0, where $F_b(z)$ is the shape of the empirical background measured for each microsphere when the cantilever was biased to 5 V, A_b is the unknown electrostatic background amplitude due to residual contact potentials on the electrodes, and A_0 accounts for the arbitrary offset subtracted from the data at each coarse stage position.

A_c, the normalization of the chameleon force, was constrained in the fit by the

following systematics. The microsphere mass was not directly measured, but the radius of the spheres was determined by the manufacturer to be 2.5 ± 0.24 μm, leading to a 35% uncertainty on the chameleon force. Fits of the calibration data to the electric field simulations indicate that the microsphere was centered in y relative to the cantilever within 4 μm, leading to an uncertainty on the amplitude of the chameleon force of 1.8%. The z position of the coarse stage was determined from microscope images of the cantilever to $\lesssim 10$ μm, at each coarse stage setting. Using the positions and uncertainties determined from the calibration images, the coarse stage positions were further refined by allowing z-position offsets to float at each coarse stage position in the electrostatic fit. The best fit positions were used in the final chameleon fit, and their uncertainties contribute an additional systematic error of 6%. All errors were added in quadrature for a total systematic error of 36% on A_c, dominated by the uncertainty in the microsphere masses.

At each value of Λ, the profile of the negative log likelihood (NLL) was calculated by minimizing the NLL for the fit at each value of β over the nuisance parameters A_c (including its Gaussian constraint), A_b and A_0. The 95% confidence interval for β was determined from the combined profile from all three microspheres following Wilks' theorem [108, 109]. This was done assuming that 2NLL follows a χ^2 distribution with one degree-of-freedom (DOF). The χ^2 statistic at the best fit point and for the background only model indicates that both provide a good fit to the data. At the best fit point, $\chi^2 = 97.8$ for 87 DOF, while for the background only model $\chi^2 = 98.9$ for 88 DOF. For all Λ, the data are consistent with the background-only model at the 95% confidence level (CL). The background-only fits are shown in Fig. 3.3, together with the amplitude of a chameleon force at the 95% CL upper limit.

The resulting limits on $1/\beta = M/M_{Pl}$ are shown in Fig. 3.4 and compared to existing limits on chameleon interactions. Due to the self-screening of the microsphere at large values of β, these results are not able to constrain forces arising from chameleons for $\Lambda = 2.4$ meV given current backgrounds. However, at values of $\Lambda > 4.9$ meV, the self-screening is reduced, and these data are able to constrain chameleon interactions. These bounds are within a factor of 3 of the best existing constraints from atom interferometry using an entirely independent technique.

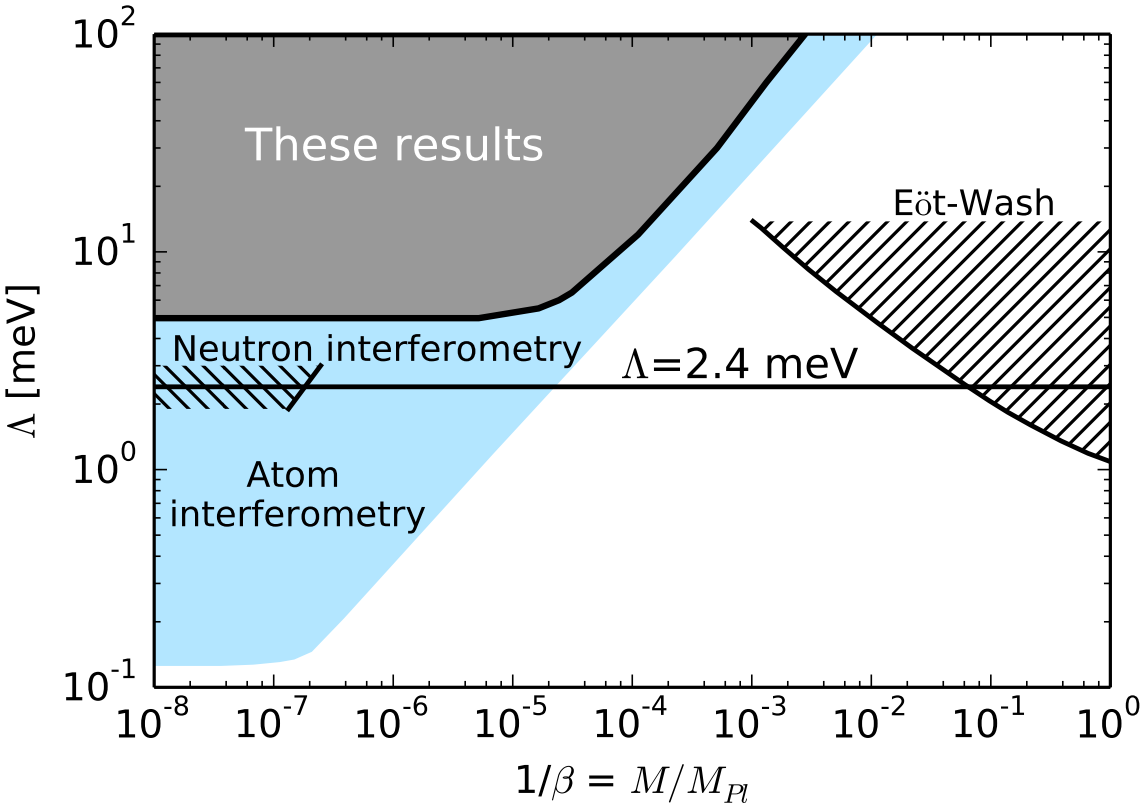

Figure 3.4: (color online) Limits on Λ versus $1/\beta = M/M_{Pl}$ for the chameleon model discussed in the text. The 95% CL exclusion limits from this search are denoted by the dark (gray) region. Recent constraints from atom interferometry are shown by the light (blue) region [7, 8]. The horizontal line indicates $\Lambda = 2.4$ meV. Limits from neutron interferometry [9–11] and from the Eöt-Wash torsion balance experiment [12–14] are denoted by the hatched regions. These limits are shown only in the restricted regions of parameter space considered in Refs [9] and [14].

3.5 Conclusion

The analysis presented here constrains screened interactions that would produce a force between the cantilever and the microsphere greater than 0.1 fN at separations greater than 20 μm. This search is limited by backgrounds from fixed dipole moments in the microspheres coupling to electric fields caused by contact potentials.

One method for reducing such backgrounds is to spin the microspheres by applying an optical [110] or electrostatic torque [111]. It might be possible to anneal the microspheres in situ [112] to increase the rate at which separated charges within the microspheres recombine. Finally, commercially available microspheres made from different materials might have smaller permanent dipole moments. Some combination of these techniques may be used in the future to enhance the sensitivity reached here.

These results provide the first search for interactions below the dark energy length scale using isolated mesoscopic objects separated by mesoscopic distances without an intervening electrostatic shield. This experimental technique is complementary to previous searches and could be sensitive to interactions that have evaded detection to date. The determination of the electric field near the cantilever and measurement of the interaction of electrically neutral silica microspheres with these fields provides important constraints on the expected backgrounds for future searches using similar methods. Future work will feature a search optimized for unscreened Yukawa interactions.

Chapter 4

Single-beam trapping

4.1 Statement of the Author's Contribution

The following chapter closely follows what was published in Ref. [17]. This work is important because it developed trapping with a single laser beam with enhanced sensitivity to scattered light, which enabled or simplified the following measurements. The author of this thesis played an important role in developing the idea of using interferometric imaging, as well as designing and constructing an implementation of heterodyne imaging for levitated microspheres.

4.2 Introduction

Optical traps for small dielectric particles have been used since the pioneering work of Ashkin and Dziedzic [24]. Although many of the initial applications of these traps were in biology and polymer science, where the particles are suspended in a liquid [26, 77, 113, 114], trapping and cooling of microspheres (MSs) in a vacuum environment has become a common tool in the fields of optomechanics [1, 51, 73, 115–119], quantum control [120, 121] and fundamental particles and interactions [32, 46, 47, 114, 122]. While several techniques for trapping MSs in vacuum have been proposed and implemented [1, 52, 74, 122–127], single-beam traps with an upward propagating, focused laser beam and active feedback have the advantages of simplicity and access to the trapping region to probe the MS.

In the single-beam trap described here, radiation pressure from the beam supports

the weight of the MS while recoil against light deflected by the MS provides a restoring force, confining the MS toward the axis of the beam [24, 26, 49] where the MS undergoes harmonic motion in three dimensions. Radial (horizontal) feedback forces are applied to the MS by modulating the position of the trap while axial (vertical) feedback forces are applied by modulating the trap beam power. Vacuum operation is required to minimize noise due to collisions between residual gas and the MS. Under vacuum, active feedback is used to stabilize the trap by replacing the damping from residual gas. In this way, the center-of-mass motion of the particle can be damped to obtain mK effective temperatures [1, 52, 74, 126] with the rest of the system at room temperature.

The system described here uses heterodyne detection to measure the position of the MS and provide feedback by interfering the light transmitted through, and reflected by, the MS with frequency-shifted phase reference beams. In addition to the simplicity of the single-beam trap, the heterodyne detection technique results in improved immunity to stray sources of light not associated with the MS because only light spatially and temporally coherent with the phase reference beam produces an interference signal at the detector. The ability to reject scattered light is particularly important for short-distance force sensing applications [32, 47], where objects used to probe the MS may scatter light from the trapping beam, producing background signals.

4.3 Experimental Setup

The apparatus presented here makes use of 4.8 μm diameter silica MS [128] trapped in vacuum by a single-beam optical trap. The trapping and phase reference beams are produced by seeding a single frequency, polarization maintaining (PM), Yb-doped fiber amplifier [129] with light from a $\lambda = 1064\,\text{nm}$, single frequency, distributed feedback, Yb-doped fiber laser [130]. The spatial coherence length of this system, $\gg 10^3\,\text{m}$, is greater than any differences in optical path length. The output of the amplifier is passed through a PM fiber splitter to obtain trapping and phase reference beams. The two branches are sent into fiber-coupled acousto-optic modulators (AOMs) driven at 149.5 MHz and 150.0 MHz that frequency shift the source light and allow for intensity modulation. Frequency shifting both the trapping light and the phase reference light

avoids the amplification of rf signals at the interference frequency which could lead to electronic backgrounds. The reference branch is further split into two branches for use in the axial and radial heterodyne measurements.

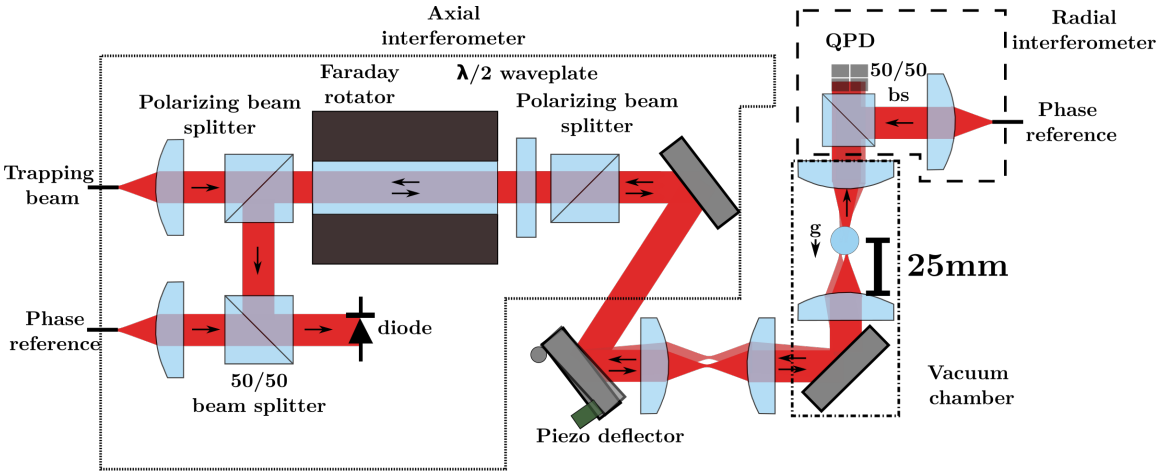

Figure 4.1: Schematic view of the free-space optical system. The output of the fiber carrying the trapping beam is first collimated, then deflected by a high-bandwidth piezo-mounted mirror in the conjugate focal plane of the trap. This produces translations in the plane of the trap, as indicated by the two closely spaced beams. A telescope is used to adjust the gain of the deflection system. Two identical aspheric lenses inside the vacuum chamber focus the trapping beam and recollimate it. The collimated beam is then recombined with a reference beam on a quadrant photodiode (QPD). Light that is backscattered by the MS is extracted, recombined with another reference beam and used to interferometrically measure the axial position of the MS.

A simplified schematic of the free space optics forming the trap and providing the position readout for the MS is shown in Fig. 5.1. The trapping and reference beams are projected into free space with the fibers providing mode cleaning and flexibility of installation. All optical fiber components are fusion spliced together for reliability. Following the fiber launch, the trapping beam passes through a Faraday isolator which is used to extract the back-propagating light reflected by the MS. The beam is then reflected off a high-bandwidth (3 dB point at 2.5 kHz) piezo-actuated deflection mirror imaged into the the Fourier plane of the trap by a telescope. Angling the mirror produces displacements of the trap that are used to apply radial feedback forces to the MS.

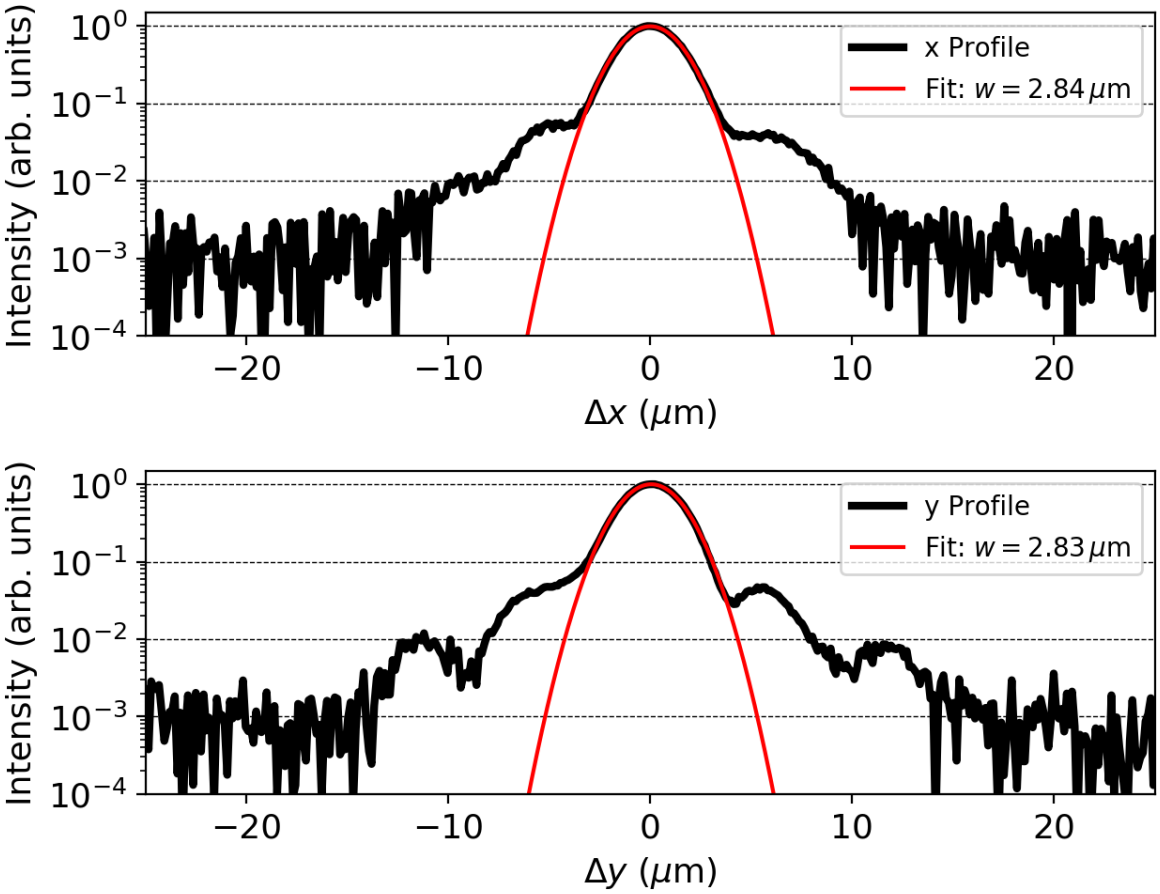

Figure 4.2: Trapping beam profile in the x and y axes at the stable point of the trap. Fits to a Gaussian profile give $w_{o,x} = 2.84\,\mu$m and $w_{o,y} = 2.83\,\mu$m (with w_o being the usual Gaussian waist) at the stable point of the trap, which is a small fraction of a Rayleigh range above the focus. Non-Gaussian tails could result from cladding modes within the fiber or imperfections in optical surfaces, as well as small misalignments.

The beam is then injected into the vacuum chamber, where it is focused by a 25 mm focal length aspheric lens to form the trap. This long free working distance is ideal for many applications requiring access to the trapping region. The beam transmitted through the microsphere is recollimated by an identical aspheric lens, sent out of the vacuum chamber and superposed with a reference beam. This superposition is projected onto a quadrant photodiode (QPD) from which the radial motion along two axes, x and y, is extracted from the interference photocurrents at the difference in modulation

frequencies.

To measure the axial position of the MS, the back-propagating light extracted by the Faraday isolator is interfered with the second phase reference beam. The interference generates an rf photocurrent whose phase encodes the z-position, as the path length of the back-propagating light depends on the MS position. This eliminates the need for an auxiliary imaging beam perpendicular to the trapping beam and provides the MS position in absolute units related to the wavelength of the trapping light.

All relevant optics have been optimized to image the fiber mode into the focal plane of the trap with minimal distortion. A relatively pure fundamental Gaussian spatial mode is important for short-distance force sensing, where devices are brought into close proximity with the MS [47]. The profile of the spatial mode at the stable position in the trap is shown in Fig. 4.2.

The axial and the radial signals are first digitized, and then analyzed by a field programmable gate array (FPGA) running the algorithms that generate real-time feedback signals. In the radial direction, only active damping is applied, so as not to disturb force measurements at frequencies below the trap resonance.

4.4 Radial Displacement Calibration

While axial displacements are intrinsically calibrated into physical units by the wavelength of the laser, displacements of the radial degree of freedom have to be calibrated empirically. A calibration of the radial position measurement is obtained by measuring the response of the system to known forces at frequencies far below resonance, and then dividing this response by the spring constant of the trap. The response to forces is determined, with active feedback on, by applying an alternating electric field to a MS with a few quanta of charge, as demonstrated in Ref. [46]. The result of this procedure is $(\Delta V/F)_{\mathrm{meas}} = (7.5 \pm 0.3) \times 10^{13}\,\mathrm{V/N}$ for either radial degree of freedom (DOF), within uncertainties, where ΔV is the voltage generated in photodetection due to a difference in photocurrent between sides of the QPD and F is the known force applied to the MS. This quantity can then be converted into a calibration constant for position by using $F_{\mathrm{app}} = kx_{\mathrm{MS}}$ where x_{MS} is the displacement in one of the radial DOFs and the spring

constant k is measured by observing the response of the MS to an oscillating electric field of variable frequency.

It is instructive to compare this empirical calibration constant to the ideal one, calculated from the properties of the system. In principle, this could be derived by solving Mie scattering theory, whereby MS displacements deflect some of the trapping light, and applying simple ray optics. However, the relationship between the MS displacement, x_{MS}, and the angle by which the light is deflected, θ, can be extracted directly by considering the optical restoring force F_{opt} for a certain θ. This force is related to displacements of the MS by the spring constant of the trap $k = m_{\mathrm{MS}}\Omega^2$ where m_{MS} is the mass of the MS and Ω is the resonant frequency of the trap. For small displacements causing small θ, $F_{\mathrm{opt}} = (\mathcal{P}/c)\,\theta$, where $\mathcal{P}$ is the power of the beam transmitted through the MS and c is the speed of light. After re-collimation by a lens of focal length d, the relationship between the force and the translation of the outgoing beam, x_B, is

$$\frac{F_{\mathrm{opt}}}{x_B} = \frac{\mathcal{P}}{d\,c}. \tag{4.1}$$

The quantity x_B is determined by interfering the beam with a phase reference beam shifted in frequency by an amount $\Delta\omega$, and projecting their superposition onto a segmented photodetector.

If the transmitted and reference beams are Gaussian with their foci in the detector plane, then $\mathbf{E}_i(\mathbf{x}) = \hat{p}_i E_i e^{-\mathbf{x}^2/w_i^2}$ with $\hat{p}_i$ being the polarization vectors and w_i being the usual Gaussian waists ($w = 2\sigma_{\mathcal{P}}$, where $\sigma_{\mathcal{P}}$ the standard deviation of the intensity). Displacing beam "2" by x_B, and making use of Eq. (4.1) and $F = kx_{\mathrm{MS}}$, the difference in photocurrent between adjacent segments per MS displacement is given by

$$\frac{\Delta I}{x_{\mathrm{MS}}} = 4\xi\sqrt{\frac{\mathcal{P}_1\mathcal{P}_2}{4\pi}}\frac{w_1^2}{(w_1^2+w_2^2)^{3/2}}\frac{k\,d\,c}{\mathcal{P}_2}\cos[\Delta\omega t + \Delta\phi], \tag{4.2}$$

where ξ is the responsivity of the photodetector in A/W, $\mathcal{P}_1$ ($\mathcal{P}_2$) and w_1 (w_2) are the power and waist of the phase reference (transmitted) beam, respectively, and beam 2 is displaced. In practice, $\mathcal{P}_1$ can be increased to optimize sensitivity, but $\mathcal{P}_2$ is fixed by the power required to levitate a particular mass of MS. For the parameters of the system described here, $\mathcal{P}_1 = 25\,\mathrm{mW}$, $\mathcal{P}_2 = 1.1\,\mathrm{mW}$, $w_1 = 3.7\,\mathrm{mm}$, $w_2 = 3.0\,\mathrm{mm}$, $k = 2.0\times10^{-7}\,\mathrm{N/m}$, $\xi = 0.34\,\mathrm{A/W}$, and $d = 25\,\mathrm{mm}$, this corresponds to an ideal

difference in photocurrent per MS displacement of 350 A/m. A detailed derivation of Eq (4.2) is included in the appendix.

This value can be compared with the empirically obtained calibration as $\Delta V/F = (\Delta I/x_{\mathrm{MS}}) \cdot (GR_t/k)$, where G is the gain of the readout electronics and R_t is the transimpedance. With $G = 259 \pm 3$ set by digital potentiometers, and $R_t = 1\,\mathrm{k}\Omega$, we find that $(\Delta V/F)_{\mathrm{calc}} = 4.5 \times 10^{14}\,\mathrm{V/N}$ compared with $(\Delta V/F)_{\mathrm{meas}} = (7.5 \pm 0.3) \times 10^{13}\,\mathrm{V/N}$. We attribute the discrepancy to imperfect mode-matching between the transmitted and the reference beams as well as slight non-Gaussianity of the modes of the two beams, as can be seen in Fig. 4.2.

4.5 Displacement Noise

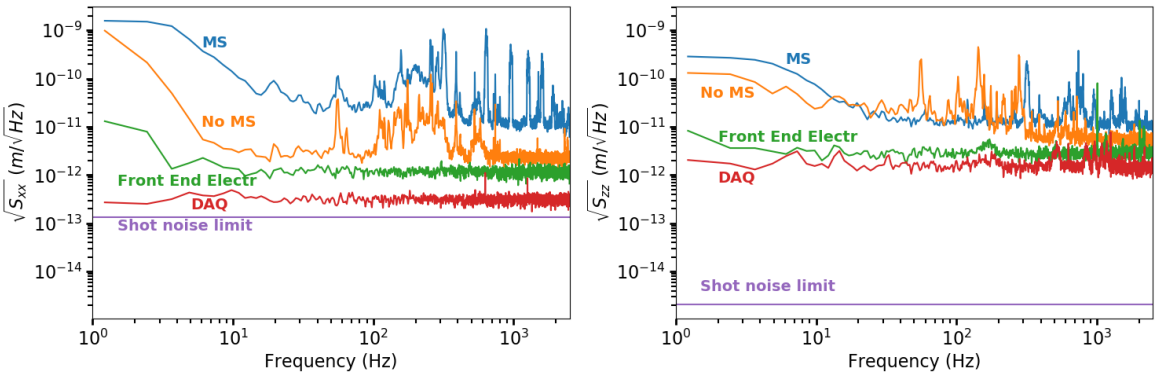

Figure 4.3: (left) Comparison between MS displacement noise in the radial DOF and the shot noise limit. Also shown is the digitizer noise, with the data-acquisition (DAQ) input terminated, the noise of the photodetector and front-end electronics without incident light, and the noise measured by the full heterodyne readout, but without a MS in the trap. (right) MS displacement noise in the axial DOF. In this case, the data collected without the MS is obtained by reflecting the light off of a gold-plated cantilever at the trap position. The intensity of the trapping beam was tuned such that the cantilever reflected the same power as a MS. The remaining curves are obtained in a manner similar to those in the left panel. Data are calibrated empirically with the spring constant measurement discussed in Sec. III, whereas the radial shot noise calculation makes use of Eq. (4.2) and the axial shot noise makes use of the interferometric relation, both assuming perfect modes and mode matching.

Shot noise places a fundamental limit on the performance of the system, which is

computed following Ref. [131]. The shot-noise-limited displacement spectral density can be determined from the usual relation between shot noise and mean photocurrent, $S_{\text{shot}} = 2eI$ [132], together with Eq. (4.2). We find

$$S_{xx} = \frac{\pi e \mathcal{P}_2}{2\xi \mathcal{P}_1} \frac{(w_1^2 + w_2^2)^3}{w_1^4 k^2 d^2 c^2} (\mathcal{P}_1 + \mathcal{P}_2), \tag{4.3}$$

where S_{xx} refers to displacements along a radial DOF. Analysis of the axial DOF is more straightforward. The axial position of the MS is determined by using heterodyne detection to measure the phase of light reflected by the MS. A change in the phase of the reflected light, $\Delta\phi_z$, is related to axial displacements of the MS, z_{MS}, by $(\Delta\phi_z / z_{\text{MS}}) = 2\pi/(\lambda/2)$. Assuming perfect mode matching, the shot noise limit for the axial position measurement is

$$S_{zz} = \left(\frac{\lambda}{4\pi}\right)^2 \frac{e(\mathcal{P}_A + \mathcal{P}_B)}{8\xi \mathcal{P}_A \mathcal{P}_B}, \tag{4.4}$$

where S_{zz} refers to displacements along the axial DOF, $\mathcal{P}_A$ is the power of the axial reference beam and $\mathcal{P}_B$ is the power reflected from the MS. A detailed derivation of Eqs. (4.3) and (4.4) is included in the appendix. Throughout, we assume perfect mode matching, because this represents the fundamental limitation to which any practical implementation should be compared.

The values of $\sqrt{S_{xx}}$ (representative of both radial DOFs) and $\sqrt{S_{zz}}$ are shown in Fig. 4.3, together with position spectral densities measured under various conditions. The cases shown in the figure correspond to displacement spectra acquired with and without a MS in the trap, with the trapping beam off, and with the front-end electronics disconnected and data-acquisition electronics terminated. The latter two cases measure the photodetector and front-end electronics noise, as well as digitizer noise, respectively. Clearly, nonfundamental sources of displacement noise far exceed the shot noise limit and thus substantial performance improvements should follow successive refinements of the apparatus.

4.6 Stray Light Rejection with Heterodyne Measurements

Immunity to extraneous sources of light is critical for short-range force sensing where objects that scatter light are brought close to the MS. Heterodyne systems provide substantial rejection of light propagating along a path that is different from the desired one. For a detector positioned in the Fourier plane of the trap, angular rejection corresponds to displacement rejection in the focal plane of the trap.

The angular rejection of the heterodyne system described is estimated by considering the interference of two Gaussian beams at their focus separated by an angle α between their wavefronts. The profile of angular rejection $H(\alpha)$ can be computed from the normalized integral $\iint |\mathbf{E_1} + \mathbf{E_2}|^2 dA$ with $\mathbf{E_1}$ and $\mathbf{E_2}$ the electric fields associated with the appropriately tilted Gaussian beams. We find that the profile of scattered light rejection can be approximated by,

$$H(\Delta x) \simeq \exp\left[\frac{-(2\pi/\lambda)^2 w_1^2 w_s^2}{4(w_1^2 + w_s^2)} \left(\frac{\Delta x}{d}\right)^2\right], \tag{4.5}$$

where w_s is the waist associated with the source of scattered light imaged onto the detector, and $\Delta x = d\,\alpha$. This result can be compared with data collected by using the trapping beam as a test source of light and angling the reference beam, with a single-channel photodiode placed in the detector focal plane, in the place of the QPD. The response, calibrated in terms of position at radial distances Δx from the center of the trap, is shown in Fig. 4.4, along with the prediction of Eq. (4.5). The tails of the distribution present in the data, but not the calculation, are likely due to interference of the reference beam with the halo of the trapping beam, shown in Fig. 4.2.

4.7 Acceleration Noise Performance

Acceleration noise, defined as force noise per unit MS mass, is an important figure of merit for force-sensing applications. While the primary goal of the technique described here is to provide a displacement measurement insensitive to stray sources of light, with comfortable access to the trapping region, the acceleration noise achieved is comparable

to the state of the art for levitated MSs. Figure 4.5 shows the acceleration amplitude spectral densities of the MS motion in each degree of freedom under vacuum conditions (10^{-6} mbar) and, for comparison, at a pressure of 1.5 mbar where the MS is driven by collisions with residual gas. The 10 to 100 Hz band where the noise has a broad minimum is used for the force-sensing application of interest to this program. In this band we measure an acceleration noise of $7.5 \times 10^{-5}\,(\mathrm{m/s^2})/\sqrt{\mathrm{Hz}}$ for the radial DOFs and $1.5 \times 10^{-5}\,(\mathrm{m/s^2})/\sqrt{\mathrm{Hz}}$ for the axial DOF.

A comparison of the acceleration noise achieved here with those obtained with other techniques is shown in Table 4.1. The noise reported in the table corresponds to the optimal conditions reported by the authors, in analogy with the data presented here. Systems optimized for smaller MS are in some cases sensitive to smaller forces, but have poorer acceleration sensitivities [$\gtrsim 0.1\ (\mathrm{m/s^2})/\sqrt{\mathrm{Hz}}$] [118, 119, 126, 127], and are not included in the table. All apparatuses capable of trapping MS larger than 0.1 μm, other than the one described here, make use of non-interferometric optical measurements and require auxiliary imaging beams. The acceleration noise observed here is the lowest reported for optically levitated MS.

4.8 Conclusions

We have described a technique applying heterodyne detection to measure the three-dimensional position of a microsphere in an optical trap. This technique allows all functions (trapping, feedback, and position measurement) to be performed with a single laser, while providing a substantial rejection of signals arising from scattered light. This provides unmatched access to the trapped microsphere and, because of the insensitivity to scattered light, is particularly powerful in applications where the microsphere is used as a force sensor in close proximity to other objects.

We have presented the current performance of the system in terms of scattered light rejection and noise, which are at the state-of-the-art level. The noise performance of the system is far from the fundamental limit imposed by shot noise, leaving significant room for improvement.

Our group is planning to apply this technique to the measurement of interactions at

sub-100 μm distance that may arise from non-Newtonian gravity.

Calculations

1. Radial-displacement calibration

Here we provide a detailed derivation of Eq. (4.2), which is the difference in photocurrent at the heterodyne frequency between adjacent sides of a segmented detector per radial displacement of the MS. To begin, following Sec. III, if a MS deflects a trapping beam of power $\mathcal{P}$ by an angle θ, the restoring force from the change in optical momentum flux is given by,

$$F_{\text{opt}} = \frac{\mathcal{P}}{c}\sin[\theta] \approx \frac{\mathcal{P}}{c}\theta \approx \frac{\mathcal{P}}{c}\frac{x_B}{d}, \tag{A1}$$

where c is the speed of light and the approximation assumes small deflections. We have related optical force to displacements of the transmitted beam, x_B, since $x_B \approx d\theta$ for small θ, where d is the focal length of the recollimation lens.

Consider the interference of two Gaussian beams on a segmented detector, where both beams have foci in the detector plane, and one beam is displaced by a radial distance x_B. Let the segments be half-infinite planes with their border parallel to the y axis of our detector at $x = 0$. Let the center of our reference beam be at the origin and the trapping beam displaced by $\mathbf{\Delta x} = x_B\hat{x}$.

The electric field of a Guassian beam at its focus is,

$$\begin{aligned}\widetilde{\mathbf{E}}(\mathbf{x}, t) &= \mathbf{E}(\mathbf{x})e^{i\phi}\exp\left[i\omega t\right] \\ &= E_o\hat{p}\exp\left[\frac{-|\mathbf{x}|^2}{w_0^2}\right]e^{i\phi}\exp\left[i\omega t\right],\end{aligned} \tag{A2}$$

where E_o is the peak electric field, ϕ is a phase, $\hat{p}$ is the polarization, w_o is the waist, and ω is the optical angular frequency. If we interfere two such beams that differ in frequency by an amount $\Delta\omega$, the resulting irradiance on a photodetector can be computed as the square of the sum of the electric fields. Dropping the constant terms and considering

the term oscillating at $\Delta\omega$, we found,

$$I_{IF} = \frac{2\xi}{\eta} \iint \mathbf{E_1}(\mathbf{x}_1) \cdot \mathbf{E_2}(\mathbf{x}_2) \cos[\Delta\omega\, t + \Delta\phi]\, dA_1, \tag{A3}$$

where ξ is the responsivity of the photodetector in [A/W], $\eta = 1/c\,\epsilon$ is the wave impedance, ϵ is the dielectric constant, and the integral is computed over some bounded segment. $\mathbf{E}_i$ are the electric fields in the detector plane, with $i = 1$ the reference beam and $i = 2$ the trapping beam, and $\Delta\phi$ is a common-mode phase across all quadrants due to path length fluctuations. The expression is defined in terms of and integrated over $\mathbf{x}_1$ with $\mathbf{x}_2 = \mathbf{x}_1 + \mathbf{\Delta x}$.

We perform this integral over two regions: (1) $\mathbf{x}_1 \cdot \hat{x} \in (-\infty, 0]$, $\mathbf{x}_1 \cdot \hat{y} \in (-\infty, \infty)$ and (2) $\mathbf{x}_1 \cdot \hat{x} \in [0, \infty)$, $\mathbf{x}_1 \cdot \hat{y} \in (-\infty, \infty)$. Finally, we take the difference of these two integrals to find an expression for ΔI in terms of beam displacement x_B. The necessary integral is given by,

$$\begin{aligned}
&\int_{-\infty}^{0} dx \int_{-\infty}^{+\infty} dy\, e^{-a(x^2+y^2)/w_1^2 - a((x+x_B)^2+y^2)/w_2^2} \\
&= \frac{\pi w_1^2 w_2^2 e^{-a x_B^2/(w_1^2+w_2^2)}}{2\,a(w_1^2+w_2^2)} \\
&\quad \times \left[1 + \mathrm{Erf}\left(\frac{\sqrt{a} x_B}{w_2^2} \sqrt{\frac{w_2^2 w_1^2}{w_1^2+w_2^2}}\right)\right] \\
&\approx \frac{\pi w_1^2 w_2^2}{2\,a(w_1^2+w_2^2)} \\
&\quad \times \left(1 + \frac{2}{\sqrt{\pi}} \cdot \frac{\sqrt{a} x_B}{w_2} \sqrt{\frac{w_1^2}{w_1^2+w_2^2}} + \ldots\right),
\end{aligned} \tag{A4}$$

where a is a constant and $a = 2$ for the integrals performed here. The result has been expanded to linear order in x_B, because we expect $x_B/w_i \ll 1$. The result of this calculation is,

$$\frac{\Delta I}{x_B} = 4\xi \sqrt{\frac{\mathcal{P}_1 \mathcal{P}_2}{4\pi}} \frac{w_1^2}{(w_1^2+w_2^2)^{3/2}} \cos[\Delta\omega t + \Delta\phi], \tag{A5}$$

where we have related the peak electric field in a Gaussian beam to its total power by

integrating the irradiance of a single, ideal Gaussian beam which yields $\mathcal{P} = \frac{1}{4}\pi c\epsilon E_o^2 w_o^2$.

Finally, we can find Eq. (4.2) by using Eqs. (A1) and (A5) and the harmonic-oscillator assumption that $F_{\rm opt} = kx_{\rm MS}$ with k being the trap spring constant,

$$\frac{\Delta I}{x_{\rm MS}} = \frac{\Delta I}{x_B}\left(\frac{x_B}{x_{\rm MS}}\right) = \frac{\Delta I}{x_B}\left(\frac{\frac{F_{\rm opt}cd}{\mathcal{P}_2}}{\frac{F_{\rm opt}}{k}}\right) = \frac{\Delta I}{x_B}\cdot\frac{kcd}{\mathcal{P}_2}, \tag{A6}$$

which yields the result quoted in Sec. III.

2. Radial-displacement noise

In this section we compute the radial-displacement noise quoted in Sec. IV, which is a far more simple calculation. We assume that the radial displacement noise is simply the photocurrent shot noise multiplied by the square of the radial-displacement calibration computed previously.

The photocurrent shot noise is given by Schottky's result, $S_{shot} = 2eI$ [132], with e being the fundamental charge and I the mean photocurrent. Computing directly,

$$\begin{aligned} S_{xx} &= S_{shot}\cdot\left(\frac{x_{\rm MS}}{\Delta I}\right)^2 \\ &= (2eI)\cdot\left(\sqrt{\frac{4\pi}{\mathcal{P}_1\mathcal{P}_2}}\frac{\mathcal{P}_2}{4\,\xi\,k\,d\,c}\frac{(w_1^2+w_2^2)^{3/2}}{w_1^2}\right)^2 \\ &= (2e\xi(\mathcal{P}_1+\mathcal{P}_2))\cdot\left(\frac{\pi\mathcal{P}_2}{4\,\mathcal{P}_1\,(\xi kdc)^2}\frac{(w_1^2+w_2^2)^3}{w_1^4}\right) \\ &= \frac{\pi e\mathcal{P}_2}{2\xi\mathcal{P}_1}\frac{(w_1^2+w_2^2)^3}{w_1^4k^2d^2c^2}(\mathcal{P}_1+\mathcal{P}_2) \end{aligned} \tag{A7}$$

where we have dropped the portion of $(\Delta I/x_{\rm MS})$ that oscillates in time, since we measure the amplitude of the interference. This is exactly the result quoted in Sec. IV.

3. Axial-displacement noise

Our expression for axial-displacement noise is derived from error propagation. The axial signal is determined by comparing the ratio of neighboring samples of the interference signal generated by light reflected from the MS. Because $f_{ADC} = 4\cdot f_{IF}$, with f_{ADC} being the sampling frequency and f_{IF} in the interference frequency, the arc tangent of

this ratio can be interpreted as the phase, ϕ, of the signal and can be averaged over many cycles of the interference.

Let the z signal be given by,

$$z_{\mathrm{MS}} = \frac{\lambda/2}{2\pi}\mathrm{atan}\left[\frac{A_i}{A_{i\pm1}}\right], \tag{A8}$$

where λ is the wavelength of light and the prefactor relates path-length changes, due to MS motion, to the phase of the back reflection, and thus the phase of the interference signal. A_i are neighboring voltage samples with shot noise spectral density $S_{A_i} = G_z^2 R_{t,z}^2 (2eI)$, with G_z being the z electronics gain and $R_{t,z}$ the z transimpedance. We assume the variance of the signal z_{MS} can be given directly by propagating errors,

$$\begin{aligned} S_{zz} &= \left|\frac{\partial z_{\mathrm{MS}}}{\partial A_i}\right|^2 S_{A_i} + \left|\frac{\partial z_{\mathrm{MS}}}{\partial A_{i\pm1}}\right|^2 S_{A_{i\pm1}}, \\ &= \left(\frac{\lambda/2}{2\pi}\right)^2 2G_z^2 R_{t,z}^2 eI\left[\left(\frac{1}{\left(1+\frac{A_i^2}{A_{i\pm1}^2}\right)A_{i\pm1}}\right)^2\right. \\ &\quad \left. + \left(\frac{A_i}{\left(1+\frac{A_i^2}{A_{i\pm1}^2}\right)A_{i\pm1}^2}\right)^2\right] \\ &= \left(\frac{\lambda}{4\pi}\right)^2 \frac{2G_z^2 R_{t,z}^2 e\xi(\mathcal{P}_A+\mathcal{P}_B)}{A_i^2 + A_{i\pm1}^2}, \end{aligned} \tag{A9}$$

where $\mathcal{P}_A$ and $\mathcal{P}_B$ are the power of the back-reflected and reference beams, respectively, although the result is symmetric with regard to these powers.

The signal samples A_i are voltage amplitudes of the interference signal, sampled every quarter wavelength, and can thus be expressed as,

$$A_i = 4G_z R_{t,z}\xi\sqrt{\mathcal{P}_A\mathcal{P}_B}\begin{cases} \sin(\phi) & i = 1,5,\ldots \\ -\cos(\phi) & i = 2,6,\ldots \\ -\sin(\phi) & i = 3,7,\ldots \\ \cos(\phi) & i = 4,8,\ldots, \end{cases} \tag{A10}$$

which assumes perfect mode matching. The coefficient can be derived from Eq. A3 without displacing one of the beams, using identical waists and converting current to voltage. Substituting these expressions and noting $\sin^2{+}\cos^2{=}1$,

$$S_{zz} = \left(\frac{\lambda}{4\pi}\right)^2 \frac{e(\mathcal{P}_A + \mathcal{P}_B)}{8\xi \mathcal{P}_A \mathcal{P}_B}, \tag{A11}$$

we immediately find the result quoted in Sec. IV.

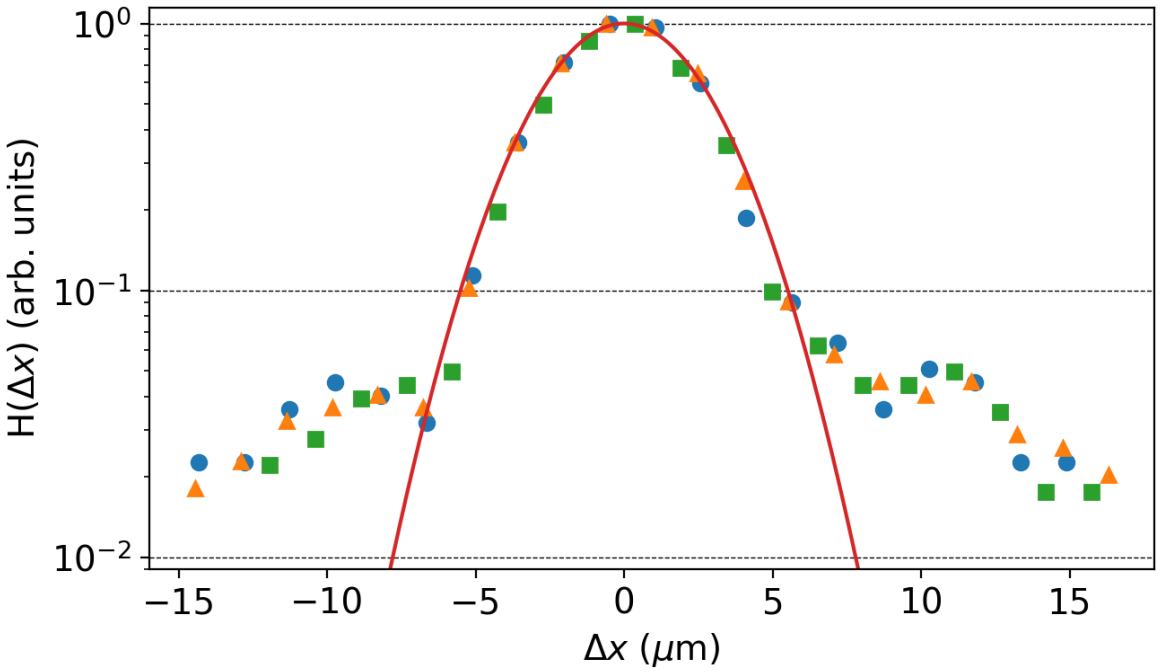

Figure 4.4: Interference contrast vs radial position in the focal plane of the trap, for three distinct sets of measurements, taken for consistency, and shown with differing marker shapes. The solid curve represents the prediction of Eq. (4.5) calculated with the measured beam waists and known focal length. Data is normalized to a maximum of one and centered. The width of the predicted profile is not fit to data. The non-Gaussian tails in the data are likely the result of the halo in the trapping beam, as seen in Fig. 4.2.

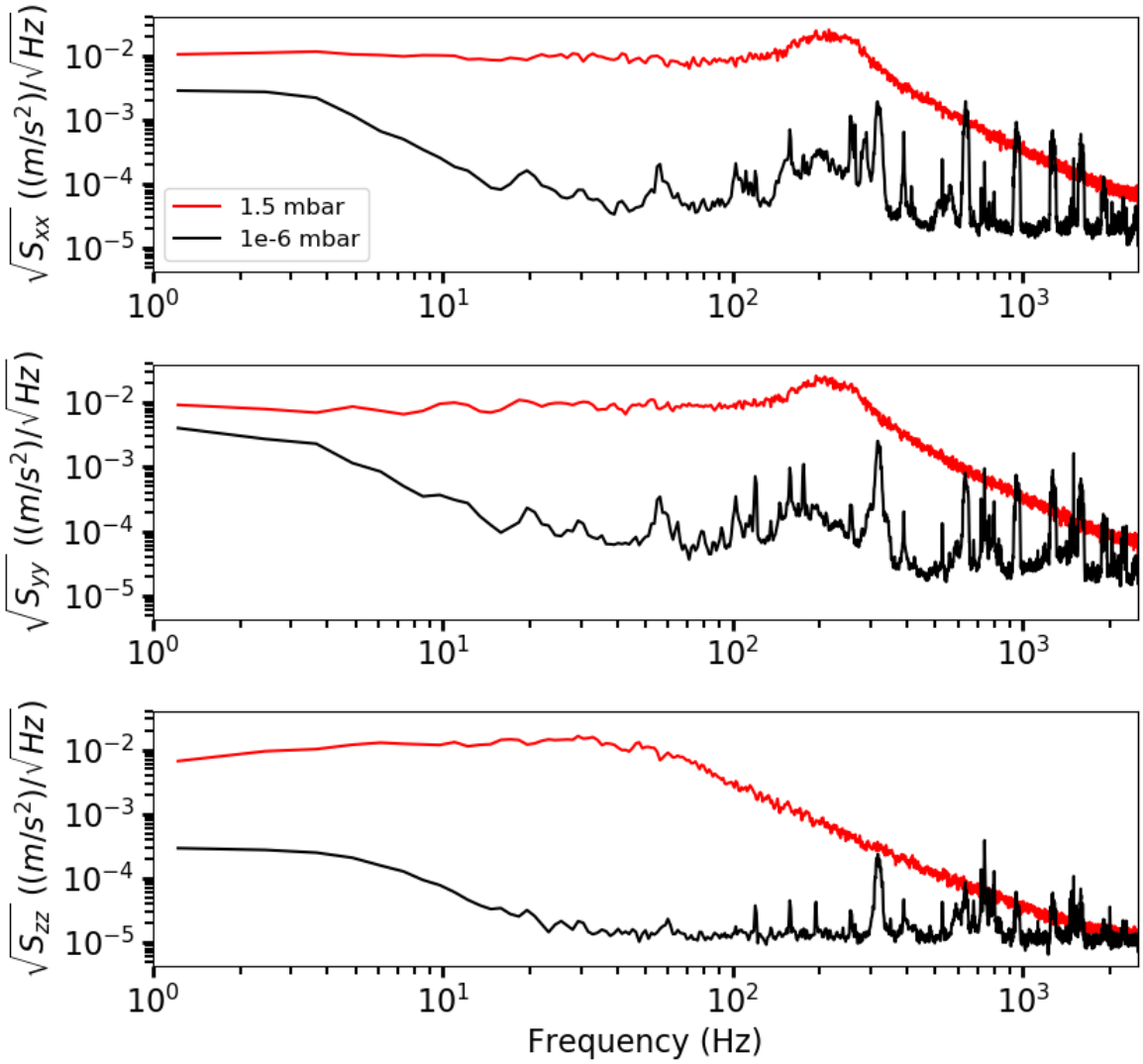

Figure 4.5: Acceleration spectral densities for each of the three DOFs for a MS in the trap at 1.5 and 10^{-6} mbar of residual gas, with feedback cooling active for the latter case. The data for both axial and radial DOFs were calibrated into physical units following the procedure discussed in Sec. III. The curves for 10^{-6} mbar pressure are directly proportional to the displacement noise with a MS, displayed in Fig. 4.3.

Table 4.1: Comparison of reported radial-displacement and -acceleration noise, in a variety of optical trapping apparatuses using MSs with diameters $> 0.3\,\mu$m. Cases designed for smaller MS are not included since they are not optimized for acceleration sensitivity. The figures reported in [1] are extracted from the case with a MS in their trap, in order to provide a valid comparison. Shown are: the MS radius R, the trap frequency $f = \Omega/(2\pi)$, the displacement noise σ_x, and acceleration noise σ_a in a frequency band (f_1, f_2). The radial DOFs are chosen here, because they are more relevant for force-sensing programs.

Ref.	R (μm)	f (kHz)	σ_x (m/$\sqrt{\text{Hz}}$)	σ_a [(m/s^2)/$\sqrt{\text{Hz}}$]	(f_1, f_2) (kHz)
This work	2.4	0.25	3.1×10^{-11}	7.5×10^{-5}	(0.01,0.1)
[1]	1.5	9.1	1.4×10^{-13}	4.6×10^{-4}	(1,10)
[124]	1.5	1.0	2.0×10^{-10}	7.7×10^{-3}	(0.01,1)
[125]	0.15	2.8	1.8×10^{-10}	5.7×10^{-2}	(0.01,3)

Chapter 5

Three dimensional force-field microscopy

5.1 Statement of the Author's Contribution

The following chapter closely follows what was published in [45]. This work is important because it demonstrated force measurements in close proximity to a solid object enabled by a single beam trap. The author of this thesis played a role in this work by developing the apparatus, fabricating the devices used for the measurement, developing techniques for measuring electrostatic forces with charged microspheres, and collecting data.

5.2 Introduction

The ability to make measurements at ever smaller length scales has had profound implications for both fundamental science and technology. In particular, atomic force microscopy has enabled the measurement and manipulation of surfaces at atomic length scales. Traditionally, atomic force microscopes (AFMs) have sensed the interaction of a tip, suspended by a cantilever, with a surface, by measuring the displacements of the cantilever in the direction perpendicular to its surface [22]. The mechanical suspension of the force sensing element limits electrical, thermal, and

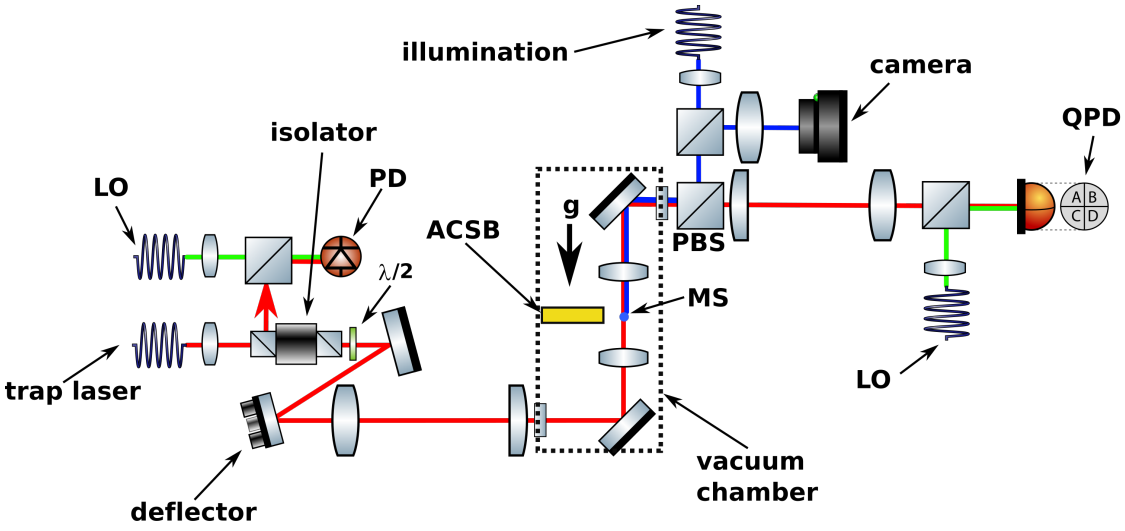

Figure 5.1: Schematic view of the free-space optical system. The output of the optical fiber carrying the trapping beam is first collimated, then deflected by a high-bandwidth ($f_{-3\mathrm{dB}}$ ∼1 kHz) piezo-mounted mirror in the fourier plane of the trap, which produces translations at the trap position. Two aspheric lenses inside the vacuum chamber focus the trapping beam and re-collimate the light transmitted through the MS. The transmitted beam is then interfered, on a quadrant photodiode (QPD), with a local oscillator (LO) beam, whose frequency is shifted by 500 kHz with respect to the trapping beam. Light backscattered by the MS is extracted, combined with another LO beam and used to interferometrically measure the axial position of the MS. All components are only shown schematically and are not drawn to scale. PD: photodiode, PBS: polarizing beam splitter, $\lambda/2$: half-wave plate.

mechanical isolation from the outside world.

Here we present a technique for measuring three-dimensional forces over a three-dimensional volume by levitating a 4.8 μm-diameter dielectric microsphere (MS) at the focus of a Gaussian laser beam, with a ∼10 μm minimum distance between the center of the MS and another object. This results in the full mapping of a vector field anywhere in space and close to mechanical objects. The optical levitation enables three important features: the absence of dissipation associated with the cantilever support allows measurements with substantially lower force noise at room temperature; the electric isolation provided by the optical support makes electrostatic measurements at fixed charge possible; and force vectors measured in three dimensions

are characterized by similar spring constants in each of the three trapping degrees of freedom (DOFs).

Since the pioneering work of Ashkin [24, 49, 133], a number of experiments with optically levitated MSs have been demonstrated, especially in recent years [1, 17, 42, 46, 47, 51, 52, 73, 74, 113, 115–119, 123–127, 134, 135]. Some authors have proposed short-range force detection experiments using their optically levitated MSs [32, 114], but only a few have actually positioned free-standing objects micrometers away from a trapped MS [47, 135], or other mesoscopic objects. Positioning a Si beam or other attractor close to a trapped MS, and measuring its effect on the trapped MS, is crucial for any short-range force sensing application.

As a demonstration of this technique, we measure the electrostatic forces between a charged MS and an Au-coated Si beam (ACSB) structure. A force calibration, obtained by charging the MS with a unity charge and applying an external electric field, allows us to precisely determine the electric field due to a overall bias on the ACSB as well as infer the distribution of "patch potentials" on the Au surface in absolute terms.

5.3 Experimental Setup

The optical trap used here is almost identical to that described in [17]. The optical system is shown schematically in Fig. 5.1. The trap is formed at the focus of a Gaussian beam generated by a 1064 nm laser, whereby the radiation pressure and Earth's gravity create a stable three-dimensional harmonic trap. Silica MSs of 4.80 ± 0.04 μm diameter [128] are applied to the bottom side of a glass coverslip, where they adhere by van der Waals forces. The MSs are loaded into the trap by vibrating the glass slide, placed about 10 mm above the trap, with a piezoelectric transducer. For this operation, the vacuum chamber is maintained at a pressure of 2 mbar of N_2 buffer gas to slow the fall of the MSs and provide sufficient damping of their motion within the trap. After loading one MS, the glass slide is withdrawn in order to minimize distortions to the trapping beam, which is also used for applying optical feedbacks and measuring forces. The N_2 gas is then gradually pumped out, reaching a final

pressure of $\sim 10^{-6}$ mbar for the measurements.

The trap becomes unstable below pressures of $\sim$0.1 mbar, because of insufficient gas damping. To stabilize the trap under high vacuum conditions, optical feedback forces are applied to the MS. The radial DOFs are stabilized using a piezoelectrically actuated deflection mirror placed in a Fourier plane of the trap, while the axial DOF is stabilized by modulating the power of the laser with an acousto-optic modulator. The optical readout system used in the feedback for the three DOFs closely follows [17] with significant improvements made to the electronics. The single beam configuration of the apparatus is ideal for the application described here, as it allows optimal access to the MS from all directions in the horizonal plane. The current noise level on the motion of the MSs is dominated by effects [17] other than the residual vacuum, which is limited by a number of non UHV-compatible translation stages.

The trap region is illustrated in Fig. 5.2. To minimize long-range electrostatic interactions, this region is shielded inside a Faraday cage consisting of six hollow, pyramidal electrodes that can be independently biased. The two electrodes on the vertical axis hold the aspheric lenses, while shielding the trap region from their, potentially charged, dielectric surfaces. MSs loaded in the trap are generally charged. Ultraviolet light from a xenon flash-lamp, brought in the trap region by an optical fiber, is used to discharge the MSs, while their charge state is monitored by applying an AC voltage to two opposing pyramidal electrodes. As demonstrated in [46], this process can be used to verify with extremely high confidence that the MS is overall neutral.

The force sensitivity of the system is calibrated for each MS with the same process, typically when a charge excess of $1e$ is reached, where e is the elementary charge. The calibration procedure, described in [17, 46, 47], can independently measure the force response along the three coordinate axes, by employing, in turn, different electrode pairs. Small corrections from the fringe field due to the shape of the electrodes are calculated and accounted for using finite element calculations and the full model of the electrode arrangement. The MS response is frequency-dependent, with a natural, radial resonant frequency of $\sim$400 Hz, and is measured over the range $1 - 600$ Hz.

Once a force calibration has been obtained, the charge state of the MS can be

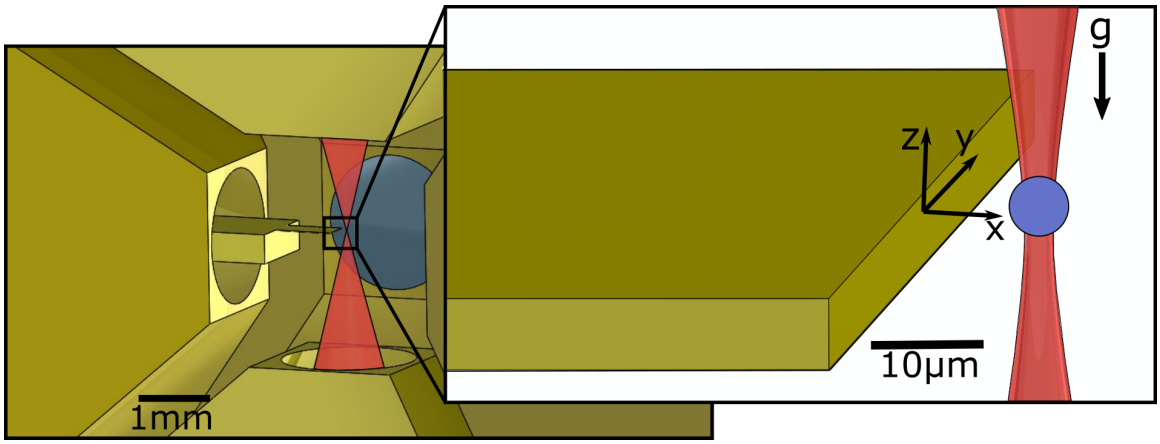

Figure 5.2: Trap region: a drawing of the trap region is shown in the left panel, illustrating the 2 mm diameter holes in the Au-coated pyramidal shielding electrodes through which the ACSB and the trapping beam are brought in and extracted. The trapping light is represented by the red conical feature. The panel to the right illustrates a detail of the end of the ACSB, and trapped MS, along with the coordinate frame used in the data analysis. A separate arrow shows the direction of Earth's gravity. The alternating Au-Si structure buried under the Au coating is inessential for the present work and not shown.

arbitrarily set, for the purpose of electrostatic force sensing. Continued exposure to UV flashes produces a net positive charge, while flashing the same UV light onto a nearby Au surface produces free electrons, some of which become bound to the MS, generating a net negative charge. Both charging mechanisms occur simultaneously, although the relative rates, and thus the charging direction, can be controlled by bringing the ACSB (an Au surface) close to the MS, or removing it to a distant location. This flexibility and the demonstrated indefinite stability of charge states, affords a large dynamic range in force sensing applications. For electric field mapping discussed here, the MS is charged to approximately $q \approx -400e$, with an excess of electrons. This large charge is intended to overwhelm possible multi-polar (mainly dipolar) effects, clearly visible for neutral MSs.

We assume this charging procedure does not produce a large permanent dipole moment via localized charging of the MS. A dipole moment of $d \approx 500\ e \cdot 5\ \mu$m (aligned for maximal coupling to the field gradient), produces a force that is an order

of magnitude smaller than the force on a charge of $q \approx 500e$ in the electric field configuration employed here (discussed below).

5.4 Measurements and Results

The ACSB is designed to have contrast in density (and baryon number) for a future experiment. This is achieved by alternating Au and Si fingers with 25 μm distance between the centers of contiguous fingers. A 3 μm thick Si fence bridges all Si fingers together, so that the Au fingers are entirely surrounded by Si. A 200 nm Au coating is then applied to all surfaces. A more complete description of the ACSB is provided elsewhere [136], while, for the purpose of the work described here, only this external layer of Au is relevant. The ACSB is 10 μm thick to minimize its interference with the tails of the Gaussian trapping beam. More work on both shaping of the trapping beam and the MS imaging system are likely to make thicker field-generating components possible; nevertheless, constraints of this type are likely to remain the main limitation of this new technique.

The ACSB can be biased independently from other components and is mounted off a three-axis, piezoelectric translational nanopositioning stage. After trap loading and force calibration, the ACSB is brought close to the trap region through one of the small holes in the pyramidal electrodes, as shown in Fig. 5.2, where the coordinate system employed here is defined. Sufficient clearance is provided for the full 80 μm range of the translation stage in the y and z directions.

Force measurements are carried out in three configurations: to evaluate the noise and linearity of the measurement, to demonstrate the ability of the technique to map the field produced by an external bias on the ACSB, and to map the field produced by patch potentials on the ACSB surface.

5.4.1 Sensor Linearity and Noise

There are two features that define the performance of a force sensor: noise and linearity. The linearity of the force measurement is obtained, along the three DOFs,

by the same process used for the force calibration, scanning the AC drive signal from (0 ± 0.1) fN to 500 fN. The result, for forces along the x axis, is shown in Fig. 5.3, along with the residuals to a perfectly linear behavior. At driving forces over 300 fN a $\sim$10% nonlinearity is observed.

The noise is characterized by collecting data with the ACSB placed over a 3-dimensional grid of positions in front of a trapped and charged MS. The six trapping electrodes are nominally grounded and the ACSB is driven with a single frequency AC voltage at 41 Hz. We then examine the response of the MS at a frequency far from this applied tone. We observe similar noise conditions when the ACSB is

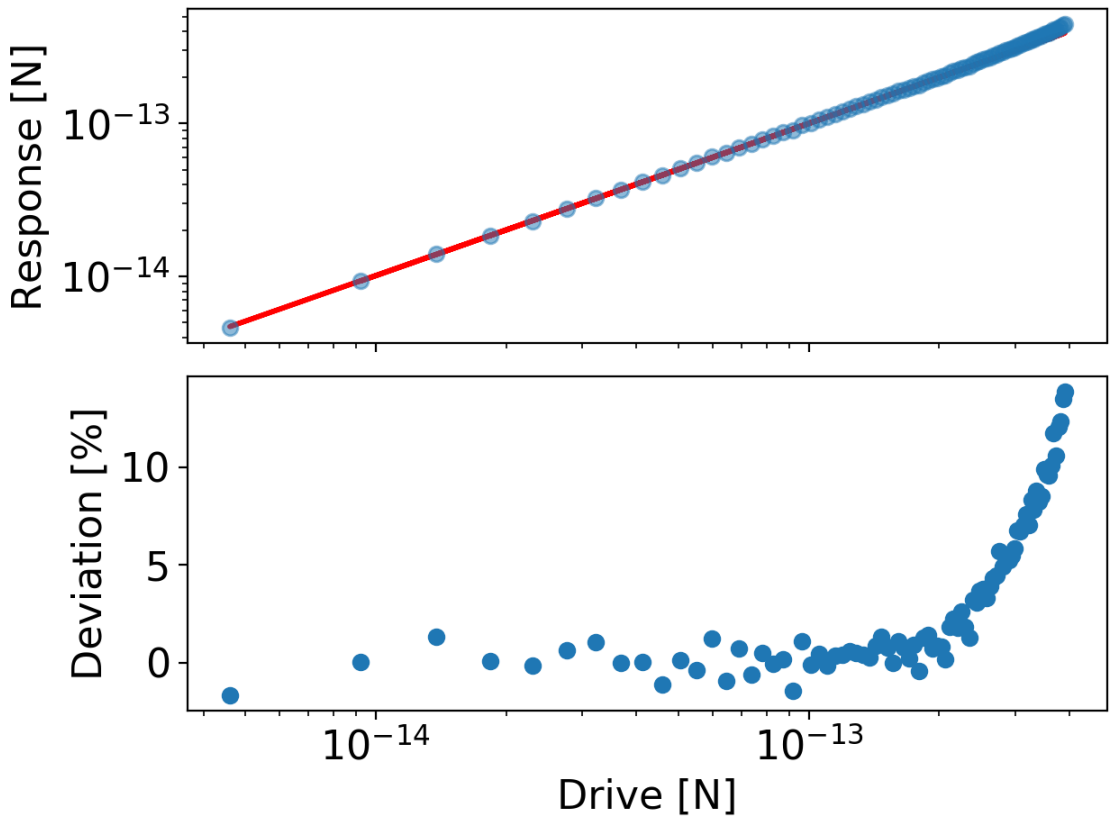

Figure 5.3: Linearity of the force sensor in the x-direction. The other two DOFs have comparable linearity. The low noise and high linearity of the apparatus enable measurements with a dynamic range of over four orders of magnitude.

nominally grounded. The resulting force micrographs are shown in Fig. 5.4 for 10 s integrations at each position and with a single MS. The rms noise forces over the whole $80 \times 80 \times 80$ μm^3 measurement volume are 5.5 aN, 17.3 aN, and 8.2 aN, for the x, y, and z directions, respectively. Histograms of the noise over the whole measurement volume are plotted in Fig. 5.5. The anisotropy in the measured noise may be the result of residual astigmatism of the trapping beam, inconsistencies in x and y feedback, or, possibly, effects related to the finite geometry of the ACSB [137, 138]. This force noise is comparable to a cryogenic Si cantilever [139, 140], but is obtained at room temperature and on all three DOFs simultaneously. This noise performance, along with the linearity up to $\sim 10^{-13}$ N, enables force measurements spanning over four orders of magnitude in amplitude.

5.4.2 Electric Field From an Overall Bias Voltage

The overall electric field from a bias voltage applied to the ACSB is measured. This procedure is used here to validate the technique, but also to register the relative position of the ACSB to the trap and its orientation in space, with a fit to a model produced by finite-element analysis (FEA). In a new version of the trap, currently under construction, high quality metrology will be possible through auxiliary optics, something only available in a rudimentary fashion in the current system.

The three-dimensional electric field is mapped over a $10 \times 10 \times 10$ grid of points, spanning the the full 80 μm of closed-loop travel in the translation stage, along each of its three orthogonal axes. The relative displacement between points in the three-dimensional scan is known with an uncertainty of $\sim$10 nm, set by the accuracy of the translation stage used. To perform the measurement at each point on this grid, the MS is driven for 10 s by an AC-voltage on the ACSB at 41 Hz, with a 100 mV peak-peak amplitude. The force at each grid point is represented by a three-dimensional vector. A slice of this vector field along an $x - z$ plane at $y = 0$ (centered along the y axis) is shown in Fig. 5.6, together with the results of the FEA. Shown are both F_x and F_z (top), and F_y and F_z (bottom) in the same $x - z$ plane.

The data is fit to the FEA model by constructing a least-squared cost function

from the difference between them, normalized by the error in the data, and summed over all 1000 grid locations. In the minimization, the charge of the microsphere, q is allowed to float (which is equivalent to applying an overall scaling of the $\mathbf{E}$ field produced by ACSB), as well as three translations of the coordinates reported by the stage, and six independent rotation angles. Three of these angles floated in the fit represent angular misalignment between the axes of the translation stage and the axes of the trap, which are used to construct a rotation matrix applied to the measurement grid points. The remaining three angles account for a possible angular misalignment of the ACSB itself to the axes of the translation stage, and are used to construct a rotation matrix applied to the measured vector field. We exclude constant offsets in the measured force, as would arise from contact potentials, since we apply an AC electric field and measure the amplitude and phase of the MS's response.

With this procedure, we find $q = -459e$ (consistent with the estimate made during the charging process), and a closest separation of the ACSB face of 15 μm from the center of the MS, centered in the z-axis with an uncertainty ± 2.5 μm. The coordinate axes of the ACSB are found to be tilted relative to the coordinate axes of the translation stage by no more than $\pm 5^\circ$ for all three rotation angles, while the coordinate axes of the translation stage are tilted relative to the physical axes of the trap by no more than $\pm 2^\circ$ for all three rotation angles.

Residual deviations from the best-fit FEA, particularly apparent at short separations, are likely the result of non-uniformity of the voltage on the ACSB, as our FEA assumes a perfect conductor with ideal geometry. Small dielectric particles (e.g. silica dust) on the surface of the ACSB, and/or metallic grains in the Au coating, may contribute to the small discrepancies observed at shorter distances [141, 142]. Permament dipole moments in the MS, estimated from [47], may produce forces more than an order of magnitude smaller than the residual force from the fit described above. Similarly, induced dipoles, estimated from the MS index of refraction [128] and the contact potential on the ACSB assumed to be < 100 mV, may produce a force more than two orders of magnitude smaller than the residuals.

The closest approach of the ACSB, as described above, is 15 μm for the dataset shown in in Fig. 5.6. Force sensing at smaller distances, down to ~ 8 μm, are possible

and have been achieved with this technique, but with an increase of the system noise for which a satisfactory explanation has not been found.

5.4.3 Patch Potential Measurements

Patch potentials on the surface of the 200 nm thick evaporated Au surface of the ACSB create an electric field which can be measured as a force on a charged MS. To perform this measurement, the ACSB is mechanically driven sinusoidally along the y-axis with the translation stage, over a regular grid of x positions (separations), and z positions. At each point within the $x-z$ grid, $\mathbf{F}(t)$ and $y(t)$ are measured, so that the three-dimensional force field $\mathbf{F}(x,y,z)$ can be obtained. The relative registration of the MS with respect to the ACSB in terms of the three translations and six rotations is taken from the fit to the case of the biased ACSB, discussed in the previous section. The three-dimensional electric field can then be extracted as $\mathbf{E}(x,y,z) = \mathbf{F}(x,y,z)/q$, where q is the charge of the MS, also determined in the previous section.

The electric field due to patch potentials on the ACSB is numerically modeled following results obtained by Kelvin probe atomic force microscopy [16, 142]. The authors define a voltage autocorrelation function, $R(\mathbf{s}) = \int\int d^2\mathbf{s}' V(\mathbf{s})V(\mathbf{s}'+\mathbf{s})$, where $\mathbf{s}$ and $\mathbf{s}'$ and positions on the surface. They then find that $R(\mathbf{s})$ is approximately constant for short length scales, followed by a sharp knee at a length scale consistent with the expected patch size, l_{patch}. As an approximation to this autocorrelation function, we model triangular patches measuring l_{patch} on a side, with voltages randomly sampled from a normal distribution, $N(0, V_{\text{patch}})$. FEA is used to determine the electric field due to these patches (as the geometry and boundary conditions do not permit an analytic solution), which we then compare to our data. Since the patches and resulting electric fields are random, we create many realizations of patches to sample the mean and variance of the root-mean-square (rms) force, F_{rms}.

Measurements of F_{rms} along x and y for different separations x, are shown in Fig. 5.7. The rms is computed over all grid points along the y axis, at $z = 0$. In the figure, the data is fit to the results of the FEA model described above using a least-squared cost function, with a constant added variance to account for noise.

By detrending the MS response along the y axis, this measurement is insensitive to contact potentials on the ACSB. At distances much greater than the patch size, the rms $\mathbf{E}$ field is proportional to the product of the patch length scale, l_{patch}, and the rms patch voltage, V_{patch}. Although the MS is not close enough to the ACSB to resolve the underlying patches, we are able to extract the patch length-scale voltage product.

To compare to other measurements, we assume $V_{\text{patch}} = 100$ mV [15, 16], and obtain l_{patch}. Our fit of the x rms (y rms) force implies $l_{\text{patch}} = 0.8$ μm ($l_{\text{patch}} = 0.7$ μm). The length scales inferred from the fit are somewhat larger than the $\sim$200 nm grain size expected for a 200 nm thick evaporated Au film [15, 16]. Others have observed sample contamination by dielectric adsorbates (such as silica dust) that become embedded in metallic surfaces, which can collect charge and affect measurements of patch potentials [141, 142]. Finite electrode geometry may also play a role [138].

5.5 Conclusions

We have demonstrated a technique capable of mapping, with sensitivity competitive to that of cryogenic AFM, a three-dimensional vector field over a volume of $\sim 10^6$ μm^3 in free space. The center of this sensor, a 4.8 μm diameter optically levitated dielectric microsphere, can be brought closer than 10 μm from a metallic surface, while performing the measurement. This novel instrument is used to map the patch potentials on an Au surface.

While this first result is exclusively sensitive to electric fields, three-dimensional mapping of other physical fields appears possible. Magnetized microspheres are commercially available, and, possibly, neutral microspheres or microrods with large electric dipole moments could be used with enhanced sensitivity to electric field gradients. Our group is actively pursuing the technique to search for new long-range interaction coupling to mass or other intrinsic properties of matter at the micrometer scale.

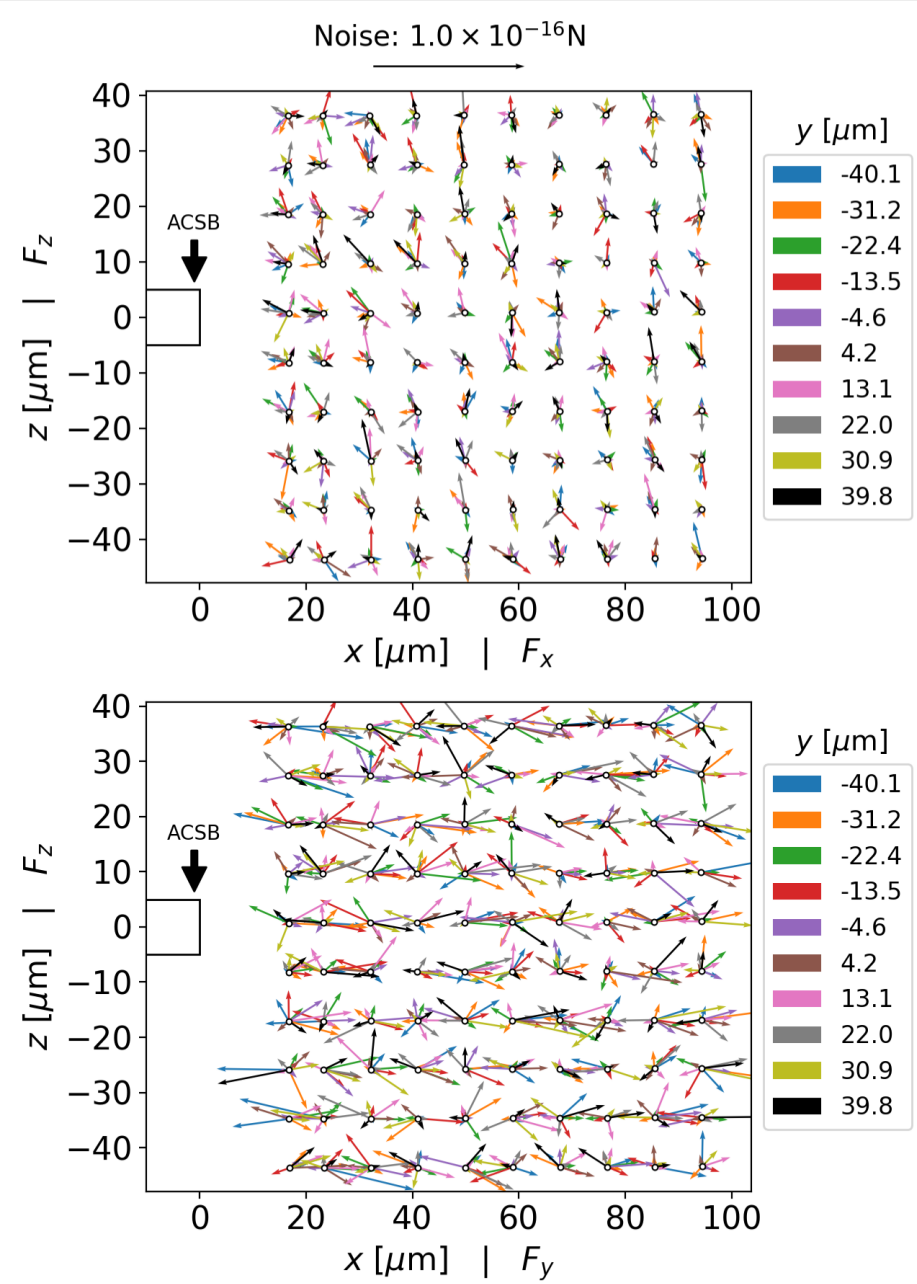

Figure 5.4: Noise micrographs with a charged MS, taken in the presence of a stationary ACSB. The force vectors represent the MS response at a frequency far from a single-frequency AC voltage drive applied to the ACSB during these measurements. For the data in the top (bottom) panel, the force vector on the horizontal axis represents F_x, the force in the x direction (F_y, the force in the y direction). In both cases, force vectors measured at ten y positions (with a different color indicating each y position shown in the legend) in a regularly spaced grid ranging from -40 μm to 40 μm are plotted at each (x, z) location.

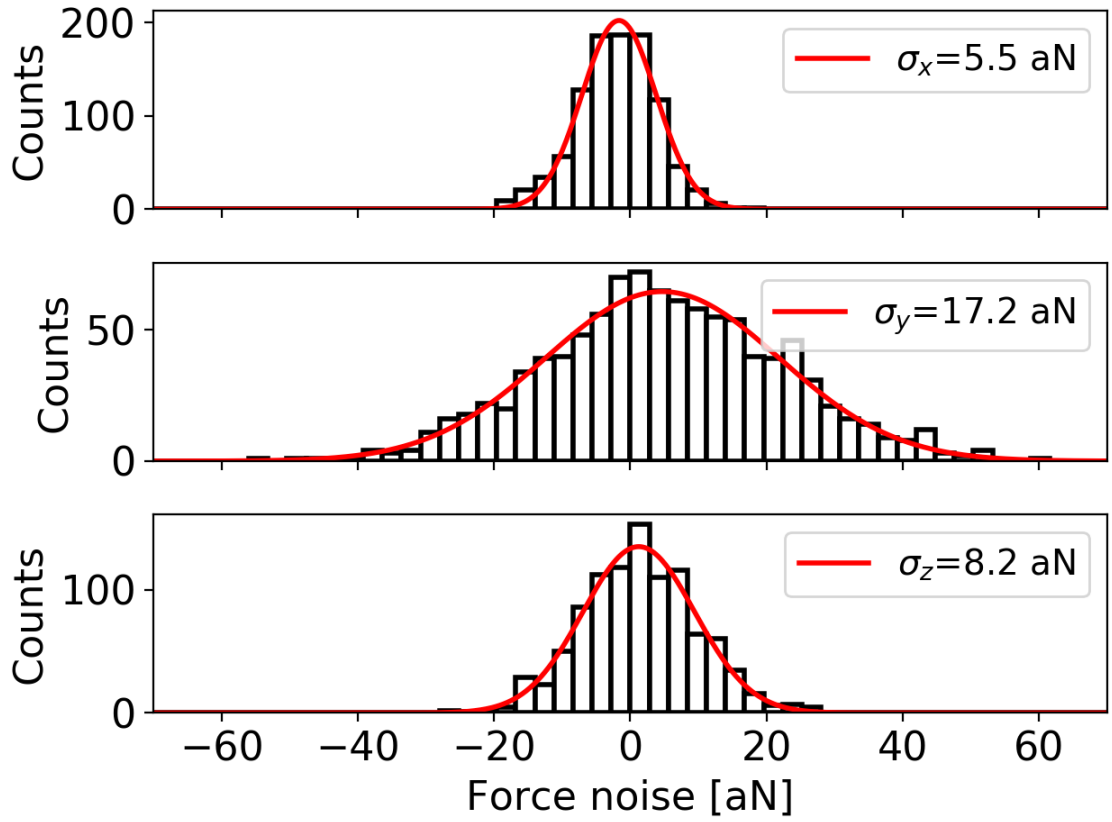

Figure 5.5: From top to bottom: histograms of the measured force noise in the x, y, and z directions at different grid locations. Also shown are the fits to normal distributions.

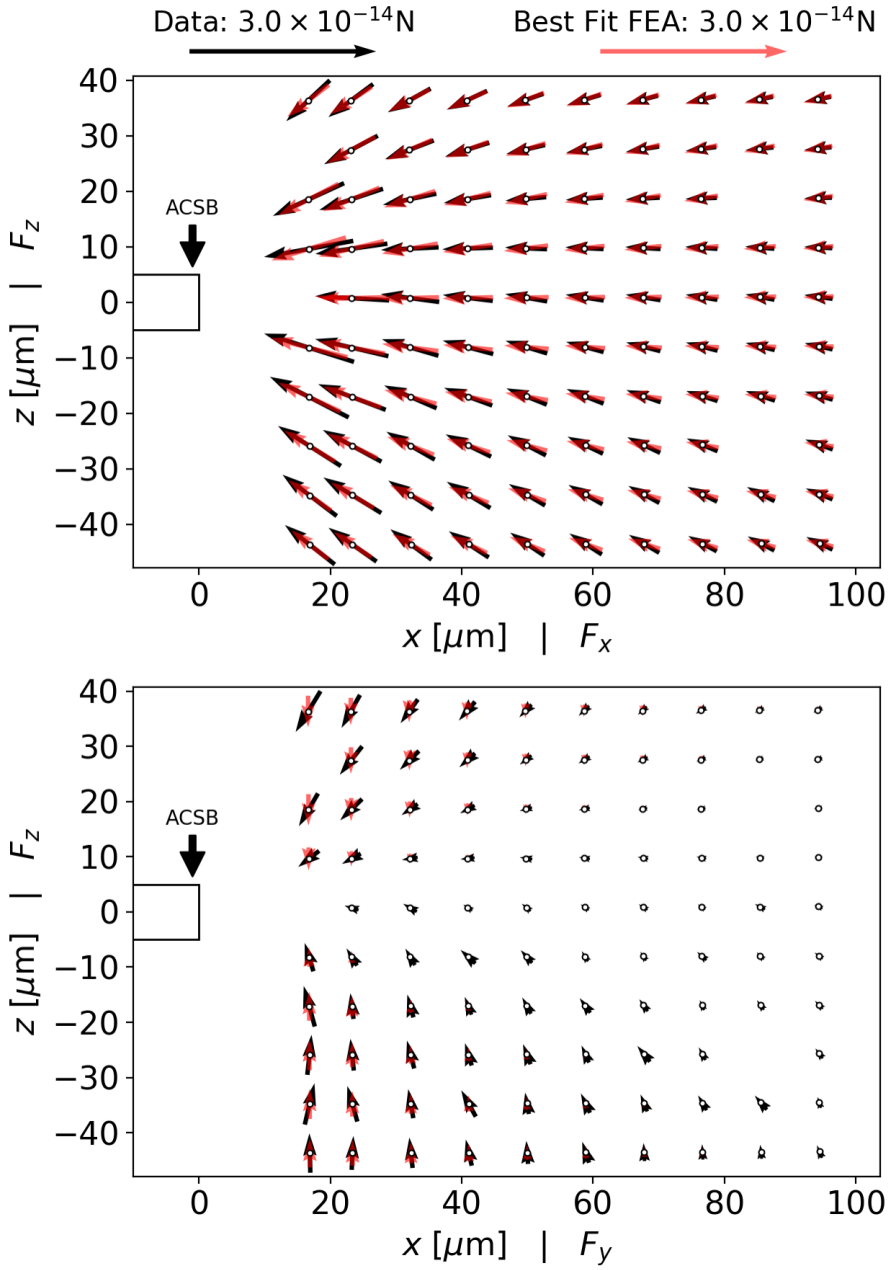

Figure 5.6: Vector field plots of (F_x, F_z), top, and (F_y, F_z), bottom, in an $x-z$ plane. The black arrows represent the measured force, while the red arrows represent the best fit from the FEA of the **E** field produced by a ACSB with the same overall bias voltage as in the experiment. A few grid points are missing, due to data corruption introduced by the DAQ instrumentation.

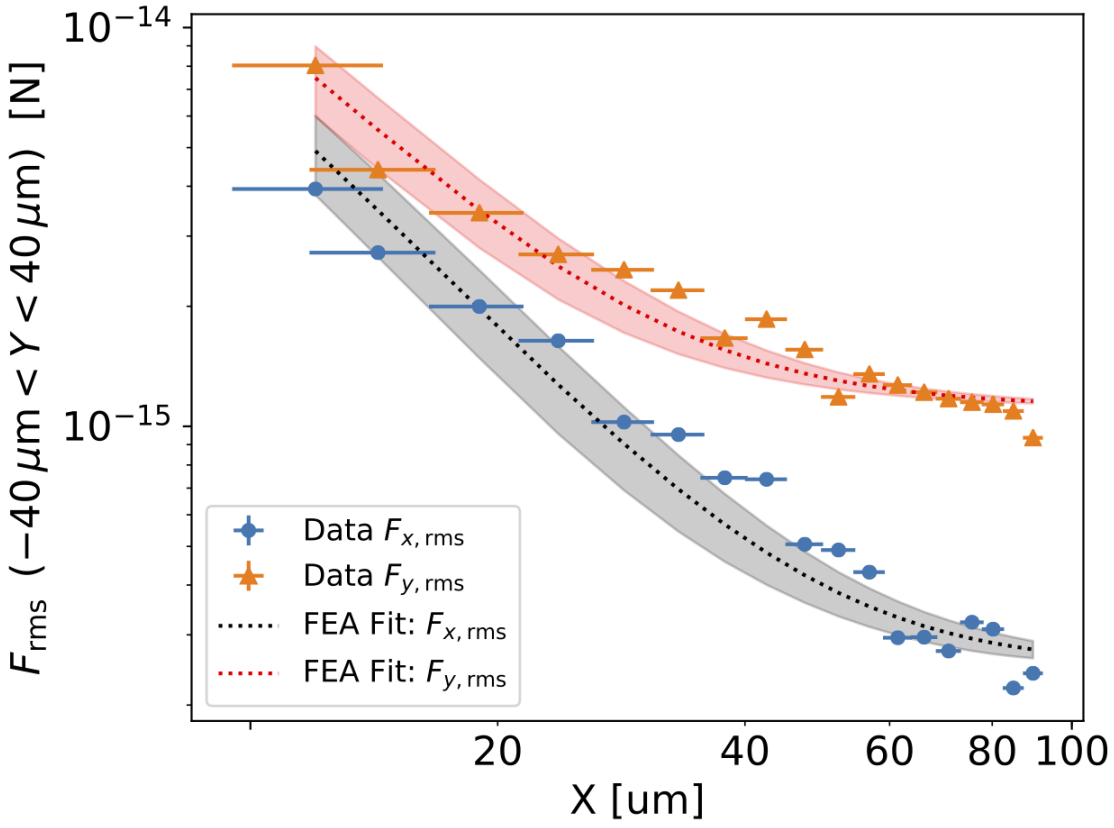

Figure 5.7: The rms of the x and y components of the measured force on the MS in the plane of the ACSB, as a function of separation from the ACSB. The data is compared to a model described in the text. The bands represents the standard deviation of the model, using different random implementations of the patch potentials. The fit of $F_{x,\mathrm{rms}}$ ($F_{y,\mathrm{rms}}$) implies voltage patches of size $\sim$0.8 μm ($\sim$0.7 μm), asssuming $V_{\mathrm{patch}} = 100$ mV [15, 16].

Chapter 6

Optically Levitated Micro-Gyroscopes

6.1 Statement of the Author's Contribution

The following chapter closely follows what was published in Ref. [54]. This work is important because it demonstrated a novel technique for manipulating the rotational degrees of freedom of an optically levitated microsphere. The author of this thesis contributed to this work by developing the framework for electrostatic rotation, modifying the apparatus to measure rotation, collecting and analyzing the data, as well as preparing the initial version of the manuscript.

6.2 Introduction

The ability to manipulate microscopic objects has found important applications in science and technology. The interest in optical levitation of dielectric objects in vacuum, pioneered by Ashkin and Dziedzic [133], has grown in recent times, with applications in precision measurements [32, 46, 47, 125, 143, 144], surface science [45] and quantum technology [1, 115, 116, 118, 126, 145–148]. The suggestion was made in [133] that the rotational degrees of freedom (DOFs) of an optically levitated dielectric microsphere (MS) could be manipulated using the angular momentum in circularly polarized light. This has been realized in more recent times [113, 117, 123, 134, 149–151, 151–155, 155–158].

Here we present a complementary technique for manipulating the rotational DOFs of an optically levitated MS by using electric fields to apply a torque to the $|\mathbf{d}| \sim 100\ e{\cdot}\mu$m permanent electric dipole moment [47] found in 2.4-μm radius silica MSs grown using the Stöber process [159]. The orientation of the dipole moment follows the orientation of the driving field so that the angular velocity, $\boldsymbol{\omega}$, can be set in both magnitude and direction [160]. Control of the rotational DOFs is an essential feature of this work, resulting in the ability to explore the dynamics of the system.

The rotational response of a trapped MS, including an applied electric field, is described by the equation of motion:

$$\dot{\mathbf{L}} = \boldsymbol{\mathcal{T}} = \mathbf{d} \times \mathbf{E} - \frac{\beta}{I}\mathbf{L} + \boldsymbol{\mathcal{T}}_{opt}, \tag{6.1}$$

where, $\boldsymbol{\mathcal{T}}$ is the total torque, $\mathbf{d}$ is the electric dipole moment, $\mathbf{E}$ is the electric field, $\mathbf{L}$ is the angular momentum related to the angular velocity by $\boldsymbol{\omega} = \mathbf{L}/I$, β is the rotational damping coefficient, I is the moment of inertia, and $\boldsymbol{\mathcal{T}}_{opt}$ is the optical torque. The part of the optical torque which does not average to zero over a rotation is negligible compared to the electric torques used here [161].

The angular velocity and the rotational phase of the MS are measured optically. As the MS rotates, it couples some of the incident linearly polarized optical power, $\mathcal{P}_0$, into the cross-polarized optical power, $\mathcal{P}_\perp$, according to,

$$\mathcal{P}_\perp = \mathcal{P}_0 \sin\left(\eta/2\right)^2 \sin\phi^2, \tag{6.2}$$

where η is the phase retardation between the fast and slow axes, and ϕ is the angular displacement of the MS relative to an origin in which the fast axis is aligned with the incident polarization [162]. The $\sin\phi^2$ term implies that the phase of the MS is encoded as a modulation of $\mathcal{P}_\perp$, at twice the rotation frequency, ω.

The optical trap is identical to that described in Ref. [17] with the addition of polarization optics to measure the cross-polarized light, $\mathcal{P}_\perp$. One polarizing beam splitter (PBS) is inserted before the trap to define the linear polarization of the incident light, and a second PBS is placed after the trap to extract $\mathcal{P}_\perp$ and measure the rotational phase of the MS. The remainder of the optical system, described in

Ref. [17], is capable of stabilizing the optical trap at high vacuum.

The residual gas pressure is controlled and measured between 2×10^{-6} mbar and 1 mbar. The vacuum pressure is tuned by introducing or removing N_2 gas and is measured by a cold-cathode gauge for pressures below 10^{-4} mbar, a capacitance manometer for pressures between 10^{-4} and 10^{-2} mbar, and a Pirani gauge for pressures between 10^{-3} and 1 mbar. The cold cathode gauge is found to affect the charge the MS, so it is only used to measure the 2×10^{-6} mbar base pressure of the vacuum system after an experiment. The capacitance manometer does not cover the full range of vacuum pressures, so the Pirani gauge is calibrated against the more accurate capacitance manometer, where there is overlap. This system is capable of measuring the pressure to an accuracy of 10% for N_2 over the range of interest [163].

The trapping region of the apparatus is illustrated in Fig. 6.1, which shows a cross-section of the pyramidal electrodes used to apply torquing electric fields to the MS. The six electrodes define a cubic trapping cavity 4 mm on a side. Each electrode is connected to a high-bandwidth, high-voltage amplifier driven by a digitally-synthesized analog signal. This apparatus is capable of producing arbitrary three-dimensional electric fields up to 100 kV/m in magnitude at frequencies as high as 150 kHz. To produce a spinning electric field, a sinusoidal voltage is applied to a set of four electrodes in a plane, with a phase offset of $\pi/2$ between successive electrodes. A finite element analysis (FEA) is used to calculate the electric field. It is found that the x component of the field in the center of the trap, E_x, is well approximated by $E_x = 0.66(\Delta V_x/\Delta x)$, where ΔV_x is the potential difference across a pair of electrodes, and $\Delta x = 4$ mm is the electrode separation. The same statement applies to E_y and E_z.

Before performing a measurement, the MS is discharged as described in Refs. [45, 46, 164]. In addition, the MS is prepared in a state of known angular momentum and rotational phase by dissipating any initial angular velocity using 0.1 mbar of N_2 gas. An electric field rotating at $\omega_0 = 2\pi\cdot(1\text{ Hz})$ with $E = 41$ kV/m is then turned on to align $\mathbf{d}$ with $\mathbf{E}$. The chamber pressure is reduced to the base pressure of the vacuum system and ω_0 is increased at a rate of 100 Hz/s to the desired rotation frequency.

Changes in the rotational dynamics in response to changes in the electric field magnitude and direction, as well as the damping coefficient, β, can then be observed. The data presented here were collected with one specific MS. Similar qualitative behavior is observed with other MSs, and the measured dipole moment is representative of the population.

6.3 Results and Dynamics

A typical amplitude spectrum of $\mathcal{P}_\perp$, in the region around twice the drive frequency, with $\omega = 2\pi\cdot(50\text{ kHz})$ is shown in the top panel of Fig. 6.2. A clear peak which follows the frequency, ω_0, of the electric driving signal is observed at $2\omega_0$. The $\sim$ 10 ppm amplitude modulation caused by rotation of the MS implies that the relative phase retardation of this MS is $\eta \sim 10^{-2}$. The prominent sidebands are caused by harmonic oscillation of the dipole about the electric field, which can be seen by demodulating the phase of $\mathcal{P}_\perp$ relative to the electric field carrier signal as shown in the bottom panel of Fig. 6.2.

After initializing the MS with a definite angular momentum and phase, the conditions can be changed to observe different solutions of the equation of motion. The simplest solution occurs when the drive electric field is switched off, so that only the drag term, $-(\beta/I)\mathbf{L}$, remains in Eq. 6.1 and the initial angular momentum decays according to:

$$\mathbf{L}(t) = e^{-t/\tau}\mathbf{L}(0). \tag{6.3}$$

Here, the damping time τ, is related to the damping coefficient by $\tau = I/\beta$. This decay is illustrated in Fig. 6.3 at the base pressure of the vacuum system (2×10^{-6} mbar). For the first 1000 s, $\omega \gtrsim 150$ krad/s, the drag torque dominates, and the data are well modeled by an exponential decay. As the angular velocity decreases, other torques become more important. The additional torque required to explain the slower decline in angular velocity is $\boldsymbol{\mathcal{T}}' \sim 10^{-23}$ N·m. This torque could be explained by an optical transfer of angular momentum due to a ~100 ppm ellipticity in the 1 mW trapping beam and the observed MS phase retardation, $\eta \sim 10^{-2}$ [161, 165].

The simplest dynamics with the electric dipole interacting with a rotating electric field can be analyzed in the case where the electric field is rotating about a fixed axis with the dipole lying in the same plane as the electric field. In the frame co-rotating with **E**, Eq. 6.1 reduces to an equation of motion for ϕ, the angle between the electric field and the dipole,

$$\ddot{\phi} = -\omega_0 \Omega \sin(\phi) - \frac{1}{\tau}(\omega_0 + \dot{\phi}), \tag{6.4}$$

where,

$$\Omega \equiv d\,E/(I\omega_0). \tag{6.5}$$

For sufficiently low damping, $\tau\Omega > 1$, this equation has an equilibrium solution,

$$\phi_{eq} = -\arcsin\left(\frac{1}{\tau\Omega}\right) = -\arcsin\left(\frac{\beta\omega_0}{d\,E}\right), \tag{6.6}$$

and can be linearized to give harmonic oscillation at the frequency

$$\omega_\phi = \sqrt{\cos(\phi_{eq})\omega_0\Omega} = \sqrt{\cos(\phi_{eq})\frac{E{\cdot}d}{I}}. \tag{6.7}$$

This results in the sidebands shown in Fig. 6.2. The dependence of ω_ϕ on the magnitude of the driving electric field, E, is well-modeled by Eq. 6.7, as shown in Fig. 6.4. The equilibrium phase lag ϕ_{eq} may be neglected because $\tau\Omega \gg 1$ at the base presssure of the vacuum system. The fit shown in Fig. 6.4 extracts the ratio d/I, which can be used to determine the dipole moment, d, if the MS is assumed to be a uniform sphere with the radius, $r_{MS} = 2.35 \pm 0.02$ μm and mass $M_{MS} = 85 \pm 9$ pg, measured for this lot of MS in Ref. [41]. This procedure gives $I = (1.9 \pm 0.2) \times 10^{-25}$ kg·m^2, which implies $d = 127 \pm 14$ $e{\cdot}\mu$m, in agreement with Ref. [47].

The equilibrium phase lag ϕ_{eq} between **d** and **E** is expected to increase with the pressure P, as the drag from the gas increases. In the molecular flow regime, the damping coefficient, β, can be written as $\beta = k{\cdot}P$, where k is a constant that depends on the geometry of the MS, as well as the temperature and species of residual

gas [18, 19]. The argument to the arcsin in Eq. 6.6 can then be parameterized by

$$\frac{\omega_0 \beta}{d\,E} = \frac{\omega_0 k}{d\,E} \cdot P = \frac{P}{P_{\pi/2}}, \tag{6.8}$$

where $P_{\pi/2} \equiv d\,E/(\omega_0 k)$ is the pressure at which $\phi_{eq} \to -\pi/2$, where the MS rotation loses lock with the driving electric field (in practice fluctuations cause the MS to lose lock before ϕ_{eq} reaches $-\pi/2$).

This behavior is shown in the three top panels of Fig. 6.5 for three different amplitudes of the driving field. It is evident that the unlocking pressure depends on the field amplitude and that after losing lock ϕ_{eq} becomes random. $P_{\pi/2}$ can be extracted from a fit for each field amplitude, as plotted (with additional values of the field) in the bottom panel of Fig. 6.5. The linear relationship $k = d\,E/(\omega_0 P_{\pi/2})$ is evident, and a fit reports $k = (4.1 \pm 0.6) \times 10^{-25}$ m^{3}s, assuming $d = 127 \pm 14$ $e{\cdot}\mu$m. This is consistent with the value $k = 3.4 \times 10^{-25}$ m^{3}s predicted in Refs. [18, 19] for a 2.35-μm-radius MS in thermal equilibrium with 300 K N_2 gas.

When the electric field rotation axis and the angular momentum are not aligned, the dynamics are complex and depend sensitively on the initial conditions. For $\Omega \ll \omega_0$, and a field $\mathbf{E}(t) = E{\cdot}(\cos(\omega_0 t)\hat{\mathbf{z}} - \sin(\omega_0 t)\hat{\mathbf{y}})$, rotating about the $\hat{\mathbf{x}}$ axis, an approximate solution is given by,

$$\mathbf{L}(t) = L{\cdot}\left\{\cos\left[(\Omega/2)t\right]\hat{\mathbf{z}} + \sin\left[(\Omega/2)t\right]\hat{\mathbf{y}}\right\} \tag{6.9}$$

and,

$$\begin{aligned}\mathbf{d}(t) = -d{\cdot}\Big\{ & \cos\left[\omega_0(\Omega/2)t\right]\,\hat{\mathbf{x}} \\ & + \sin\left[(\omega_0 + \Omega/2)\,t\right]\cos\left[(\Omega/2)t\right]\,\hat{\mathbf{y}} \\ & + \sin\left(\Omega/2\right)\,\hat{\mathbf{z}}\Big\},\end{aligned} \tag{6.10}$$

in the absence of dissipation.

The angular momentum vector $\mathbf{L}$, undergoes left-handed precession about the electric field axis of rotation at an angular frequency $\Omega/2$. This behavior is observed

as a low-frequency modulation of the cross-polarized light most prominently at twice the precession frequency. The amplitude spectra for a precessing MS driven by a range of electric fields magnitudes are shown in Fig. 6.6, in which the MS is spinning at $\omega_0 = 2\pi\cdot(50\text{ kHz})$. As expected, the precession frequency is proportional to the magnitude of the driving electric field and the slope of Ω vs E is consistent with the measurement of (d/I) from the frequency of small oscillation.

6.4 Conclusions

We have demonstrated a technique capable of manipulating and measuring the rotational degrees of freedom of an optically levitated MS using electric fields and polarized light. Electrically driven rotation has several advantages over optical rotation. The driving torque and measurement of rotation use independent physical mechanisms allowing the MS to be rotated about an arbitrary axis, independent from the configuration of the trapping beam. The rotational frequency and phase of the MS can be fully controlled, expanding the range of possible measurements. For instance, the phase sensitive pressure measurement presented here makes it possible to measure the residual gas pressure in the immediate vicinity of the MS.

This technique has potential applications. For instance, the oscillation of the dipole in the rotating reference frame of the electric field is a low dissipation DOF that could be exploited for precision measurement and cooling. MSs made from materials with larger dipole moments, such as barium titanate, could be combined with larger electric fields in order to make oscillators with frequencies that can be tuned over many orders of magnitude with enhanced sensitivty to electric fields.

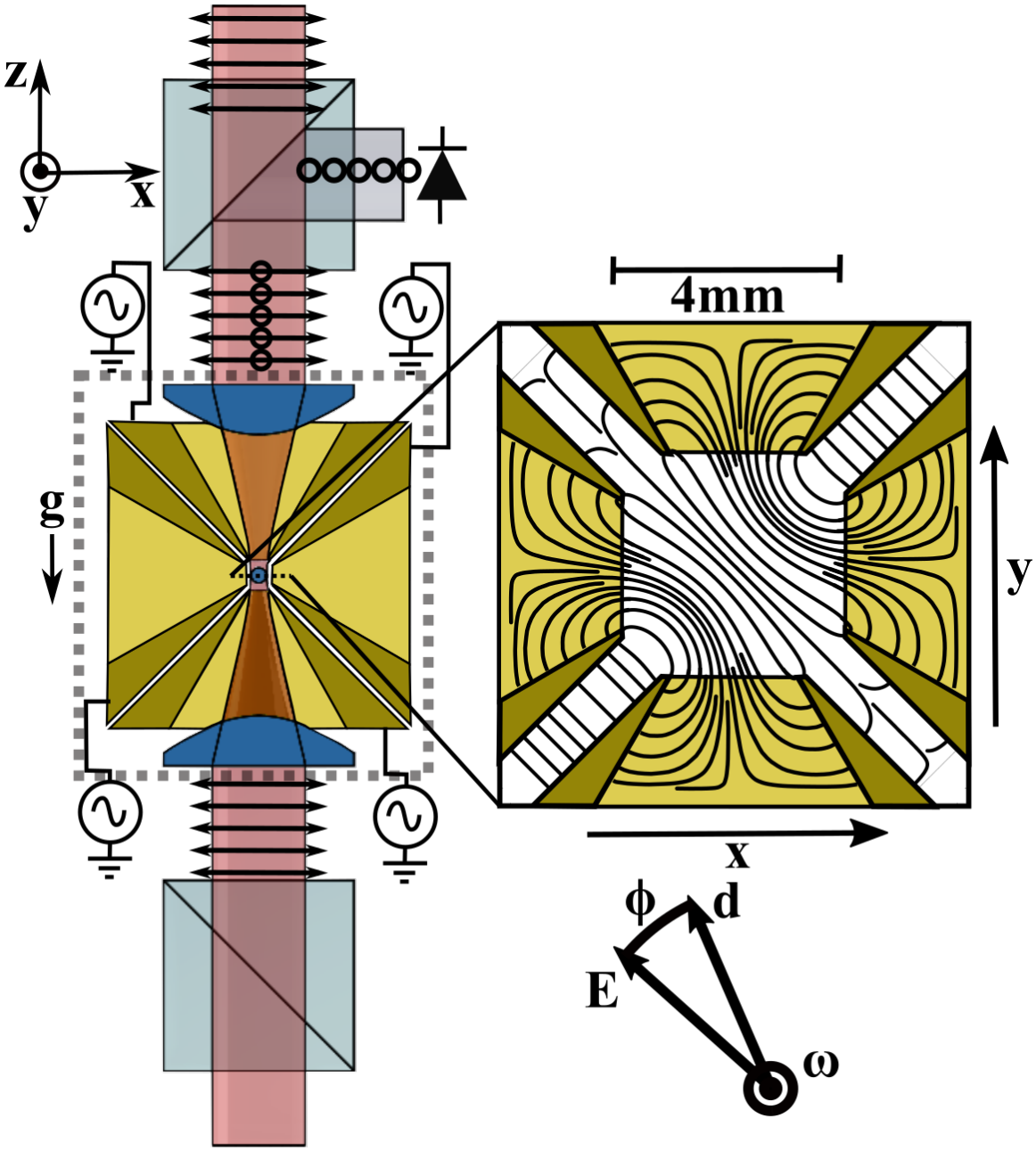

Figure 6.1: Cross-section of the electrodes and polarization optics. The MS is levitated by an optical system identical to that described in [17], with the addition of the polarization optics used to measure the rotational state of the MS. The dashed lines denote the components inside the vacuum chamber. The voltages on each of the six electrodes around the trapping region are driven to exert arbitrary torques on the MS's permanent dipole moment. The detail to the right shows a slice of the electric field streamlines produced by the electrode geometry with the electrodes on the top and the left at $+V$, while those on the bottom and on the right are at $-V$. The convention used to define ϕ is also illustrated to the bottom right.

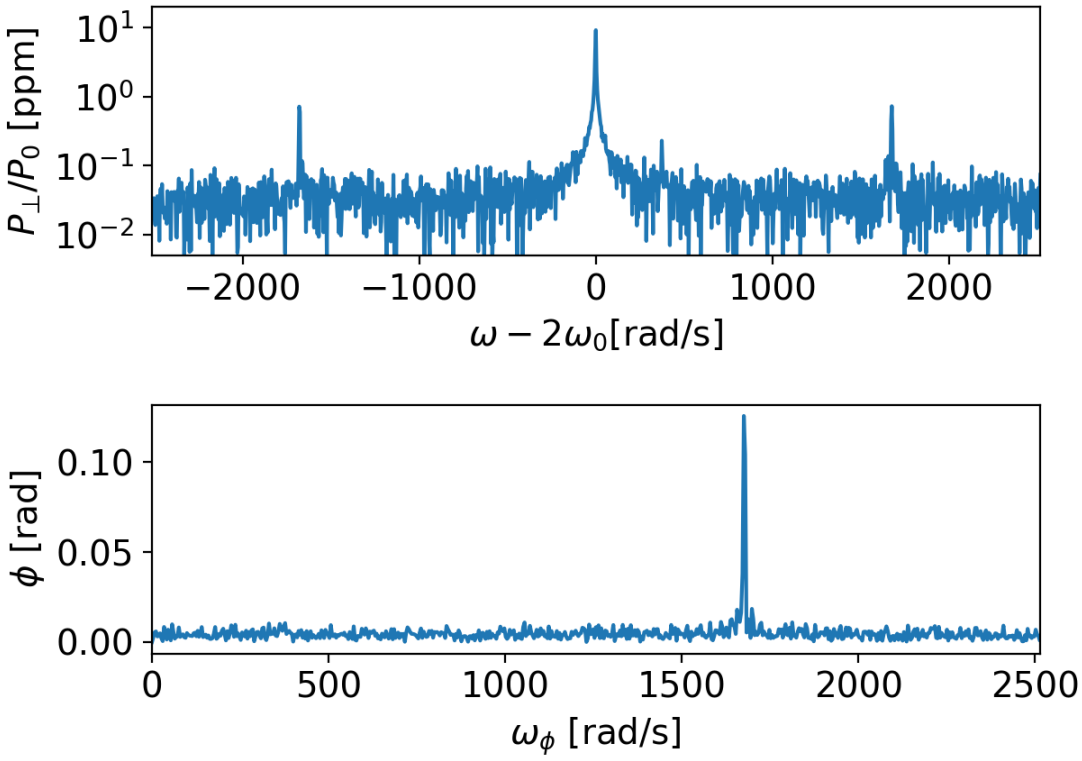

Figure 6.2: Top: typical amplitude spectrum of $P_\perp$ for a MS prepared in a state of angular momentum pointing along the $\hat{\mathbf{z}}$ direction. The MS is spinning with $\omega_0 = 2\pi\cdot(50\text{ kHz})$, driven by an electric field with $E = 27$ kV/m. The prominent line with sidebands are signatures of the MS rotation, with the position of the central line at twice the drive frequency. The sidebands are phase modulation of the rotation frequency, as shown in the bottom panel.

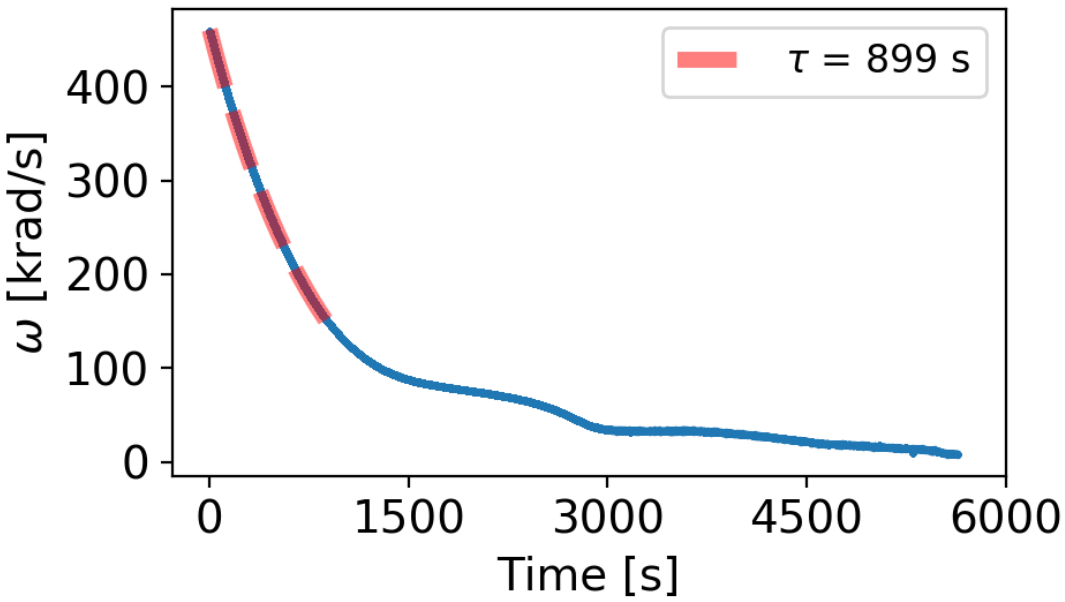

Figure 6.3: Time evolution of ω after the driving electric field is switched off. For $\omega \gtrsim 150$ krad/s the angular velocity exhibits an exponential decay. For $\omega \lesssim 150$ krad/s the dynamics are modified by torque that could be explained by a ~ 100 ppm degree of ellipticity in the 1 mW trapping beam and the $\eta \sim 10^{-2}$ phase retardation of the MS.

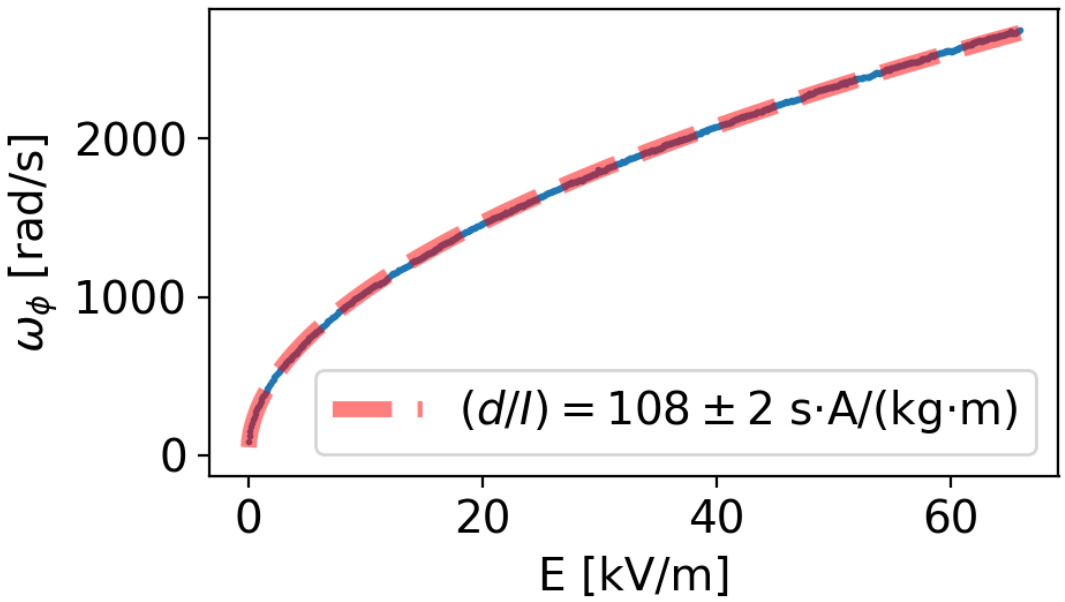

Figure 6.4: Harmonic oscillation frequency, ω_ϕ, versus driving electric field amplitude, E, for a MS spinning at $\omega_0 = 2\pi\cdot(50\text{ kHz})$ at a pressure of 2×10^{-6} mbar. The data is fit to Eq. 6.7, obtaining $(d/I) = 108 \pm 2$ s·A/(kg·m) and $d = 127 \pm 14$ $e\cdot\mu$m.

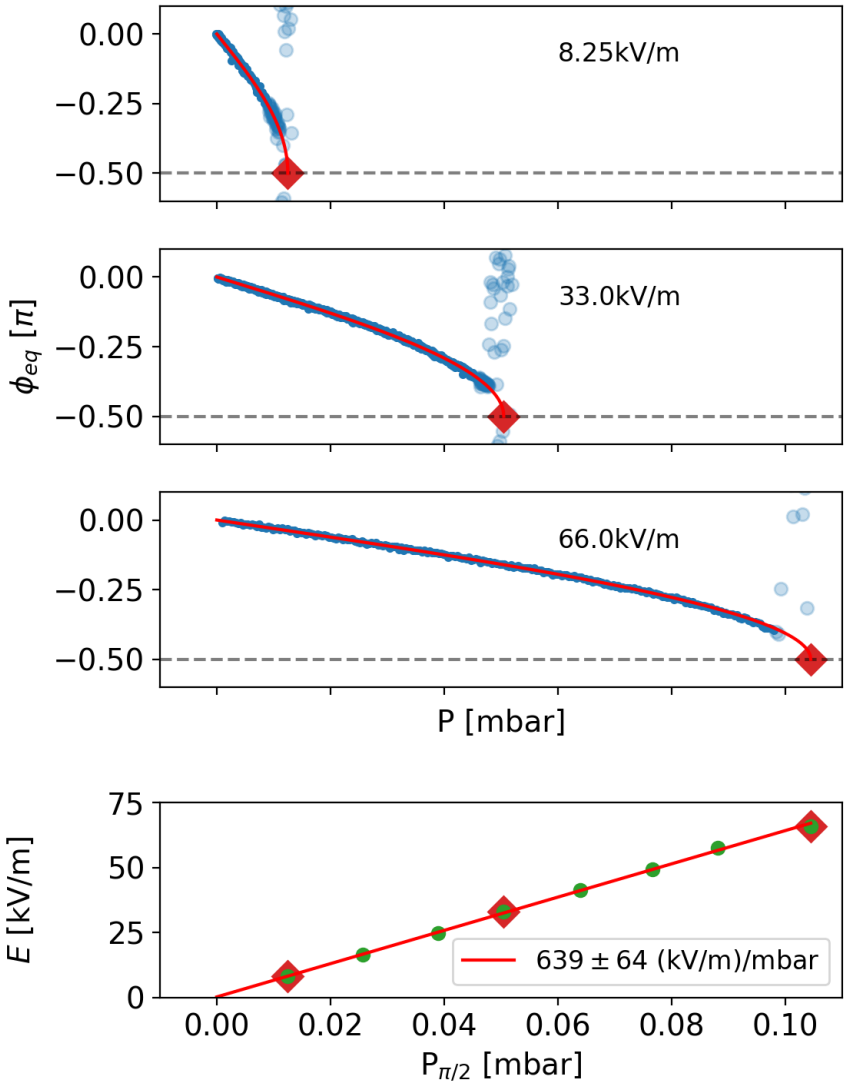

Figure 6.5: Top three panels: Equilibrium phase, ϕ_{eq}, versus chamber pressure for several magnitudes, E, of the driving field with $\omega_0 = 2\pi\cdot(50\text{ kHz})$. For each value of E, ϕ_{eq} increases until the MS loses lock with the field, and the phase becomes random. For each E, a fit to Eq. 6.6 (with the argument in Eq. 6.8) is shown in red. $P_{\pi/2}$ is identified by a red diamond. Bottom panel: The linear relationship between $P_{\pi/2}$ and E, with additional E included. The slope of the fit of E vs p_{max} is 639 ± 64 (kV/m)/mbar. Assuming the dipole moment measured from the frequency of small oscillations, this gives $k = \beta/P = (4.1 \pm 0.6) \times 10^{-25}$ m^{3}s, which is consistent with $k = \beta/P = 3.4 \times 10^{-25}$ m^{3}s predicted in Refs. [18, 19].

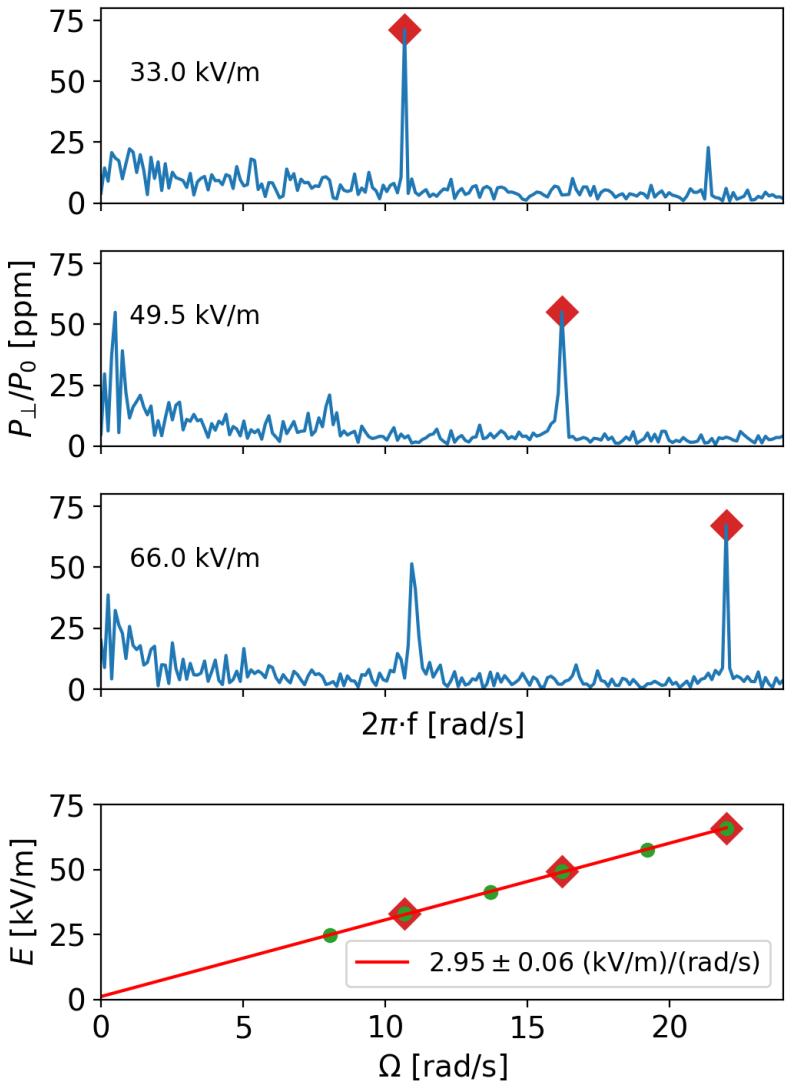

Figure 6.6: Top three panels: Spectra of the cross-polarized light intensity, $\mathcal{P}_\perp$, for a MS precessing about the $\hat{\mathbf{x}}$ axis while spinning at $\omega_0 = 2\pi\cdot(50\text{ kHz})$. The modulation of the cross-polarized light occurs predominantly at twice the precession frequency, denoted by red diamonds. Bottom panel: Ω for different E. The slope of the fit (red line) provides $(d/I) = \omega_0\Omega/E = 106 \pm 2$ s·A/kg·m, which is consistent with the measurement of d/I from the frequency of small oscillations.

Chapter 7

Precision mass and density measurement

7.1 Statement of the author's contribution

The following chapter closely follows what was published in [166]. This work is important because it developed a calibration independent technique for measuring the mass of a microsphere. The author contributed to the construction of the experiment, early development of the technique, and preparation of the manuscript.

7.2 Introduction

Optical trapping and manipulation of micron-sized dielectric particles in vacuum has been applied to optomechanics [1, 24, 115, 117, 133, 134] and cavity cooling [52, 116, 126], fundamental forces and interactions [46, 47, 114, 118, 119, 125, 143], quantum mechanics [120, 167] and quantum information [74], and surface science [166]. In many of these applications, knowing the size, mass and other characteristics of the trapped particles is critical to drawing conclusions about moments of inertia, optical spring constants, and force sensitivity.

We present a technique to measure the mass of individually trapped microspheres (MSs), by balancing a known electrostatic force, the optical levitation force, and

earth's gravity. The electrostatic force is extrapolated to the condition of no optical power to determine the gravitational force on the MS, and thus infer its mass. This measurement requires fewer assumptions than other techniques [168, 169] and is found to be independent of environmental conditions.

It may be possible to derive a direct relation between the optical power required to levitate a MS at the center of the trap and the mass of the MS using numerical methods to solve Mie scattering theory [170]. However, this requires a detailed understanding of the MS radius, non-sphericity, and index refraction, as well as a full description of the optical potential in three dimensions. The technique described here bypasses these complications and their associated systematics, resulting in improved accuracy.

A subset of MSs are also individually collected from the optical trap using a mechanical probe, and imaged via scanning electron microscopy (SEM) to determine their radii. Knowing both the mass and radius of individual MSs, their density can be calculated. The radii determined from SEM images of those specific MSs are compared to the radii determined from SEM images of large populations of $\sim 10^3$ MSs that have never been in the optical trap.

7.3 Experimental Setup

The optical trap used here is described in Refs. [17, 166]. Silica MSs obtained from the Stöber process [128, 159] with $\sim$4.7-μm-diameter are loaded into the trap by ejection from a vibrating glass slide placed above it. To efficiently load MSs, 1 mbar of residual gas is used to provide viscous damping. The chamber can then be evacuated to a final pressure of 10^{-6} mbar, in order to reduce thermal noise. Below 0.1 mbar, the trap requires active feedback for stabilization. The feedback system [17] serves to provide viscous damping in all three degrees of freedom (DOF). Importantly, the axial degree of freedom of the MS, stabilized by modulating the power of the trapping beam with an acousto-optic modulator, is held at a fixed position by proportional and integral feedback terms.

The above loading procedure triboelectrically charges the MSs. A xenon flash-lamp, emitting ultraviolet light, is used to alter the MS charge state, q_{MS}, over a wide range $-500e < q_{\mathrm{MS}} < 500e$, where e is the elementary charge [17, 46, 47, 166]. The arbitrarily set MS charge state, stable over timescales of order one month, is known with sub-e precision, as individual quanta are added to or removed from a state of overall neutrality.

Charged MSs are shielded from external electric fields by a Faraday cage made of six electrodes, each with an independent bias voltage. The two electrodes directly above and below the trapped MS are used to generate a uniform, slowly-varying electric field at the trap location, exerting an axial force on a charged MS. The relation between the applied voltage and the electric field within the trapping region is modeled with finite-element analysis, with an uncertainty that is much smaller than any other systematics.

After measuring their mass, three MSs are collected onto the end of a polymer-coated silicon beam, described in Refs. [136, 166], where they remain attached via Van der Waals forces. Individual MSs are addressed to particular locations, recognizable from features on the silicon beam. The silicon beam is removed from the chamber and the three MSs are imaged with SEM, in order to determine their individual radii. A population of MSs of the same variety and lot as those used in the trap are also measured with SEM. For this purpose, a monolayer of MSs is spread onto a silicon wafer, and subsequently imaged with SEM. Various diffraction gratings [20] are used to calibrate the instrument at each of the magnifications.

7.4 Measurements and Results

Once a constant, known charge is obtained for a trapped MS, its axial position is fixed near the focus of the optical trap using the feedback. The slowly-varying (0.5 Hz) electric field is applied in the vertical direction, while the power of the trapping beam injected into the chamber, controlled by the feedback, is monitored with a beam pick-off and a photodiode. As the applied electrostatic force increases, the axial feedback

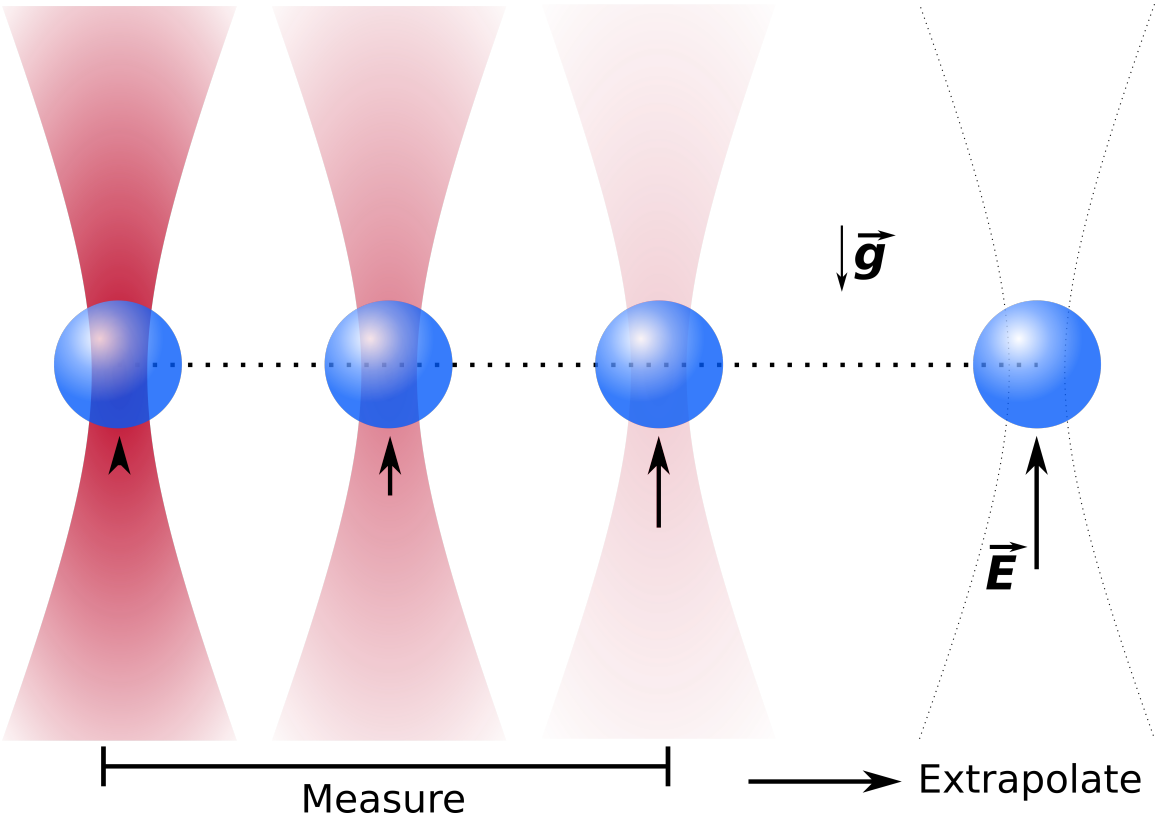

Figure 7.1: Schematic depiction of the measurement technique. A charged MS is trapped by a Gaussian laser beam and held at fixed axial position with active feedback. A slowly varying electric field is applied, depicted with a black arrow. The active feedback reduces the optical power, indicated by the intensity of the trapping beam, such that the sum of the optical and electrostatic levitation forces opposing gravity is constant. The relation between optical power and applied field is then extrapolated to zero optical power, allowing a determination of mass from the implied electrostatic levitation field and the known charge.

reduces the optical power required to maintain a net force of zero, counteracting gravity. The electric field can then be extrapolated to zero optical power, which allows a determination of the MS mass. This process is shown schematically in Fig. 7.1. The case of zero optical power cannot be directly measured, as there is a minimum power necessary both to constrain the MS to the optical axis, and to generate sufficient back-reflected light to measure the axial position via the methods described

in Refs. [17, 166]. We note that the technique described is only applicable to single-beam traps [17], as its extension to systems with more than one beam requires care to account for the contributions of auxiliary beams to the total optical levitation force.

The equilibrium of axial forces F_z is expressed as,

$$\sum F_z = qE(t) - mg + F_{\mathrm{opt},z}(t) = 0, \tag{7.1}$$

where q and m are the charge and mass of the MS, respectively, $g = 9.806\ \mathrm{m/s^2}$ is the local gravitational field strength [171], $F_{\mathrm{opt},z}(t)$ is the optical levitation force, assumed to be proportional to the trapping beam power, and $E(t)$ is the applied electric field strength. For each MS and charge state combination, the slowly-varying electric field and power are measured at least 50 times, each with a 50 s integration. An exemplary dataset is shown in Fig. 7.2, with the calculated mass from the extrapolation to zero optical power.

The technique described avoids a number of systematic uncertainties inherent to derivations of the MS mass from optical properties and the trapping potential [170]. Importantly, the extrapolation to zero trapping beam power is only sensitive to an offset in the power measurement, so an exact calibration of power is also unnecessary. The only requirement for the measurement is that the photodiode responds linearly to the incident optical power, which is easily achieved with a device operating well below saturation. Indeed, for the measurements reported here, the optical power is normalized to an arbitrary value of one, as seen in Fig. 7.2.

The mass measurement is performed on 13 MSs, in various charge states around $|q| = 20e$, with both signs of charge, as well as in two vacuum pressure regimes: trapping pressure, $\sim$1 mbar, and chamber base pressure, $\leq 10^{-6}$ mbar. The use of different pressures tests whether MS mass is lost due to heating, as observed for larger MSs in Ref [42]. Cooling via residual gas decreases significantly with decreasing pressure, while absorption and scattering of laser light, the dominant heating mechanisms, remain constant.

Results of mass measurements for all experimental conditions are shown in Fig. 7.3,

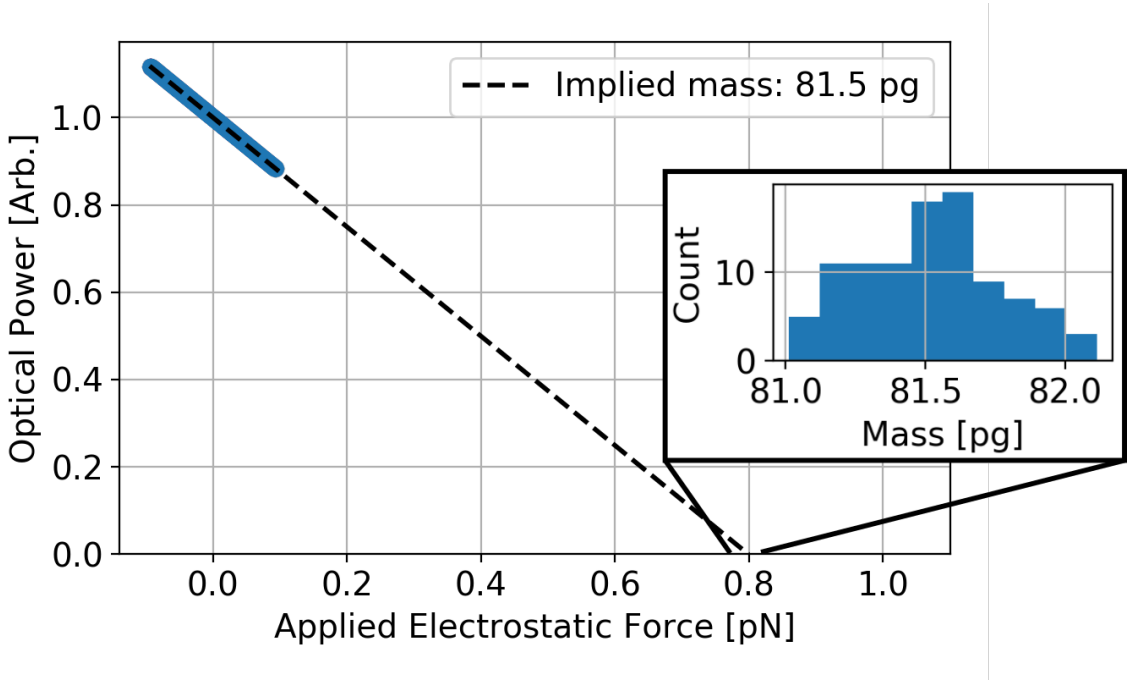

Figure 7.2: Normalized optical power vs applied electric field for 100×50 s integrations with a single MS. The extrapolation is performed separately for each integration. The mean of all extrapolations is shown with a dashed black line. (Inset) distribution of the 100 extrapolated masses.

while the results from the final three MSs later transferred to SEM are provided in the first column of Table 7.1. Fluctuations in the mass measurement over the ≥ 50 distinct

Table 7.1: MS masses, m, averaged over all experimental conditions; radii, r, averaged from two distinct high magnifications; and the derived density, ρ, for the three MSs caught on the silicon beam. All measurements include statistical and systematic uncertainties, and the relative contributions have been shown explicitly for the measured masses.

MS	m [pg]	r [μm]	ρ [g/cm^3]
#1	$84.0 \pm 0.8\,(\text{stat}) \pm 1.5\,(\text{sys})$	2.348 ± 0.038	1.550 ± 0.080
#2	$83.9 \pm 1.1\,(\text{stat}) \pm 1.5\,(\text{sys})$	2.345 ± 0.037	1.554 ± 0.079
#3	$85.5 \pm 0.2\,(\text{stat}) \pm 1.5\,(\text{sys})$	2.355 ± 0.038	1.562 ± 0.081

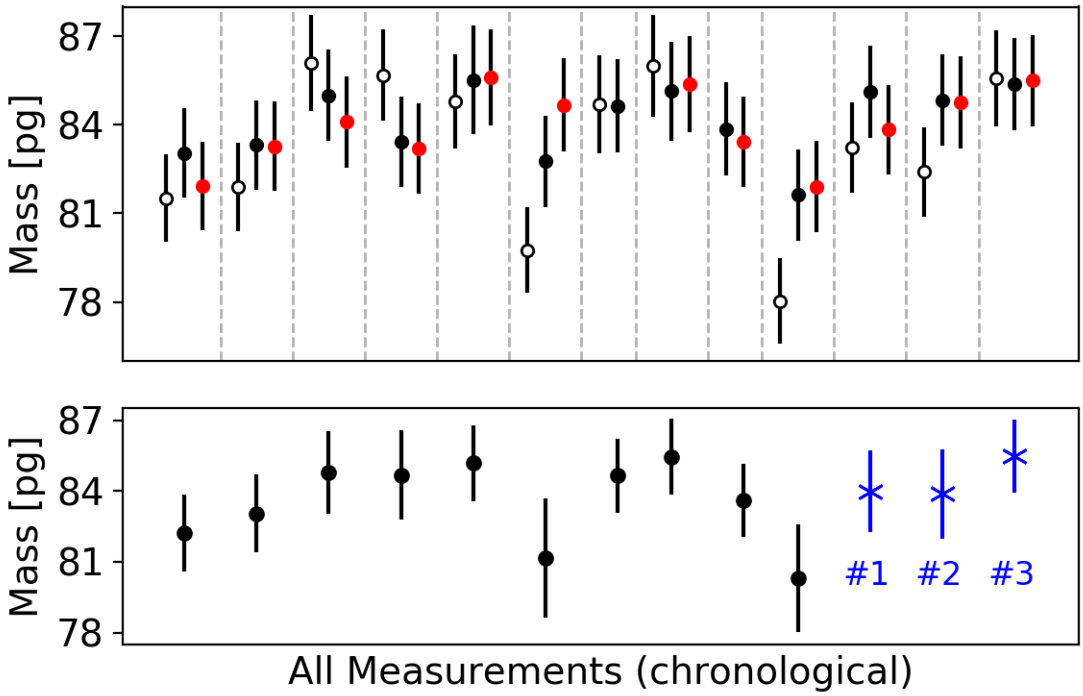

Figure 7.3: (top) Measured MS masses in chronological order. Unfilled markers indicate a low-vacuum environment, $P = 1.5$ mbar, while filled markers indicate high-vacuum environment, $P = 10^{-5} - 10^{-6}$ mbar. Black markers are measurements with a negatively charged MS, while red markers are measurements with a positively charged MS. Different MSs are separated by vertical dashed lines. (bottom) Mean mass for each MS, weighted over all experimental conditions. The blue data points with cross-shaped markers indicate the three MSs imaged with SEM following their mass measurement.

50 s integrations for a set of experimental conditions are normally distributed with a standard deviation on the order of 0.5 pg as seen in the inset of Fig. 7.2. However, the total uncertainty of the measurement is dominated by common systematics which are enumerated in Table 7.2.

Each effect listed has been interpreted as an uncertainty on either the applied electric field, the measured optical power, or the assumed value of g. From Eq. 7.1, these relative uncertainties directly propagate onto the extrapolated mass, whose uncertainty is computed as a quadrature sum of all contributions. The accuracy

Table 7.2: Systematic effects on the mass measurement. The amplifier discussed produces the voltage driving the electrodes, and thus the electric field. Geometric misalignment, including optical tolerances, can change the value of the electric field at the location of the trap. The application and subsequent measurement of the electric field is also subject to systematics, and each measurement channel can experience electrical pickup. Effects were determined empirically where possible, or were obtained from instrument specifications.

Effect	Uncertainty [$\times 10^{-3}$]
Amplifier monitor accuracy†	$\boldsymbol{\sigma_E/E \sim 15}$
Lens focal length†	$\boldsymbol{\sigma_E/E \sim 10}$
Amplifier gain error†	$\sigma_E/E \sim 2$
Tilt of field-axis	$\sigma_E/E \sim 2$
Tilt of trap (optical)	$\sigma_E/E \sim 1$
ADC offsets†	$\sigma_{\mathcal{P}}/\mathcal{P} \sim 1$
Electrode voltage offset	$\sigma_E/E \sim 0.5$
DC power offsets	$\sigma_{\mathcal{P}}/\mathcal{P} \sim 0.3$
Local g ‡	$\sigma_g/g \sim 0.1$
Electrical pickup	$\sigma_{\mathcal{P}}/\mathcal{P} \sim 0.02$

† From manufacturer datasheets,
‡ Estimated from EGM2008 [171].

of the high-voltage amplifier's output monitor and the tolerance on the trapping lens focal length dominate the overall uncertainty. The second effect may offset the trap axially, thus sampling a different electric field strength. Each of the effects in Table 7.2 should result in a systematic shift common to all mass measurements. The total uncertainty obtained is 1.8%, which is included as a systematic on the mean mass for each MS.

We also observe scatter in the measured mass of a single MS between different experimental conditions, as seen in Fig. 7.3. These variations could be due to a number of effects including optical path length fluctuations in the axial feedback, electronic fluctuations in the axial feedback, as well as real changes in the mass of a MS. We do not observe any correlations between measured mass and experimental

parameters such as the MS charge state or the vacuum pressure. The fluctuations are quantified by the standard deviation of measurements with different experimental conditions, which is included as part of the statistical uncertainty on the measured mass.

To collect the final three MSs, the polymer-coated silicon beam is rapidly inserted between the trapping laser and the MS, allowing the MS to fall under the influence of gravity. Each distinct MS can be associated to the respective mass measurement given its position relative to the internal structure of the silicon beam. Van der Waals forces, enhanced by the polymer, serve to keep the MSs attached, whereas doped silicon and gold were both found to produce insufficient adhesion during previous attempts. The fluorocarbon polymer coating is made with a plasma deposition technique inherent to the Bosch process [172], using C_4F_8 and SF_6 gases in a 1.5 kW inductively-coupled plasma.

For the SEM measurements, the silicon beam with three MSs is first sputter-coated with 100 ± 50 nm of a Au/Pd alloy, in order to prevent charging and the resulting MS ejection from the silicon beam. Charging effects from the SEM are significantly exacerbated by the non-conductive polymer, necessitating the relatively thick coating. A diffraction grating with 1.000 ± 0.005 μm pitch [20] is used to calibrate SEM images of individual MSs at high magnification, as seen in Fig. 7.4.

The MS diameter is first determined in terms of raw pixels. This is done via edge detection and contour tracing to outline the MSs. The contour is then fit with an ellipse to account for real ellipticity in the MSs, as well as astigmatism in the electron microscope. The radius is taken as the average of the semi-major and semi-minor axes, which differ by less than a percent. A systematic uncertainty of ± 1 pixel in the determination of the semi-major and semi-minor axes is included.

At the same level of magnification, images of the calibration grating are used to convert from pixels to physical distances. This is done by locating the centroids of the grating's repeated structure in the image, and averaging the pixel distance between neighboring centroids across the entire image. The ratio of grating pitch in microns to observed grating pitch in pixels serves to calibrate the images. The 100 ± 50 nm conductive coating was subtracted from the final radius.

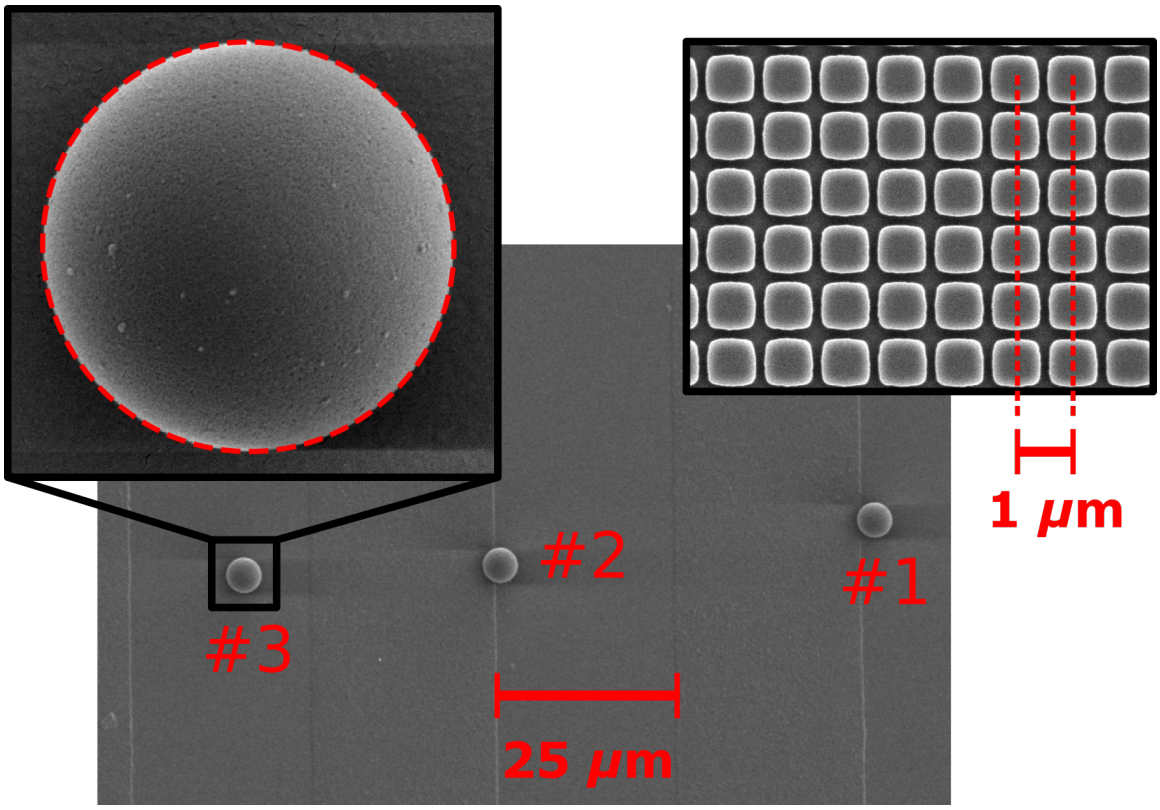

Figure 7.4: SEM images the of three MSs collected onto the silicon-beam, at 2500× magnification. (Left inset) one MS at 35000× magnification, overlaid with the best-fit ellipse, and (right inset) the 1.000 ± 0.005 μm diffraction grating [20], also seen at 35000× magnification. The diffraction grating serves as a calibration length scale for the high magnification images of individual MSs.

The measured masses and radii of the three imaged MSs are shown in Table 7.1, together with the calculated individual density. This is consistent among the three MSs and its average value, $\rho_{\mathrm{MS}} = 1.55 \pm 0.08$ g/cm^3, is significantly smaller than that of amorphous fused silica, $\rho_{\mathrm{SiO_2}} \approx 2.2$ g/cm^3 [173], as well as the value provided by the manufacturer, $\rho_{\mathrm{Bangs}} \approx 2.0$ g/cm^3 [128]. Spin-echo small-angle neutron scattering measurements on particles synthesized via the Stöber have found an open pore volume fraction of 32% and an inaccessible pore volume fraction of 10% for particles with radius ∼80 nm [174]. It is distinctly possible that MSs in solution absorb a nontrivial amount of water or other solvent, and that under low- to high-vacuum conditions, the

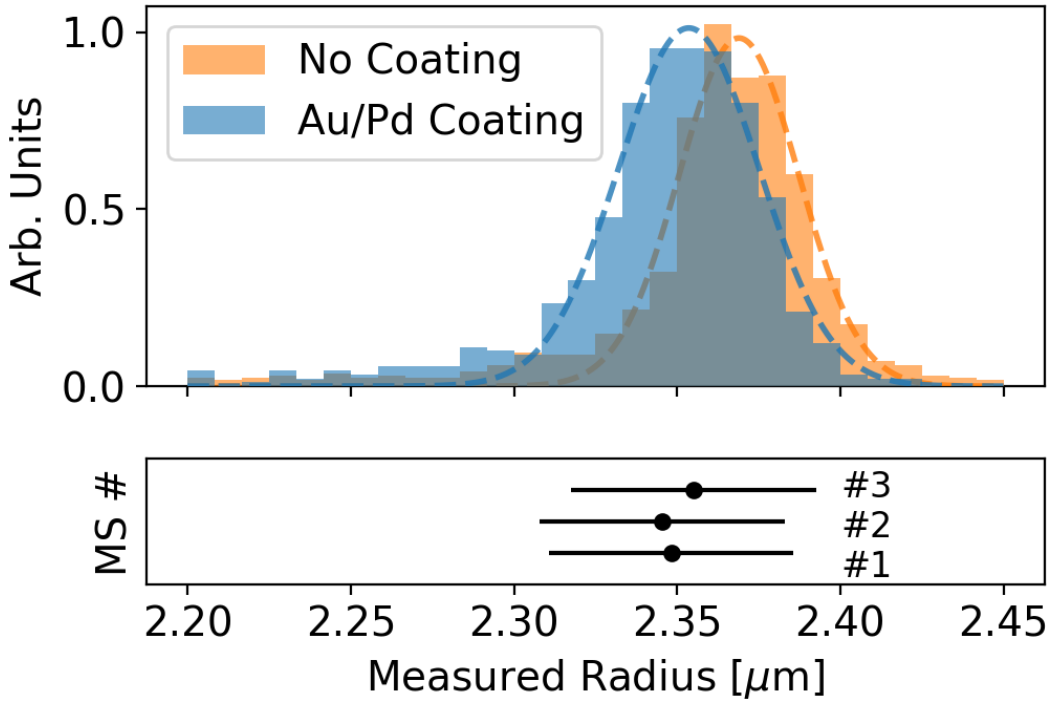

Figure 7.5: (top) Distributions of MS radii measured via SEM, for both conductively coated and uncoated MSs. Gaussian fits yield central values of $r_{\mathrm{Au/Pd}} = 2.35$ μm and $r_{\mathrm{NC}} = 2.37$ μm for the conductively coated and uncoated MSs, respectively. Each distribution is generated from approximately 10^3 distinct MSs. (bottom) Individual radius measurements from analysis of the MSs seen in Fig. 7.4.

liquid is removed, effectively lowering the mass and density. The classical electron oscillator model [175] implies that the reduced density should result in a reduced refractive index: $n_{\mathrm{MS}}^2 - 1 = (n_{\mathrm{SiO_2}}^2 - 1)(\rho_{\mathrm{MS}}/\rho_{\mathrm{SiO_2}})$, leading to $n_{\mathrm{MS}} \approx 1.33$, at 1064 nm, where $n_{\mathrm{SiO_2}}$ is the index of fused silica [176].

To characterize the distribution of radii via SEM, a monolayer of MSs is prepared on two heavily-doped silicon wafers. Charging effects are reduced without the polymer so a conductive coating is not explicitly necessary. However, the two wafers are imaged with and without a conductive coating to study possible systematics. The coated wafer is sputtered with 40 ± 10 nm of the same Au/Pd alloy mentioned previously.

Each wafer includes a diffraction grating with 9.98 ± 0.02 μm pitch [20] to serve as a length calibration. Images of $\sim 10^3$ distinct MSs, both conductively coated and not, are collected at a range of magnifications, together with images of the calibration grating. The same ellipse identification and calibration are used to characterize MS populations.

The radii of the final three MSs measured are compared to the distribution of radii from the MS population measurements, shown in Fig. 7.5. The conductive coating reduces the apparent size of the MSs by $\sim$20 nm, after accounting for the correction due to coating thickness. This may be the result of charging of the uncoated MSs.

After correcting for the thickness of the coating, the individually measured radii of conductively coated MSs are found to be consistent with the distribution of radii measured from the large population of conductively coated MSs. The apparent independence of the measured mass on the vacuum pressure, as well as the consistency between the measured radii of individual MSs that have been optically trapped and large populations of MSs that were never trapped, both indicate a negligible loss of MS material by heating, under the environmental conditions tested for $r \approx 2.35$ μm silica MSs. The simplicity and accuracy of the mass measurement, along with the reliable transfer of specific microspheres from the optical trap to air and subsequently to a different vacuum environment, opens the possibility for other correlated, precision measurements on microscopic objects.

Chapter 8

Conclusion

Tests of gravity at micron length-scales with optically levitated microspheres have to overcome various challenges in order to compete with the sensitivity of measurements like those in Refs. [32, 37, 40]. The sensitivity has to be increased by about four orders of magnitude to probe unexplored parameter space for Yukawa deviations from Newtonian gravity. The work conducted within this thesis provided the first steps towards understanding and overcoming these challenges, which consist mainly of background forces. Techniques that may help achieve this sensitivity are presented in this chapter as well as other potential improvements for future work.

8.1 Technique For Testing Gravity

Due to the relative weakness of gravitational interactions, techniques for testing gravity must suppress sources of noise as well as background forces. In this context, noise is a disturbance added to a signal that can be reduced by averaging over a longer measurement period, while backgrounds are extraneous signals that do not average to zero. Both noise and backgrounds have a component that resembles the experimental signature of gravity, so their presence ultimately limits the sensitivity of a measurement.

We developed a technique for testing gravity with optically levitated microspheres that attempted to mitigate sources of noise and backgrounds. The concept is depicted

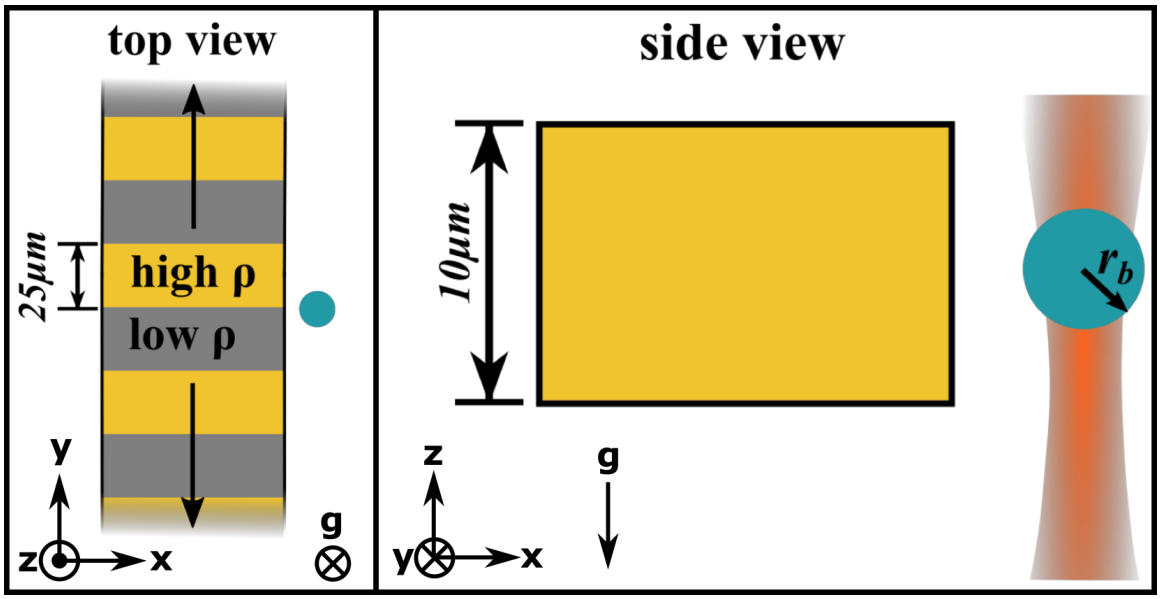

Figure 8.1: Left: Top down view of the protocol we developed for testing gravity. A mass structure with density modulation, or attractor, is driven past a microsphere producing an oscillating gravitational field. Right: A profile view of the attractor and the microsphere showing that a high aspect-ratio structure can be brought to the surface of a levitated microsphere.

schematically in Figure 8.1. A microsphere is suspended at the focus of a Gaussian laser beam where an attractor mass with density modulation is brought in close proximity to the microsphere. If the attractor mass is driven along the direction of density modulation it produces an oscillating gravitational field.

This technique has several potential advantages. Backgrounds form mechanical vibration should occur primarily at the frequency of mechanical motion, so the density modulated attractor shifts gravitational signals to higher harmonics of the driving motion. Shifting the gravitational signal to higher frequencies also increases the signal to noise ratio by moving the signal above many sources of low frequency noise. This technique also maintains a constant separation between the attractor and the microsphere, which should minimize variation in the electric field produced by a voltage on the attractor. A shielding layer can be evaporated onto the surface of the density modulation to screen underlying electronic variation between the high and

low-density regions of the attractor.

8.1.1 Attractor Fabrication

To implement this technique, attractor microstructures were fabricated with density contrast formed by silicon ($\rho = 2.2$ g/cm^3) and gold ($\rho = 19.3$ g/cm^3). An example of one of the attractors is shown in Figure 8.2. The process for fabricating the attractor structure starts with a silicon-oxide-insulator (SOI) wafer. A SOI wafer has three layers. The bottom handle layer is a ~ 500 μm silicon layer which is separated from the ~ 10 μm silicon device layer by a ~ 1 μm oxide layer. The gold structures in the attractor are formed by plasma etching trenches in the device layer. A conductive gold seed layer is then evaporated on the bottom of the trenches and used to complete the circuit for electroforming gold into the trenches using a sulfite based plating solution. After electroforming gold, the shape of the attractor is defined by plasma etching the device layer. The devices are then released from the SOI wafer by plasma etching through the handle layer. The final step of the process is evaporating a gold film on the entire structure to shield the electrostatic differences between the underlying gold and silicon. The fabrication process is given in detail in appendix A.

8.2 Backgrounds

This measurement technique suffered from the presence of background forces limiting its sensitivity. When the attractor was placed with a surface to surface separation of 20 μm to the microsphere and driven along the axis of density modulation, a $\sim 10^{-15}$ N force was observed. This performance needs to be improved by five orders of magnitude in order to achieve sensitivity comparable to other experimental approaches. A plot of the measured force in the x, y, and z directions is shown in Figure 8.3. This background was attributed to electric fields due to 'patch potentials' interacting with the microsphere's permanent dipole moment because it was modulated by changing the overall bias of the attractor structure.

'Patch potentials' are variation in the surface potential of a conductor caused by

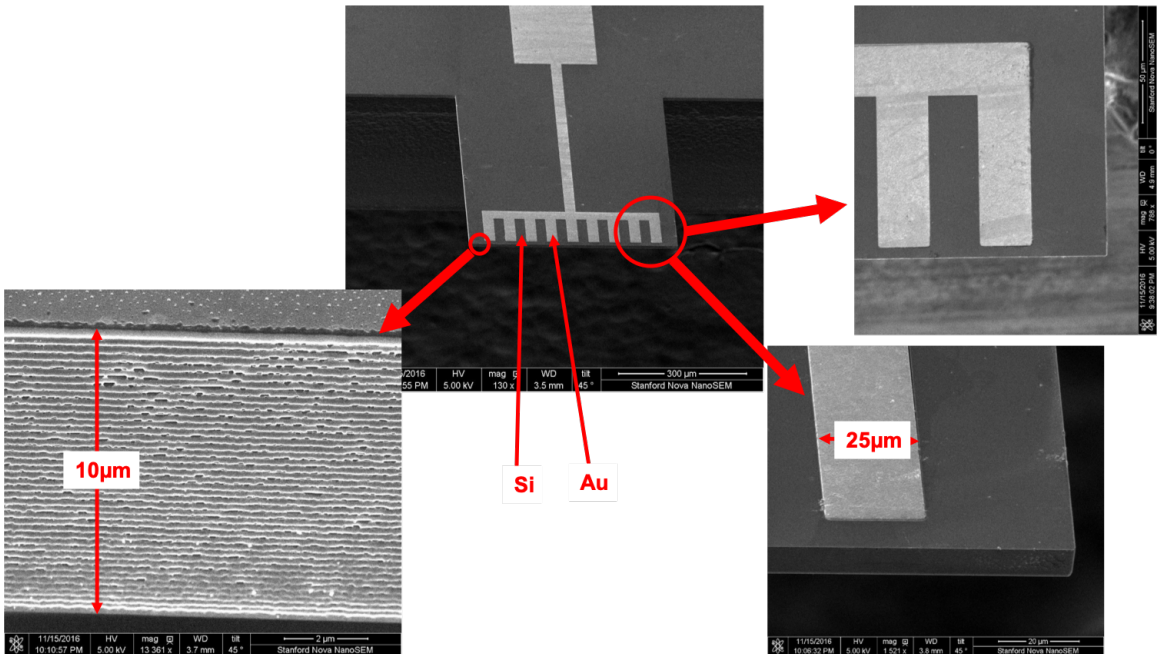

Figure 8.2: Scanning electron microscope (SEM) images of an attractor for gravitational measurements. The density modulation is formed by the density contrast between gold and silicon. These devices were fabricated at the Stanford Nano Fabrication Facility (SNF) by etching trenches into the device layer of a silicon-Oxide-Insulator (SOI) wafer, electroforming gold into the trenches, and then releasing the attractor by etching through the back of the SOI wafer.

differences in the chemical potential for conduction electrons. The background force from patch potentials can be estimated as follows. A patch primarily interacts as a dipole, with an electric field that scales like $E \sim Vl^2/r^3$, where V is the voltage scale of the patch, l is the length scale of the patch, and r is the separation. Since the electric fields from patches fall of like $1/r^3$, a point in space only feels the electric field from patches in an area $\sim r^2$ on the surface. All of the $N = r^2/l^2$ microscopic patches in this region form an average patch with $V_{ave} \sim V/\sqrt{N} = Vl/r$, and length scale r, which produces an electric field $E \sim Vl/r^2$. Both the Vl scaling and the approximate $1/r^2$ scaling are verified in Ref. [45]. The gradient of the electric field from patches produces a force on the microsphere's permanent dipole moment, d, that scales like $\sim dVl/r^3$. For the $d = 100$ $e\mu$m dipole moments measured in Refs. [47, 54], and the

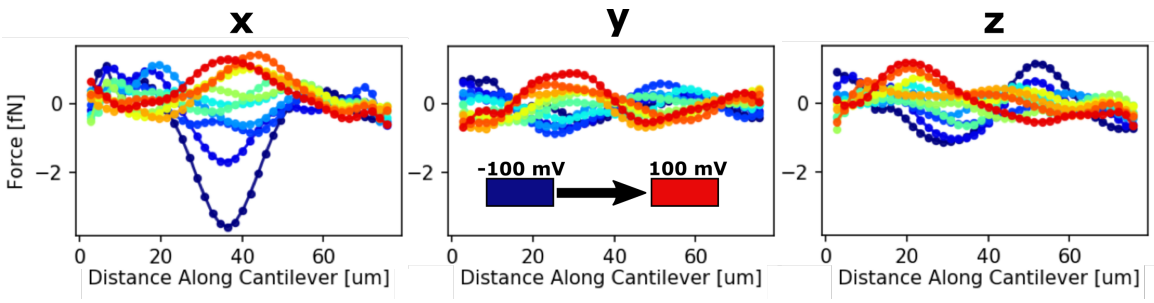

Figure 8.3: The force on a microsphere as the attractor is displaced along the axis of density modulation. The microsphere was aligned with the attractor as shown in Figure 8.1 with a face to face separation of 20 μm. We observed a ∼fN force which is at least five orders of magnitude greater than the force due to a Yukawa deviation from Newtonian gravity at the sensitivity reported by other experiments.

$Vl \sim 100$ μm mV patches measured in Ref. [45] this produces a $\sim 10^{-16}$ N force at 20 μm separation, in rough agreement with the observed background.

Sensitivity was determined by fitting the measured force versus attractor displacement in either the frequency, time or spatial domains to a template created by numerical integration of a Yukawa potential over the attractor geometry at each λ. The analytic integral of a Yukawa interaction over a sphere shown in appendix B was needed to improve the computational efficiency of this process. An example of a Yukawa force template is shown in Figure 8.5, while an example fit is shown in Figure 8.6. No analysis technique was found to have a significantly different performance. A comparison of the sensitivity implied from the size of this background is shown in Figure 8.4.

8.3 Electrostatic Shield

A stationary electrostatic shield was implemented to screen electrostatic forces. The shield consisted of a $500 \times 100 \times 1$ μm tip-less AFM cantilever positioned between the end of the attractor and the microsphere as shown in Figure 8.7, and Figure 8.8. Although the gold film on the shield had similar patch potentials to the attractor, it

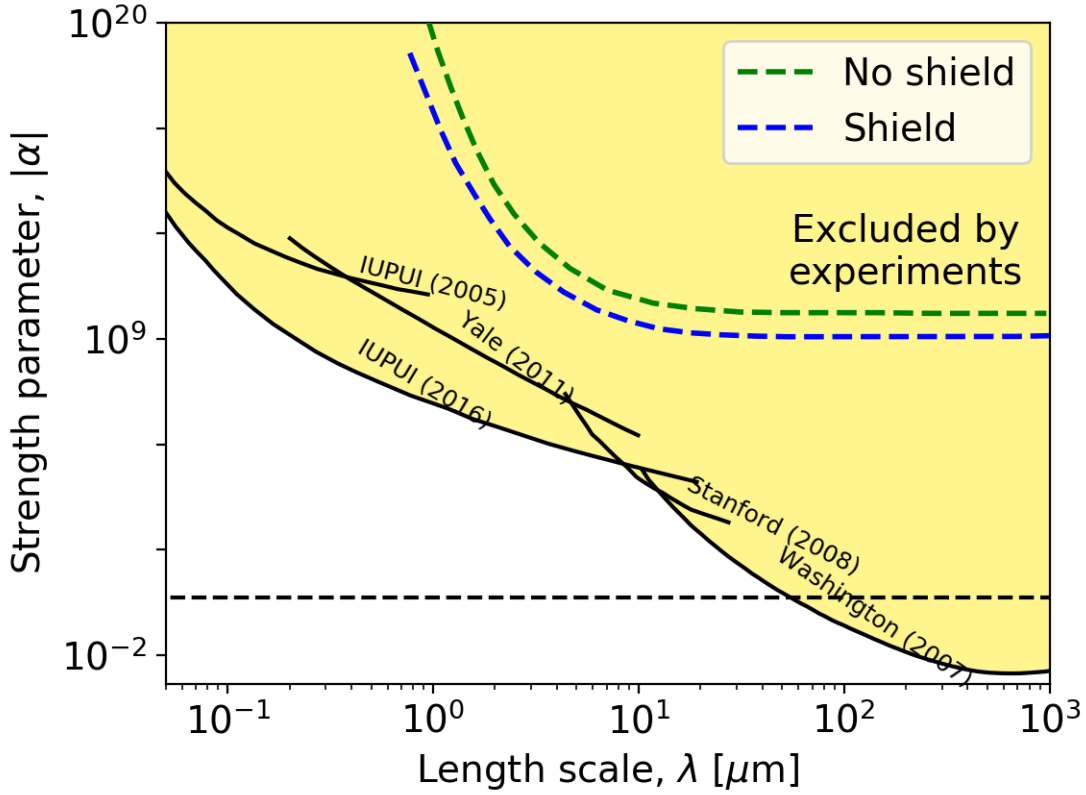

Figure 8.4: A comparison between the reported 95% confidence level sensitivity to interactions of the form $V(r) = Gm_1m_2(1 + \alpha e^{-r/\lambda})/r^2$ between other experiments and the test with optically levitated microspheres discussed here. The sensitivity with and without a stationary shield is shown. The technique discussed here needs to be improved by about four orders of magnitude to reach competitive sensitivity.

remained stationary during measurements so it was not expected to produce a background force modulated like a gravitational signal from the attractor. It was possible to position the shield in between a microsphere and attractor with the microsphere separated from the attractor less than 20 μm. The rudimentary position measurement did not allow measurement of the position of the shield more accurately at the time. The background force with the shield was a factor of ~ 10 smaller than the background without a shield. The sensitivity determined by analyzing the data taken

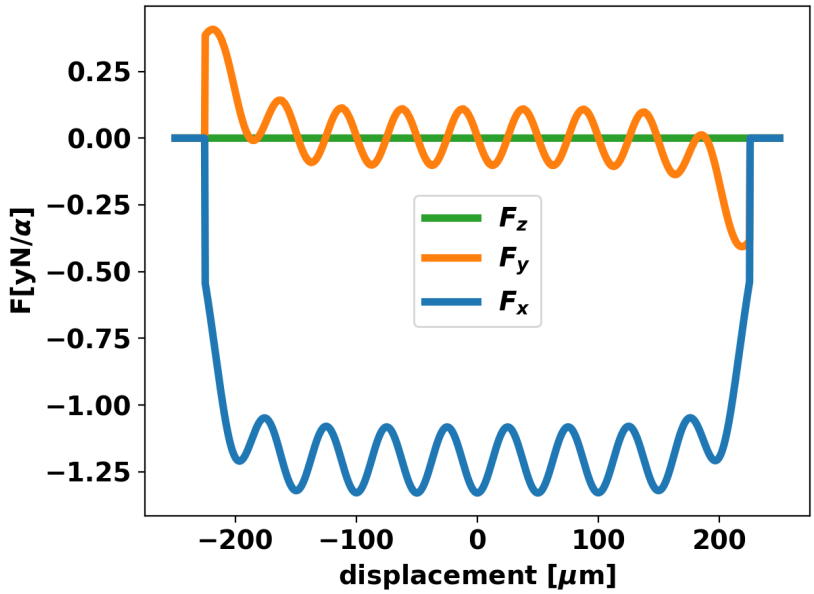

Figure 8.5: The 3-d force on a 2.5 μm radius silica microsphere as a function of displacement along the density modulation of the attractor for $\lambda = 25$ μm with a 15 μm face to face separation from the attractor. There is no force in the z-direction because the microsphere is centered on the attractor. Sensitivity was determined by fitting to this curve in the time, space, or frequency domains with different empirical background models. A different template was created for each value of λ that was tested. No analysis technique was found to produce a significantly different sensitivity.

with a shield is compared to the sensitivity without a shield, as well as to the sensitivity of other measurements in Figure 8.4. While the sensitivity of optically levitated microspheres was improved by about an order of magnitude, a further improvement of about four orders of magnitude is still necessary to probe new parameter space.

The behavior of the shielded $\sim 10^{-16}N$ background was found to be qualitatively different from the unshielded background. The shielded background was not modulated by the bias of the attractor, and was comparable in size with and without a microsphere in the trap, as shown in Figure 8.9. Electrical interference was ruled out as the cause by the observation that the background was not observed with the laser beam blocked. The best explanation for the background was scattered light

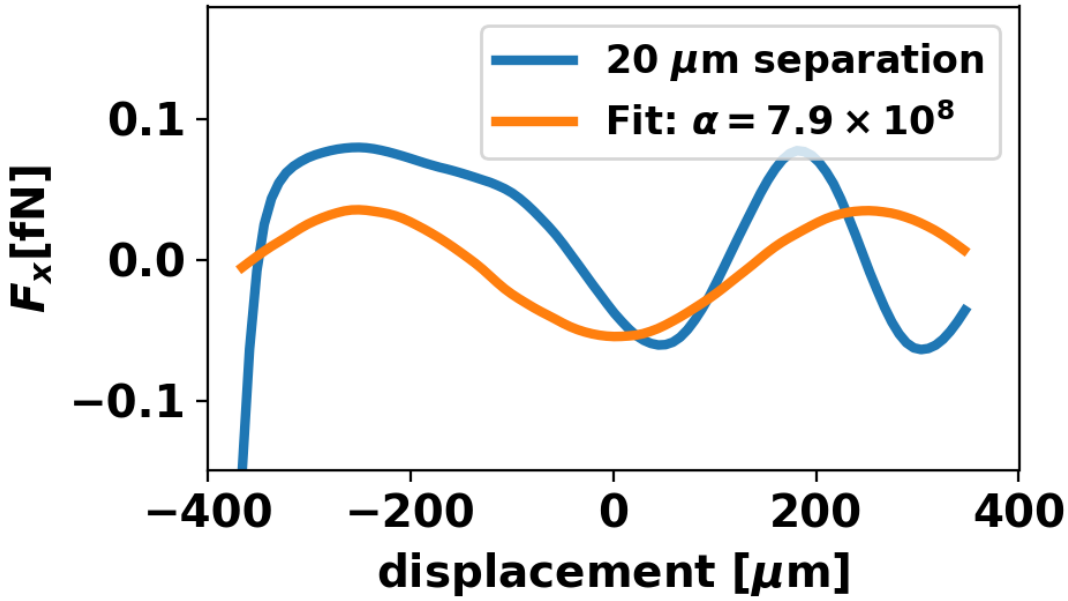

Figure 8.6: An example of a fit to a force template in the force versus displacement domain to the force in the x-direction to a microsphere separated from the end of the attractor by 20 μm at $\lambda = 25$ μm. The data and the template were linearly detrended before fitting. In practice, the 3-dimensional force was fit to determine the sensitivities as the value of α returned by the fit. Fitting in different domains with different background models did not produce substantially different results.

modulated by motion of the attractor.

To understand the nature of the background, measurements were taken without a microsphere in the trap over a range of laser frequencies with the attractor moving. The background was found to be modulated by the laser frequency as shown in Figure 8.10. As discussed in Ref. [17], the signal recorded by the electronics is the differences in electric field amplitudes on the segments of a quadrant photodiode. The effect of laser frequency modulation on the background with this difference signal is more complex than it would be for an individual detector.

The modulation for an individual detector can be understood as follows. With the phase sensitive optical measurement developed in Ref. [17], the signal generated

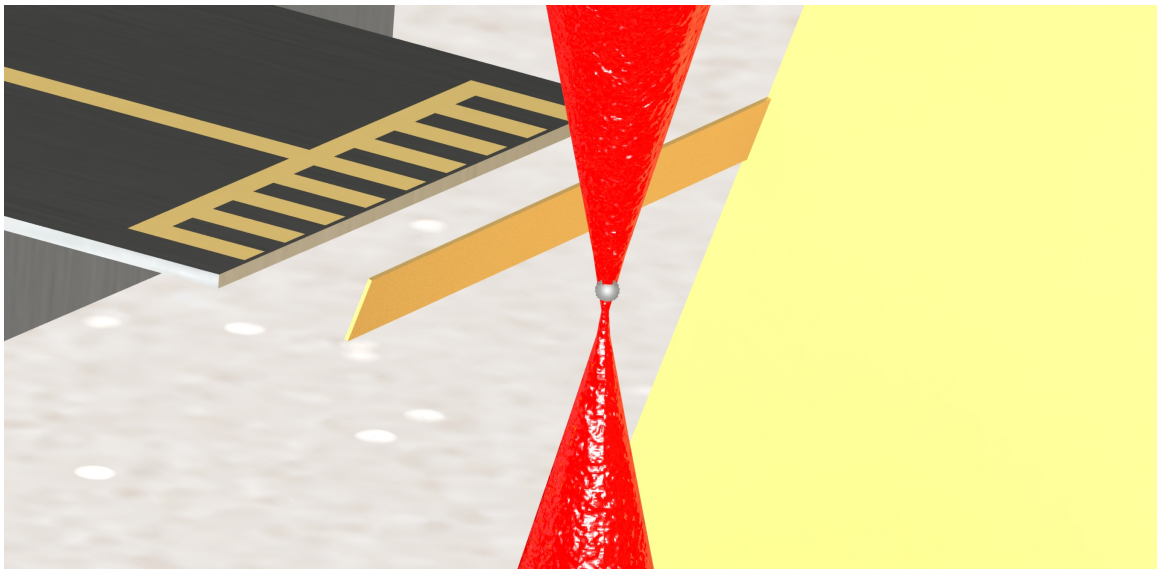

Figure 8.7: A rendering of the geometry of the freestanding shield placed in-between the microsphere and the end of the attractor. The freestanding shield reduced the electrostatic background, which resulted in an order of magnitude improvement in sensitivity. With the shield, the background was dominated by optical backgrounds due to stray light scattered by the attractor.

on the photodetector by a superposition of electric fields with differing optical path lengths (OPL) is proportional to the real part of the complex electric field $E(t) = \sum_{n=0} E_n \exp i(\Delta\omega t + OPL_n\omega_{opt}/c)$, where n indexes the source, c is the speed of light, ω_{opt} is the laser frequency, $\Delta\omega$ is the difference frequency defined in Ref. [17], and $\omega_{opt} = c/\lambda$ is the optical frequency when λ is the wavelength of the light. As the frequency of the laser, ω_{opt} is swept, different sources of light with different OPL will cause variations in the amplitude and phase of the electric field at the detector with a period of $2\pi c/OPL$ so that the $\sim$1 GHz period observed in Figure 8.10 indicates that a significant portion of the scattered light background has an optical path length difference of $\sim$30 cm from the main trapping beam.

The background from scattered light is the main challenge to overcome in order to reach the desired sensitivity. The current best sensitivity at $\lambda = 10$ μm is $\alpha \sim 10^4$. At a separation of 10 μm between the microsphere and the attractor, this corresponds

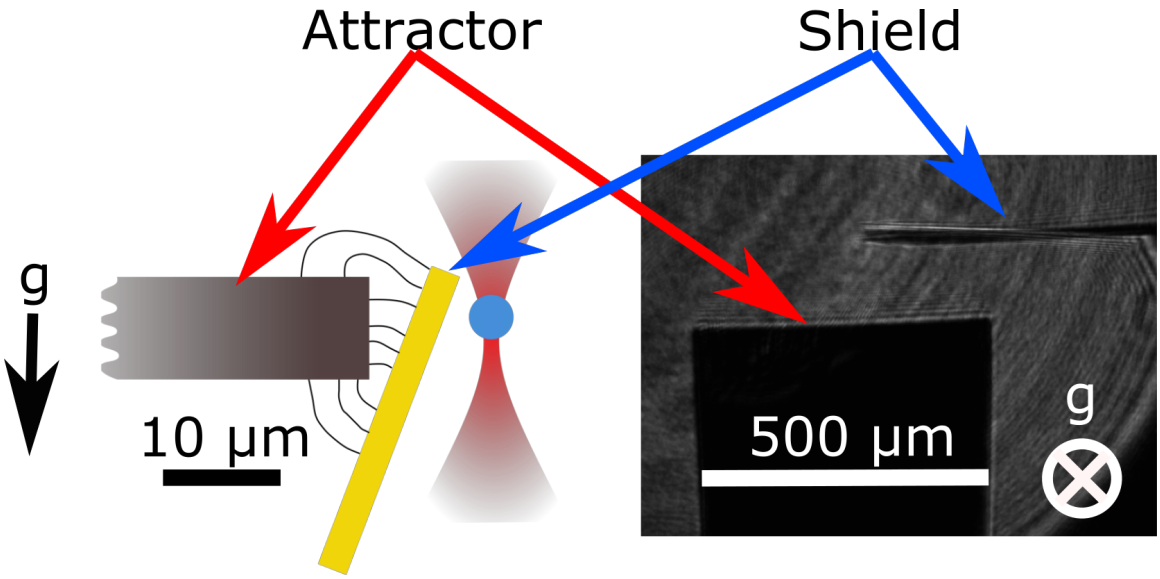

Figure 8.8: A side and a top-down cross-section of the geometry of the shield. The conducting shield terminated electric field lines sourced from the front face of the attractor reducing electrostatic backgrounds. With the shield positioned between the end of the attractor and the microsphere, the dominant background was caused by the attractor scattering stray light, rather than electrostatic backgrounds.

at a $F_{Yuk} \sim 10^{-20}$ N force on the microsphere. The optical background comparable to this is $\mathcal{P}_{opt} \sim cF_{Yuk} = 3$ pW, which is ∼1 ppb of the incident trapping beam. At this level, a ghost beam from 3 reflections off of a 0.1% wavelength specific anti-reflective coating could cause a significant background. Furthermore, a single 1 μm obstruction in a 1 mm beam will scatter $\sim$ 1 μm^2/1 mm^2 = 1ppm of the light. Even a 1% modulation of the light scattered by a single dust particle *could* cause a significant background.

There are two different mechanisms for optical backgrounds. Since the optical backgrounds observed here are present without a trapped microsphere, they are primarily caused by scattered light modulated by the motion of the attractor and detected by the imaging system. Improvements in imaging can reduce this background. At some level, scattered light may exert radiation pressure on the microsphere which could be modulated by the motion of the attractor. Radiation pressure backgrounds

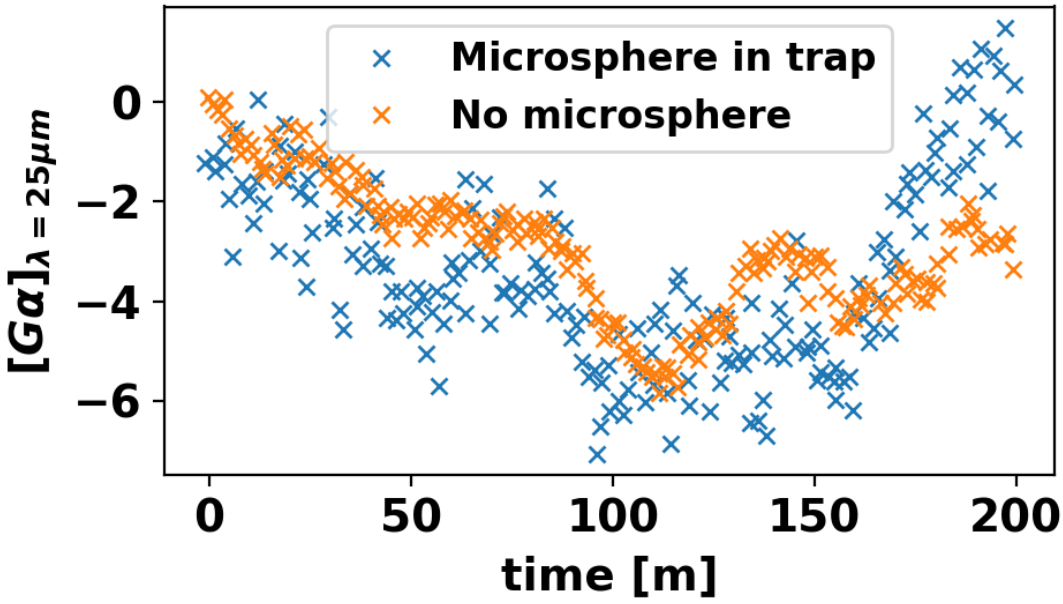

Figure 8.9: The fitted of α with $\lambda = 25$ μm in data with and without a microsphere in the trap. Since a similar background was measured with and without a microsphere in the trap, the background was attributed to stray light scattered by the attractor. Electrical interference was ruled out as a cause of the background because it was not present with the laser turned off.

can not be eliminated by improvements to the imaging alone.

8.4 Mitigation Techniques

There are techniques to reduce the effect of scattered light for measurements of micron length-scale interactions with optically levitated microspheres. One approach would be to use the frequency sweeping technique discussed here to discriminate between light with the same optical path length as the trapping beam and scattered light which has a different optical path length. This technique is equivalent to inverse Fourier transform spectroscopy, described in [177], where the known optical frequency is swept to measure a distance spectrum, rather than a known distance being swept to measure

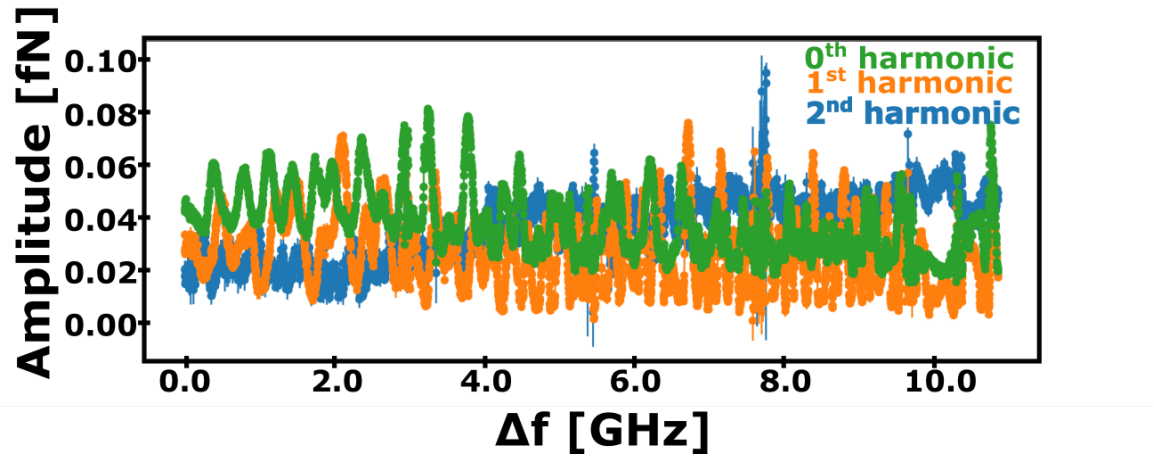

Figure 8.10: The amplitude of the first three Fourier components of the optical background versus changes in laser frequency, without a microsphere in the trap. The variation of the background with laser frequency indicates that it was caused primarily by scattered light which has a different optical path length than the main trapping beam. Technical limitations prevented this test from being carried out with a microsphere in the trap.

an optical frequency spectrum.

The laser frequency could be driven and the imaging electronics could lock into the modulation corresponding to the optical path length of the main trapping beam. Unfortunately, doing this in real time with bandwidth sufficient to maintain feedback would be difficult. The laser frequency needs to be swept over a wide range of frequencies because the minimum resolvable optical path length difference is given by $c/\Delta f$, where Δf is the laser tuning range. Implementation of this technique could require active measurement and closed loop actuation of the laser frequency.

Another technique that could mitigate the effect of scattered light would be to measure changes in the mechanical resonant frequency of the microsphere in the trap rather than direct force measurements. Changes in resonant frequency would be caused by any potential perturbing the underlying trap potential. A potential $V(r)$ with curvature $\partial^2 V/\partial r^2$ will modify the spring constant and cause a shift in the resonant frequency. This technique is commonly used in atomic force microscopy [178] and could potentially reduce the effect of scattered light picked up by the imaging

system. Unfortunately, frequency shift measurements would not help if scattered light applies radiation pressure to the microsphere. Frequency sensitive measurements are developed further in appendix C.

8.5 Concluding Remarks

The work presented here demonstrates development of techniques for manipulation and measurement with optically trapped particles. This includes the first demonstration of charge control in Ref. [46], the first measurement of the force between an optically levitated microsphere and a nearby object in Ref. [47], the development of a novel imaging technique in Ref. [17], demonstration of 3-dimensional force microscopy in Ref. [45], rotational control of optically levitated microspheres in Ref. [54], and a novel technique for measuring the mass of a microsphere in Ref. [166]. Although the techniques described here do not yet have competitive sensitivity to deviations from Newtonian gravity, improvements in the future may make it possible to reach unexplored parameter space.

A new system is currently under development with the goal of improving the sensitivity of optically levitated microspheres to gravitational interactions. Use of reflective rather than transmissive optics and construction in a clean room environment may reduce the amount of scattered light by reflections and dust particles. Improvements in the shield positioning and metrology may also help reduce backgrounds from scattered light and patch potentials. A careful analysis of noise sources could improve the sensitivity of the measurement and reduce the amount of time it takes to troubleshoot small backgrounds.

Appendix A

Attractor Fabrication

The following lists the process step for fabricating attractors as of 2/26/2019. A selection of SEM images are shown to reference what nominal devices look like at key points in the process.

- First litho step

    1) SRD SOI wafers in litho area
    2) 150C oven in litho area for (30mins).
    3) Run 2 dummnies on svgcoat track 2 20mins in 1.6um 3612 w/vp 2mm EBR on SVGcoat2
    4) Expose 1.5s for 15mW/cm2, 365nm with Mask1 hard contact 40um alignment gap
    5) Develop, bake #9 #2, develop#4 #2 (20mins)
    6) Descum with Drytek2 500W for 1mins, 150mT, O2 100sccm, 500W

- Gold finger trenches etch

    1) PT-DSE clean: clean the chamber with DSE clean with O2 for 30mins
    2) PT-DSE nano recipe 75 cycles. Check previous users for number cycles
    3) Enable wbflexcorr2 and bring bath up to temp

4) Rinse resist off with acetone, ipa, and methanol at wb solvent

5) Piranha clean, 120C 20 mins in bath at wbflexcorr-2

6) Rinse on wbflexcorr-2

7) SRD in litho area (10mins)

- Electrical isolation oxide

1) Grow 250nm thermal oxide at thermco 4. 60mins 950C wetox

2) Measure oxide thickness with nanospec

- Evaporation with innotech, TiAu 20nm/50nm

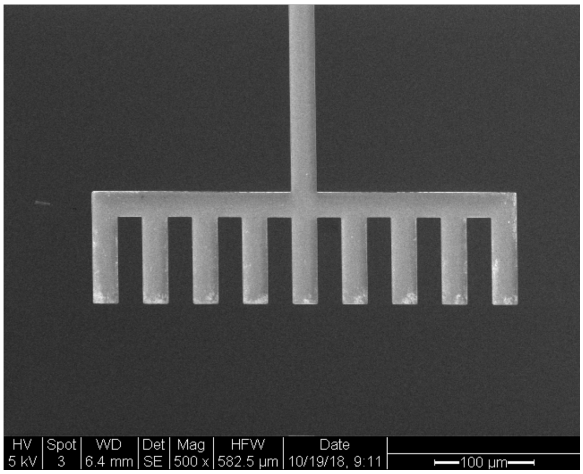

Figure A.1: An SEM image of an attractor structure after evaporating the gold seed layer and removing the seed layer from the un-trenched regions of the wafer by polishing the surface with chemical mechanical planarization (CMP). Some residual slurry is visible in this image. It was found that immediate sonication in detergent helped reduce the slurry residue left on the wafer.

- Chemical machine polish 1

1) CMP with 50,15,30, 80, 110, check every 60s until gold visually removed

2) Alternate rinsing with water and scrubbing with lint free wipe

3) Rinse with acetone, IPA and methanol in solvent bench in wafer sawing room

4) Sonicate in warm water and detergent

5) Ti etch on wbflexcorr-1 with 20 H2O: 1 H2O2(30%): 1 HF(49%), 20C, 1100nm/min for 4s (30mins)

6) Face down and sonicate on wbsolvent-1 for 15mins in DI water, high power.

7) SRD in litho area

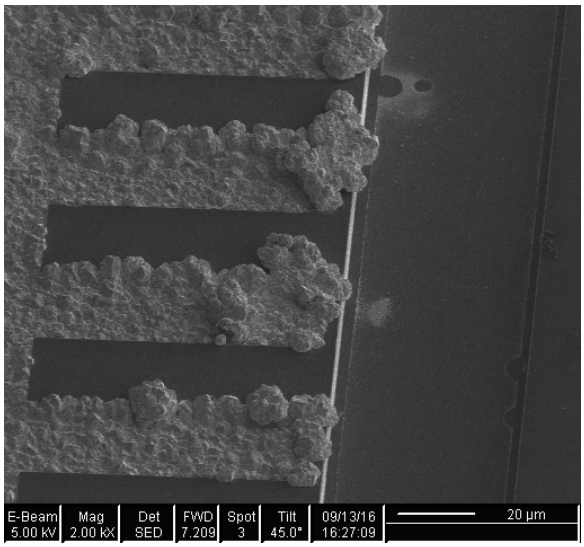

Figure A.2: An SEM image of initial attempts to electroform the gold fingers using a cyanide based hard gold plating solution. With the parameters we used the grain sizes were too large to form useful deposits. Better results were obtained with a sulfite based gold plating solution.

- Electroplating

1) Load wafer into fixture

2) check contact between pins and wafer

3) Filter the Sulfite plating solution (solution: Enthone BDT 510 Make-Up)

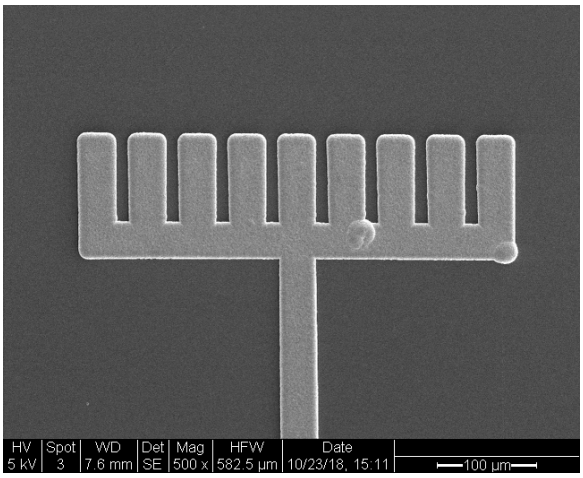

Figure A.3: An SEM image of the plating obtained with a gold sulfite based plating solution (Enthone BDT 510 Make-Up). The reduced grain size and improved uniformity of the deposits produced much smoother attractors after polishing.

4) Clean the plating jig: Sonicate for 10mins with wafer mounted, observe if dirt on surface. If so, take out everything and re filter again.
5) Assemble and test electronics
6) Check plating solution:
   a) pH 8.5 to 9.5
   b) Specific gravity 10 to 28 baume
   c) Adjust according to datasheet
7) plate dummy first (1h per wafer)
8) Physical parameters:
   a) Area of pattern: $0.029dm^2$
   b) estimate cathode area $0.06dm^2$
9) Parameters:
   a) Temp: 50C
   b) Voltage 0.4V
   c) stir bar not too fast

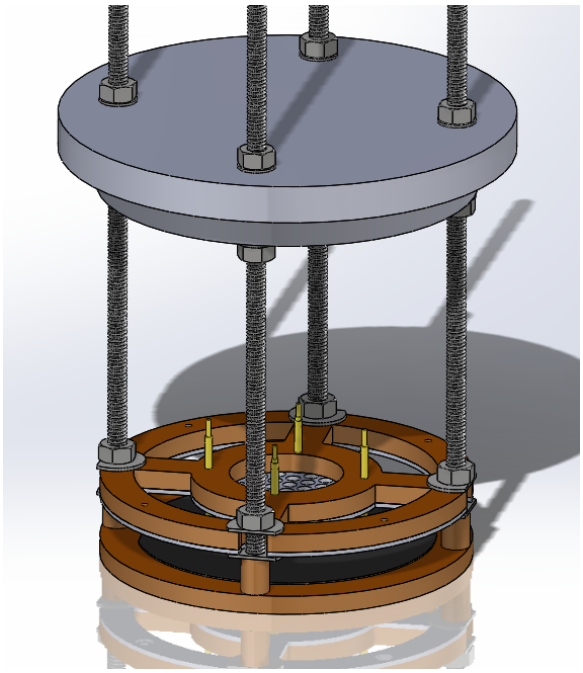

Figure A.4: A solidworks rendering of the fixture developed to produce uniform and repeatable gold plating deposits. Current was suppled to the front face of the wafer using gold plating contact pins. The plating solution was agitated by a magnetic stir bar syspended over the wafer.

d) 45mA forward current

e) 1KHz

f) 50

g) 90mins

10) Clean wafer in hot di water

11) Check with profilometer, optical microscope, and or SEM before proceeding to sample wafers (1h)

- Gold planarization

1) CMP Settings: 500, 30, 30, 200, 300, Time depends, check at 400s, and every 100s after that (3-5):1 DI to Slurry dilution seems to work well

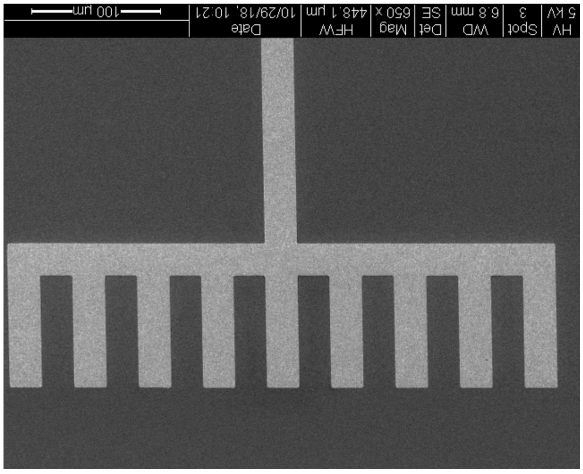

Figure A.5: An SEM image of an attractor after gold plating an planarization. The following steps defines the attractor on the top side of the wafer and releases the device by etching through the back of the wafer.

2) Finished polishing clearly visible under optical microscope

3) Keep polished wafers in DI in a beaker until cleaned with detergent

4) Sonicate in warm DI with 5-10 mL of detergent to remove slurry

5) Examine plating and polishing results under sem

6) Piranha on wbflexcorr-2 120C for 20mins

- Second lithography step

1) Spin rinse dry in litho area

2) Bake at 150C for 10mins

3) Coating 1.6um 3612 with Vapor Prime with 5mm EBR

4) Expose for 1.5sec with 345nm, vacuum contact

5) Develop 3612 1.5um recipe, Hardbake #9 #2, Develop #4 #2, recommend svgdev2

6) SRD in litho area

7) Descum with Drytek2 1min 500W, 100sccm 150 mTorr O2

8) Ox-rie descum v1.0 cpb (50 W, 50sccm, 150mTorr, 30s)
9) Oxford rie qdox etch
10) Start with 4 min, check for oxide
11) Continue with 60s intervals
12) DRIE chamber clean,
13) Nano recipee 75 cycles
14) Sonicate with Acetone(5min), Methanol(2min), Isopropanol(2min),
15) rinse on wbflexcorr-2
16) Pirhana clean wbflexcorr2 (120 C, 20min)
17) SRD in litho area
18) Bake at 110C for 10mins

- Backside oxide mask
  1) PECVD chamber clean with EP (tool: ccp-dep)
  2) PECVD backside SiO2 for 55mins Recipe: sio350-1
- Backside lithography
  1) Vapor prime on svg coater track 2 or yes oven
  2) Coat with 7um SPR220-7 no TOP EBR on track
  3) Recipe: 4 7.0um wo/VP 2mm EBR 200s Bake
  4) 7 μm thick 220-7: 4X 2.5s exposures, 120s wait, soft contact, better with karlsuss1
  5) Post exposure bake on svg developer
  6) Develop SPR220-7 on svgdev2
  7) Drytek2 1min 500W, 100sccm O2
- Plasma etch backside oxide hard mask

1) Oxford RIE QDOX etch 30mins per wafer
2) SVG coater - 2mm ebr only, 3 times (prior to DSE FAT)

- Backside etch through handle wafer

1) Use carbon dots to bond to backing wafer
2) Release etch
3) DSE clean 30mins
4) DSE FAT ETBTr 200cycles on dummy
5) DSE clean 5 min
6) Repeat until etched through
7) likely only twice, maybe 200 -> 100 -> 100 SOI
8) DSE FAT ETBTr 200cycles on sample
9) DSE clean 5 min
10) Repeat until etched through (buried oxide looks like thin window)
11) Check etch rate on alpha step (1um per cycle)

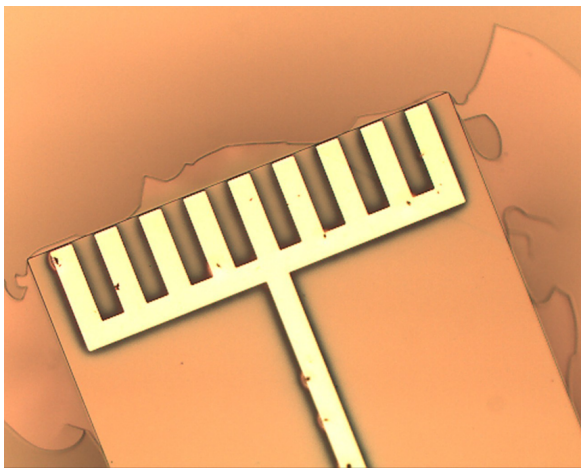

Figure A.6: An optical microscope image of a attractor before the penultimate step removes the buried oxide layer.

- Remove buried oxide

  1) with 1:10 HF for 20nm/s

  2) OR try ox-rie etch, maybe 5 min interval (15 min QD OXEtch works beautifully)

Appendix B

Yukawa Integral

A general Yukawa interaction leads to the interaction between two point masses given by

$$V(r) = \frac{-Gm_1m_2}{r}\left(1 + \alpha e^{-r/\lambda}\right) \tag{B.1}$$

where G is the gravitational constant, m_1 and m_2 are the respective point masses, α is the dimensionless strength of the interaction, and λ is the length scale of the interaction. The potential due to the Yukawa interaction between a r_b radius sphere of density ρ, and point mass m can be written as the integral

$$V(s, r_b, \rho) = m\rho \int_s^{s+2r_b} \int_0^{\pi} \int_0^{2\pi} V(r) r^2 \sin(\theta) d\phi d\theta dr \tag{B.2}$$

The geometry of this setup is shown in Figure B.1, where s is the separation between the point mass and the closest point on the surface of the sphere, and r_b is the radius of the sphere. Symmetry can be used to perform the integration over the ϕ and θ coordinates and sum up spherical caps weighted by $V(r)$.

The area of a spherical cap intersecting the sphere at a distance r from the point mass is given by

$$A(r) = r^2 \int_0^{\theta_{max}} \int_0^{2\pi} \sin(\theta) d\phi d\theta = 2\pi r^2\left(1 - \cos(\theta_{max})\right) \tag{B.3}$$

where θ_{max} is the maximum azimuthal angle at which the spherical cap centers on

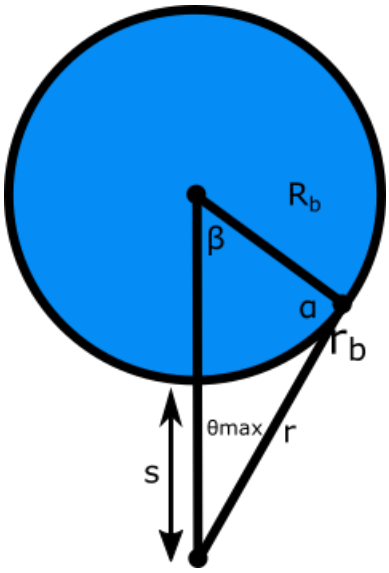

Figure B.1: The geometry for integrating a function that is constant of radius between a point and a sphere.

the point mass intersects the sphere. θ_{max} can be calculated from the law of cosines as

$$\theta_{max} = \arccos\left(\frac{(s+r_b)^2 + r^2 - r_b^2}{2r(s+r_b)}\right) \tag{B.4}$$

Inserting this into Equation B.3 we obtain

$$A(r) = \pi r \frac{(r-s)(s+2r_b-r)}{s+r_b} \tag{B.5}$$

so that we can write the total potential between a point mass and a sphere as

$$V(s, r_b, \rho) = m\rho \int_s^{s+r_b} V(r)A(r)dr. \tag{B.6}$$

To integrate over a Yukawa potential we note that

$$\int r^n e^r dr = \int [\partial_\beta^n e^{r\beta}]_{\beta=1} dr = [\partial_\beta^n \int e^{\beta r} dr]_{\beta=1} \tag{B.7}$$

For the relevant cases of $n = 1$ and $n = 3$ we have that

$$\int re^r dr = (r-1)e^r \tag{B.8}$$

and

$$\int r^3 e^r dr = (r^3 - 3r^2 + 6r - 6)e^r. \tag{B.9}$$

Now we can write that

$$V(s, r_b, \rho, \lambda, \alpha, m) = \frac{-Gm\rho}{r_b + s}\big(v(r_b) + 3/2\alpha e^{-s/\lambda} v(\lambda) f(r_b/\lambda)\big) \tag{B.10}$$

where

$$v(r) = 4/3\pi r^3 \tag{B.11}$$

and

$$f(r_b/\lambda) = e^{-2r_b/\lambda}(1 + r_b/\lambda) + r_b/\lambda - 1 \tag{B.12}$$

It is instructive to examine some limiting cases. In the limit $\alpha \to 0$ we see that $V \to \frac{-Gm_1m_2}{r}$ obtaining Newtonian gravity. In the limit $\alpha \gg 1$ and $r_b/\lambda \ll 1$, $f(r/\lambda) \to 2/3(r_b/\lambda)^3$ so $3/2v(\lambda)f(r_b/\lambda) \to v(r_b)$ and we get

$$V(s, r_b, \rho, \lambda, \alpha, m) \approx \alpha \frac{m\rho v(r_b) e^{-s/\lambda}}{r_b + s}. \tag{B.13}$$

Appendix C

Measuring Spring Constant Shifts

The sensor is a microsphere (MS), with mass m_{MS} in a harmonic potential with spring constant k:

$$V(x) = \frac{1}{2}kx^2 \tag{C.1}$$

Theories of modified gravity can also be written as potentials that modify the harmonic oscillator potential the MS experiences. Of particular interest are Yukawa type modifications at separations d from an attractor with mass m_{att}:

$$\Delta V(x,d) = \frac{-m_{MS}m_{att}G}{x+d}\big(1+\alpha\exp\left(-x+d\right)/\lambda\big) \tag{C.2}$$

Any perturbation $\Delta V(x)$, to the original harmonic oscillator potential can be written as a series expanded about $x = 0$:

$$\Delta V(x) = \Delta V(0) + \Delta V'(0)x + \frac{1}{2!}\Delta V''(0)x^2 + \mathcal{O}(x^3). \tag{C.3}$$

Adding a perturbation to the original potential and rearranging terms, the potential is modified to:

$$V_{mod}(x) = \Delta V(0) - \frac{\Delta V'(0)^2}{2(\Delta V''(0)+k)} + \frac{\Delta V''(0)+k}{2}\Big(x+\frac{\Delta V'(0)}{\Delta V''(0)+k}\Big)^2 + \mathcal{O}(x^3). \tag{C.4}$$

For terms up to second order in x, a harmonic oscillator potential with the zero of

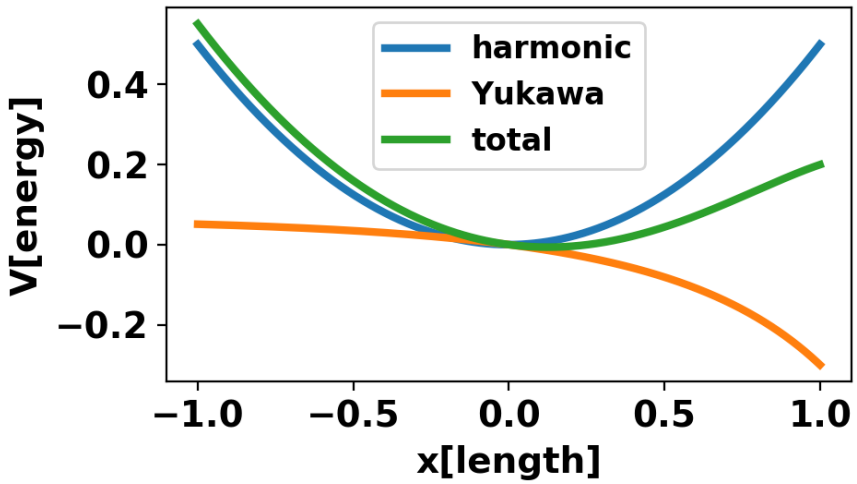

Figure C.1: A harmonic potential $V(x) = 1/2kx^2$ (blue), a modifying Yukawa potential $V_{mod}(x) = -\exp(-|x-2|)/(|x-2|)$ (orange). In this extreme case, the broadening of the harmonic potential can be seen from inspection.

potential energy shifted, the equilibrium position shifted by $\Delta x = \frac{\Delta V'(0)}{\Delta V''(0)+k}$, and the spring constant modified by $\Delta k = \Delta V''(0)$ is recovered. Measurements have focused on detecting the Δx caused by modification to the harmonic oscillator potential. What is the sensitive for the system described in this thesis that can be achieved by measuring changes to the effective spring constant caused by modified gravity?

The effect of adding a Yukawa perturbation to a harmonic potential is shown in figure C.1.

C.1 Measuring spring constant shifts

The best way to measure a change in the trap spring constant is to measure the corresponding change the resonant frequency. For fixed MS mass, m_{MS}, a change in the trap spring constant causes a change in the resonant frequency by an amount:

$$\Delta\omega_0 = \frac{\Delta k\omega_0}{2k} = \frac{\Delta k}{2m\omega_0} = \frac{\Delta V''(0)}{2m\omega_0} \tag{C.5}$$

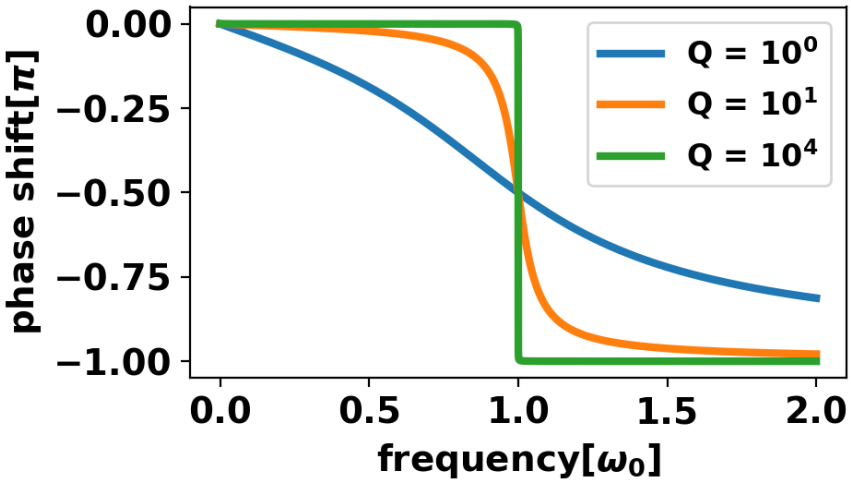

Figure C.2: The phase response of a harmonic oscillator for a range of Q. From the slope of this curve, it is clear that the best sensitivity to phase shifts and therefore resonant frequency shifts is obtained by stimulating the oscillator on resonance.

One way to measure spring constant shifts for a harmonic oscillator is to stimulate the oscillator with a sinusoidal driving force, $F(t) = F_0 \sin \omega t$ and measure shifts it the response of the oscillator $x(t) = A \sin(\omega t + \phi)$. The amplitude response of the oscillator to $F(t)$ is given by

$$A = \frac{F_0}{m\omega\sqrt{(\omega_0/Q)^2 + \frac{1}{\omega^2}(\omega_0^2 - \omega^2)^2}} \tag{C.6}$$

Where $Q = \frac{\sqrt{mk}}{c}$, with c being the damping force per unit velocity, is the Q factor for the oscillator. The phase response of the oscillator is given by

$$\phi = \arctan\left(\frac{\omega\omega_0}{Q(\omega^2 - \omega_0^2)}\right) \tag{C.7}$$

For experimental reasons, it is often easier to measure phase shifts rather than amplitude shifts. Differentiating the phase response with respect to the resonant

frequency we arrive at

$$\Delta\phi = \Delta\omega_0 \times \left(\frac{Q\omega(\omega^2+\omega_0^2)}{\omega^2\omega_0^2+Q^2(\omega^2-\omega_0^2)^2}\right) \tag{C.8}$$

Inspection of C.2 shows that the most sensitivity to resonant frequency shifts is obtained by driving on resonance. On resonance, we have that resonant frequency shifts can be determined by:

$$\Delta\omega_0 = \Delta\phi\frac{\omega_0}{2Q} \tag{C.9}$$

What is the sensitivity to phase changes? The uncertainty in the phase measurement of a tone is:

$$\sigma_\phi = \frac{\sigma_A}{\sqrt{2}A} \tag{C.10}$$

Our ability to measure phase shifts depends inversely on how hard the MS can be driven. It is unclear how hard this is. Let us assume that the MS can tolerate displacements around the size of the beam waist, $A_{max} \sim 1\mu m$. Inverting the expression for the amplitude on resonance, this corresponds to a driving force of $\frac{A_{max}m_{MS}\omega_0^2}{Q} \sim \frac{10^{-13}N}{Q}$. Our measured thermal force noise is $\sim 10^{-17}N/\sqrt{Hz}$. This gives a phase noise spectral density of $\sim Q10\mu rad/\sqrt{Hz}$

Putting everything together we can write our overall sensitivity to the second derivative of a perturbing potential:

$$\sigma_{V''} = 2m_{MS}\omega_0\sigma_{\omega_0} = m_{MS}\omega_0^2\sigma_\phi/Q \sim m_{ms}\omega_0^2 10\mu rad/\sqrt{Hz} \tag{C.11}$$

Since we are limited to drive amplitudes on the order of the size of the trap, the factor of Q dropps out.

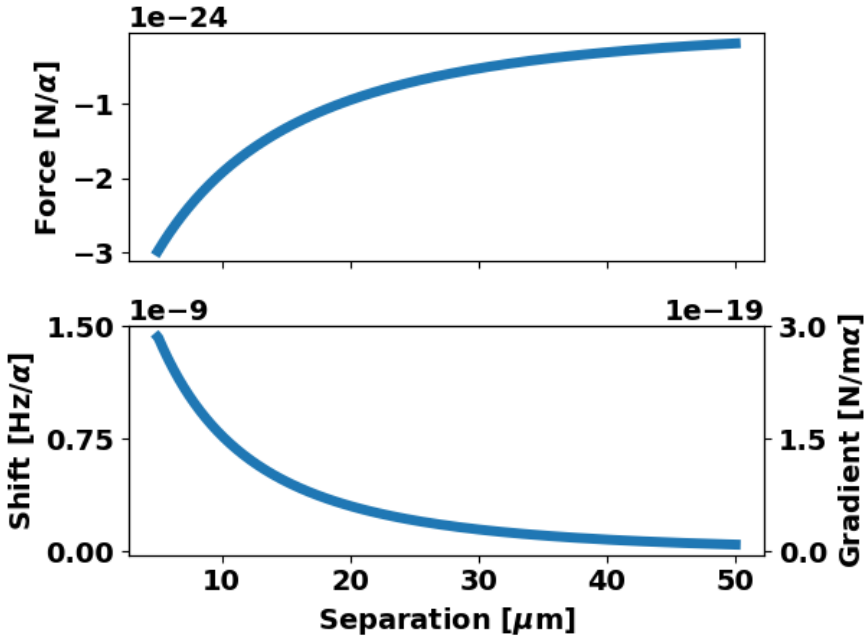

Figure C.3: Top: The force induced between the attractor structure described in chapter 8, and a 2.4-μm-radius 85 pg microsphere by a λ =25 μm Yukawa deviation as a function of separation. Bottom: The force gradient (right scale) an resonant frequency shift (left scale) caused by this perturbation for a 400 Hz trap.

C.2 The Second Derivative of the Yukawa potential from the Attractor

We can use our numerical integration of the attractor mass distribution to estimate the sensitivity of a measurement performed by measuring frequency shifts. The integration returns the force which is the first derivative of the potential. The Force for $\lambda = 25\mu m$ and $\alpha = 1$ versus separation in the plane of the attractor is shown at the top of figure C.3. The result of numerically differentiating this is shown in figure C.3. The inferred change in resonant frequency is shown in figure C.3. Our previous limits would have been equivalent to several Hz of frequency shift. The sensitivity inferred for two different separations with the numerically computed force gradients is shown in C.4 assuming $\sigma_{V''} = m_{ms}\omega_0^2 10\mu\text{rad}/\sqrt{Hz}$ and a $10^4 s$ integration.

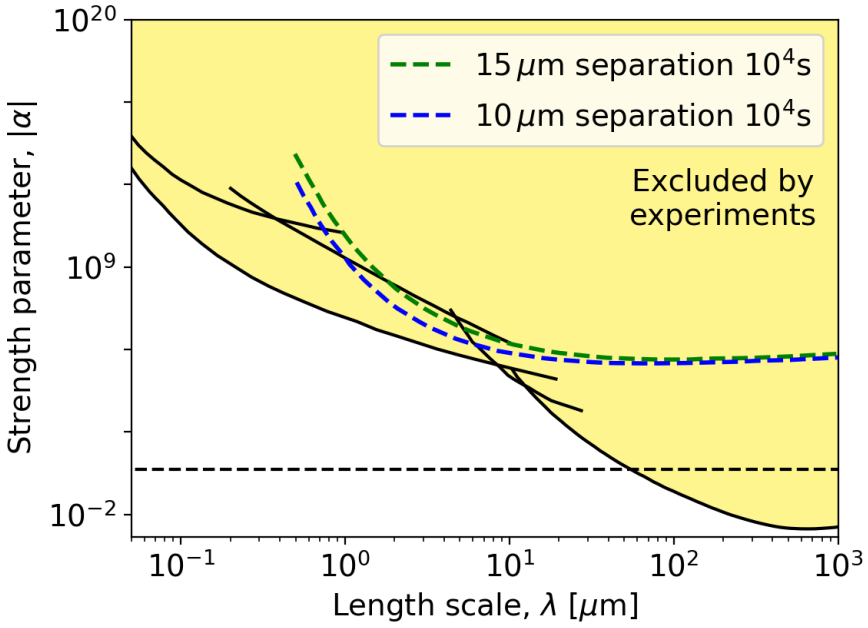

Figure C.4: The sensitivity to Yukawa deviation with the current noise and attractor for 10 μm and 15 μm minimum separations in a 10^4 s integration.

Appendix D

Feedback Implementation

As discussed in chapter 1, optical traps for μm-scale dielectric particles must be actively stabilized to operate at high vacuum. Feedback stabilizing a trapped particle requires an actuating force, a way of imaging displacements, and calculation of the appropriate feedback force for the microsphere. Optical actuation and imaging are discussed in chapter 1. Here I go into the details of our technique for calculating the feedback force digitally in a field programmable gate array (FPGA).

For the radial degrees of freedom, we only applied derivative feedback to replace the dissipation from residual gas, while the axial position was fixed with proportional, integral, and derivative feedback. For the $\sim$ 400 Hz trap resonant frequencies, we found that this required a feedback bandwidth $\gtrapprox$1 kHz to have a sufficient gain-bandwidth product to stabilize the trap. A block diagram showing the basic component of the feedback calculation is shown in Figure D.1.

The feedback sampling and calculation were performed with National Instruments 7854r FPGA card. The card had eight integrated ADCs and DACs that could sample at frequencies as high as 750 kHz. The card was housed inside a National Instruments PXI crate which provided power, a clock signal, and communication with a host computer. The feedback parameters shown in Figure D.1 could be adjusted in real time with a GUI on the host computer. Analog signals were passed to the card through a shielded twisted pair inside of a proprietary National Instruments cable.

Signal processing was performed on a Xilinx Vertex 5 LX110 FPGA. Although

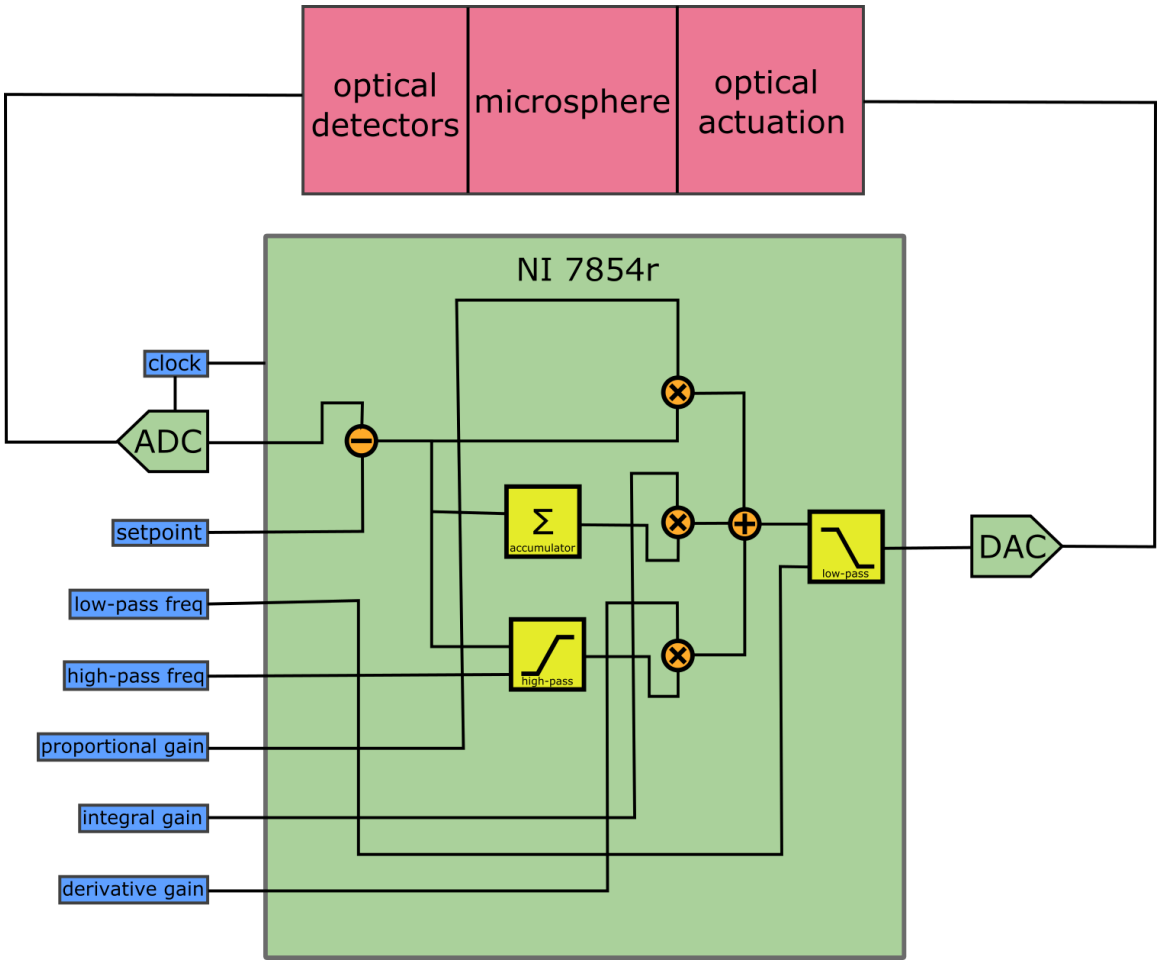

Figure D.1: A schematic representation of our implementation of PID feedback with a National Instruments 7854r FPGA card. The ADCs, DACs, and the FPGA for signal processing were integrated onto a single card in a national instruments PXI crate. Although the loops running the signal processing and DAC-ADC sampling operated at different clock rates, they were phase locked to the clock source provided by the PXI crate. The parameters of the feedback loop like gain and critical frequencies could be adjusted in real time from a GUI on the host computer controlling the PXI crate.

the development environment mostly obscured this detail from the user, this FPGA had sixty-four DSP48e slices which were important for efficient multiplication and digital filtering. The FPGA was programmed in LabView using a schematic interface

with predefined functions in a block diagram. The programming interface was easy to work with at first, but became cumbersome for more complex designs.

The ADCs and DACs integrated onto the card were nominally sixteen-bit. In practice, the noise from the ADCs limited them to $\sim$ 14.5 bits of information per sample. Smart designs would sample the ADCs at their full bandwidth and average down errors at the $\sim$ 1 kHz bandwidth required for the feedback. Oversampling by a factor of roughly 2^8 allowed us to average down errors by a factor of $\sqrt{2^8} = 2^4$ and in principle increase the precision to roughly $\sim$ 18.5 bits. The exact details of how the ADCs and DACs were sampled was opaque to the user using this hardware and development environment.

Data was read from the ADC as a signed sixteen-bit integer. To avoid loss of precision, this was cast to a thirty-two bit fixed point number for further computations. The first numerical operation was set-point subtraction from the value measured by the ADC to create an error signal. The proportional term for the feedback was then determined by multiplying the error term against the proportional gain value entered on the host computer. At times when FGPGA resources were limited, bit shifting was used in place of fixed point multiplication as an efficient way to scale by powers of 2.

Integral gain was calculated by passing the error signal into an accumulator and scaling the output like the the proportional gain. The integrator had no lower cutoff frequency to have an infinite gain at DC and pull the microsphere to the set point. The accumulator could be reset to avoid overflow when initiating feedback. The output of the accumulator was configured to saturate rather than wrap.

Derivative gain was implemented with a predefined first order Butterworth filter. This had the advantage that the derivative action could be rolled-off at a controllable frequency to avoid amplifying noise. The cutoff frequency of the Butterworth filter was adjusted in real time from the host computer to achieve sufficient gain-bandwidth for the feedback without amplifying high-frequency noise.

The final steps of the of the feedback calculation were to sum the different feedback terms together, a final low-pass filter stage, and a bit shift to convert the thirty-two-bit floating point number used for calculations into sixteen-bit signed integers. In

general, it was difficult to *a priori* determine the bits that should be sent to the DAC for controlling the actuators. The best solution we found was to use a bit shift that could be adjusted in real time to achieve the desired behavior.

Managing data types, numerical precision, and saturation with NI-FPGA was a challenge. Part of this challenge stems from the fact that it takes more than n bits to represent all possible results of a computation involving two or more n-bit numbers. The black-box LabView filter functions increased the number of output bits to avoid loss of precision. Since the LabView functions worked with relatively high precision numbers, they were resource intensive. The Vertex 5 LX110 FPGA could only support $\sim$10 first-order Butterworth filter blocks in a design.

Recombining the higher precision output of a filter block with other lower precision numbers and correctly casting them to sixteen-bit numbers for the DAC was a challenge. The preferences for LabView type casts allow the user to configure where bits are gained or lost and the saturation behavior when the result of the cast goes out of range. Outputs were configured to saturate rather than warp to avoid inverting the sign of the feedback. The LabView development environment supported simulation which could be useful for understanding these numerical issues.

D.1 Thoughts on NI FPGA Cards

The National Instruments FPGA cards were overall useful pieces of hardware under the right circumstances. The integration of eight ADCs, eight DACs, and an FPGA for signal processing onto a single card was easy to make work. Additionally, the schematic Labview programming language combined with a library of example code was useful for quickly creating a design that worked.

The disadvantage of using this national instruments product was that the details of the underlying implementation were opaque. For instance, the timing of the sampling of the ADCs and DACs was unknown and impossible to control. Although a design would specify that the ADCs or DACs would sample at the same time, there was an unknown delay between the sampling on the same order of magnitude as the sampling period. For frequencies much lower than the 750 kHz sampling frequency,

this contributed a negligible phase shift. However, for demodulating a carrier at a similar frequency to the sampling as in Ref. [17], or synthesizing a sin function at 10% of the DAC sampling frequency as in Ref. [54] this was more problematic.

Bibliography

[1] T. Li, S. Kheifets and M. G. Raizen, *Millikelvin cooling of an optically trapped microsphere in vacuum*, *Nature Physics* **7** (Mar, 2011) 527 EP –.

[2] *Henry cavendish (1731–1810): Experiments to determine the density of the earth*, *A Source Book in Geology, 1400–1900* . doi:10.4159/harvard.9780674180666.c26.

[3] T. A. Nieminen, V. L. Y. Loke, A. B. Stilgoe, G. Knöner, A. M. Brańczyk, N. R. Heckenberg et al., *Optical tweezers computational toolbox*, *Journal of Optics A: Pure and Applied Optics* **9** (jul, 2007) S196–S203. doi:10.1088/1464-4258/9/8/s12.

[4] T. Li, S. Kheifets and M. G. Raizen, *Millikelvin cooling of an optically trapped microsphere in vacuum*, *Nature Phys.* **7** (2011) 527–530, [1101.1283]. doi:10.1038/nphys1952.

[5] P. C. Kim, E. R. Lee, I. T. Lee, M. L. Perl, V. Halyo and D. Loomba, *Search for fractional-charge particles in meteoritic material*, *Phys. Rev. Lett.* **99** (Oct, 2007) 161804. doi:10.1103/PhysRevLett.99.161804.

[6] M. Marinelli and G. Morpurgo, *Searches of fractionally charged particles in matter with the magnetic levitation technique*, *Physics Reports* **85** (1982) 161 – 258. doi:https://doi.org/10.1016/0370-1573(82)90053-9.

[7] P. Hamilton, M. Jaffe, P. Haslinger, Q. Simmons, H. Müller and J. Khoury, *Atom-interferometry constraints on dark energy*, *Science* **349** (2015) 849–851, [1502.03888].

[8] B. Elder, J. Khoury, P. Haslinger, M. Jaffe, H. Müller and P. Hamilton, *Chameleon Dark Energy and Atom Interferometry*, 1603.06587.

[9] K. Li et al., *Neutron Limit on the Strongly-Coupled Chameleon Field*, *Phys. Rev. D* **93** (2016) 062001, [1601.06897]. doi:10.1103/PhysRevD.93.062001.

[10] H. Lemmel, P. Brax, A. N. Ivanov, T. Jenke, G. Pignol, M. Pitschmann et al., *Neutron Interferometry constrains dark energy chameleon fields*, *Phys. Lett. B* **743** (2015) 310–314, [1502.06023]. doi:10.1016/j.physletb.2015.02.063.

[11] T. Jenke et al., *Gravity Resonance Spectroscopy Constrains Dark Energy and Dark Matter Scenarios*, *Phys. Rev. Lett.* **112** (2014) 151105, [1404.4099]. doi:10.1103/PhysRevLett.112.151105.

[12] D. J. Kapner, T. S. Cook, E. G. Adelberger, J. H. Gundlach, B. R. Heckel, C. D. Hoyle et al., *Tests of the gravitational inverse-square law below the dark-energy length scale*, *Phys. Rev. Lett.* **98** (Aug, 2007) , [0611184].

[13] E. G. Adelberger, B. R. Heckel, S. A. Hoedl, C. D. Hoyle, D. J. Kapner and A. Upadhye, *Particle Physics Implications of a Recent Test of the Gravitational Inverse Sqaure Law*, *Phys. Rev. Lett.* **98** (2007) 131104, [hep-ph/0611223]. doi:10.1103/PhysRevLett.98.131104.

[14] A. Upadhye, *Dark energy fifth forces in torsion pendulum experiments*, *Phys. Rev. D* **86** (2012) 102003, [1209.0211]. doi:10.1103/PhysRevD.86.102003.

[15] C. C. Speake and C. Trenkel, *Forces between conducting surfaces due to spatial variations of surface potential*, *Phys. Rev. Lett.* **90** (Apr, 2003) 160403. doi:10.1103/PhysRevLett.90.160403.

[16] J. L. Garrett, D. Somers and J. N. Munday, *The effect of patch potentials in casimir force measurements determined by heterodyne kelvin probe force microscopy*, *Journal of Physics: Condensed Matter* **27** (2015) 214012.

[17] A. D. Rider, C. P. Blakemore, G. Gratta and D. C. Moore, *Single-beam dielectric-microsphere trapping with optical heterodyne detection*, *Phys. Rev. A* **97** (Jan, 2018) 013842. doi:10.1103/PhysRevA.97.013842.

[18] A. Cavalleri, G. Ciani, R. Dolesi, M. Hueller, D. Nicolodi, D. Tombolato et al., *Gas damping force noise on a macroscopic test body in an infinite gas reservoir*, *Physics Letters A* **374** (2010) 3365 – 3369. doi:https://doi.org/10.1016/j.physleta.2010.06.041.

[19] L. Martinetz, K. Hornberger and B. A. Stickler, *Gas-induced friction and diffusion of rigid rotors*, *Phys. Rev. E* **97** (May, 2018) 052112. doi:10.1103/PhysRevE.97.052112.

[20] Planotec and Pelcotec. [https://www.tedpella.com/calibration_html/SEM_Magnification_Calibration_Standards.htm].

[21] *Recherches théoriques et expérimentales sur la force de torsion et sur l'élasticité des fils de metal*, *Histoire de l'Académie Royale des Sciences* .

[22] G. Binnig, C. F. Quate and C. Gerber, *Atomic force microscope*, *Phys. Rev. Lett.* **56** (Mar, 1986) 930–933. doi:10.1103/PhysRevLett.56.930.

[23] LIGO Scientific Collaboration and Virgo Collaboration collaboration, B. P. e. a. Abbott, *Observation of gravitational waves from a binary black hole merger*, *Phys. Rev. Lett.* **116** (Feb, 2016) 061102. doi:10.1103/PhysRevLett.116.061102.

[24] A. Ashkin and J. M. Dziedzic, *Optical levitation by radiation pressure*, *Applied Physics Letters* **19** (1971) 283–285, [https://doi.org/10.1063/1.1653919]. doi:10.1063/1.1653919.

[25] D. J. Griffiths, *Introduction to electrodynamics*. Prentice Hall, 1999.

[26] A. Ashkin, J. M. Dziedzic, J. E. Bjorkholm and S. Chu, *Observation of a single-beam gradient force optical trap for dielectric particles*, *Opt. Lett.* **11** (May, 1986) 288–290. doi:10.1364/OL.11.000288.

[27] S. Chu, J. E. Bjorkholm, A. Ashkin and A. Cable, *Experimental observation of optically trapped atoms*, *Phys. Rev. Lett.* **57** (Jul, 1986) 314–317. doi:10.1103/PhysRevLett.57.314.

[28] A. Ashkin and J. Dziedzic, *Optical trapping and manipulation of viruses and bacteria*, *Science* **235** (1987) 1517–1520. doi:10.1126/science.3547653.

[29] K. G. Libbrecht and E. D. Black, *Toward quantum-limited position measurements using optically levitated microspheres*, *Physics Letters A* **321** (2004) 99 – 102. doi:https://doi.org/10.1016/j.physleta.2003.12.022.

[30] A. Arvanitaki and A. A. Geraci, *Detecting high-frequency gravitational waves with optically levitated sensors*, *Phys. Rev. Lett.* **110** (Feb, 2013) 071105. doi:10.1103/PhysRevLett.110.071105.

[31] M. S. Safronova, D. Budker, D. DeMille, D. F. J. Kimball, A. Derevianko and C. W. Clark, *Search for new physics with atoms and molecules*, *Rev. Mod. Phys.* **90** (Jun, 2018) 025008. doi:10.1103/RevModPhys.90.025008.

[32] A. A. Geraci, S. B. Papp and J. Kitching, *Short-range force detection using optically cooled levitated microspheres*, *Phys. Rev. Lett.* **105** (Aug, 2010) 101101. doi:10.1103/PhysRevLett.105.101101.

[33] Particle Data Group collaboration, K. A. Olive et al., *Review of Particle Physics*, *Chin. Phys. C* **38** (2014) 090001. doi:10.1088/1674-1137/38/9/090001.

[34] S. Dimopoulos and G. Giudice, *Macroscopic forces from supersymmetry*, *Physics Letters B* **379** (1996) 105 – 114.

[35] N. Arkani–Hamed, S. Dimopoulos and G. Dvali, *The hierarchy problem and new dimensions at a millimeter*, *Physics Letters B* **429** (1998) 263 – 272.

[36] Particle Data Group collaboration, C. Patrignani et al., *Review of Particle Physics*, *Chin. Phys.* **C40** (2016) 100001. doi:10.1088/1674-1137/40/10/100001.

[37] D. J. Kapner, T. S. Cook, E. G. Adelberger, J. H. Gundlach, B. R. Heckel, C. D. Hoyle et al., *Tests of the gravitational inverse-square law below the dark-energy length scale*, *Phys. Rev. Lett.* **98** (Jan, 2007) 021101. doi:10.1103/PhysRevLett.98.021101.

[38] A. A. Geraci, S. J. Smullin, D. M. Weld, J. Chiaverini and A. Kapitulnik, *Improved constraints on non-newtonian forces at 10 microns*, *Phys. Rev. D* **78** (Jul, 2008) 022002, [0802.2350]. doi:10.1103/PhysRevD.78.022002.

[39] A. O. Sushkov, W. J. Kim, D. A. R. Dalvit and S. K. Lamoreaux, *New experimental limits on non-newtonian forces in the micrometer range*, *Phys. Rev. Lett.* **107** (Oct, 2011) 171101, [1108.2547]. doi:10.1103/PhysRevLett.107.171101.

[40] Y.-J. Chen, W. K. Tham, D. E. Krause, D. López, E. Fischbach and R. S. Decca, *Stronger limits on hypothetical yukawa interactions in the 30–8000 nm range*, *Phys. Rev. Lett.* **116** (Jun, 2016) 221102. doi:10.1103/PhysRevLett.116.221102.

[41] C. P. Blakemore, A. D. Rider, S. Roy, A. Fieguth, A. Kawasaki, N. Priel et al., *Precision mass and density measurement of individual optically-levitated microspheres*, arXiv:1902.05481.

[42] F. Monteiro, S. Ghosh, A. G. Fine and D. C. Moore, *Optical levitation of 10-ng spheres with nano-g acceleration sensitivity*, *Phys. Rev. A* **96** (Dec, 2017) 063841. doi:10.1103/PhysRevA.96.063841.

[43] J. D. Jackson, *Classical electrodynamics*. Wiley, New York, NY, 3rd ed. ed., 1999.

[44] G. Mie, *Beiträge zur optik trüber medien, speziell kolloidaler metallösungen*, 1908.

[45] C. P. Blakemore, A. D. Rider, S. Roy, Q. Wang, A. Kawasaki and G. Gratta, *Three dimensional force-field microscopy with optically levitated microspheres*, 1810.05779.

[46] D. C. Moore, A. D. Rider and G. Gratta, *Search for millicharged particles using optically levitated microspheres*, *Phys. Rev. Lett.* **113** (Dec, 2014) 251801, [1408.4396]. doi:10.1103/PhysRevLett.113.251801.

[47] A. D. Rider, D. C. Moore, C. P. Blakemore, M. Louis, M. Lu and G. Gratta, *Search for screened interactions associated with dark energy below the* 100 μm *length scale*, *Phys. Rev. Lett.* **117** (Aug, 2016) 101101, [1604.04908]. doi:10.1103/PhysRevLett.117.101101.

[48] A. Ashkin and J. M. Dziedzic, *Optical levitation in high vacuum*, *Applied Physics Letters* **28** (1976) 333–335. doi:10.1063/1.88748.

[49] A. Ashkin and J. M. Dziedzic, *Feedback stabilization of optically levitated particles*, *Applied Physics Letters* **30** (1977) 202–204. doi:10.1063/1.89335.

[50] A. Ashkin and J. M. Dziedzic, *Stability of optical levitation by radiation pressure*, *Applied Physics Letters* **24** (1974) 586–588, [https://doi.org/10.1063/1.1655064]. doi:10.1063/1.1655064.

[51] T. Li, *An examination of keystroke dynamics for continuous user authentication*. PhD thesis, The University of Texas at Austin, 2013.

[52] P. Asenbaum, S. Kuhn, S. Nimmrichter, U. Sezer and M. Arndt, *Cavity cooling of free silicon nanoparticles in high vacuum*, *Nat. Commun.* **4** (Nov, 2013) 2743, [1306.4617]. doi:10.1038/ncomms3743.

[53] D. C. Moore, A. D. Rider and G. Gratta, *Search for Millicharged Particles Using Optically Levitated Microspheres*, *Phys. Rev. Lett.* **113** (2014) 251801, [1408.4396]. doi:10.1103/PhysRevLett.113.251801.

[54] A. D. Rider, C. P. Blakemore, A. Kawasaki, N. Priel, S. Roy and G. Gratta, *Electrically driven, optically levitated micro-gyroscopes*, 2018.

[55] B. Holdom, *Two u(1)'s and [U+03F5] charge shifts*, *Physics Letters B* **166** (1986) 196 – 198. doi:https://doi.org/10.1016/0370-2693(86)91377-8.

[56] D. Feldman, Z. Liu and P. Nath, *Stueckelberg $Z^{'}$ extension with kinetic mixing and millicharged dark matter from the hidden sector*, *Phys. Rev. D* **75** (Jun, 2007) 115001. doi:10.1103/PhysRevD.75.115001.

[57] S. D. McDermott, H.-B. Yu and K. M. Zurek, *Turning off the lights: How dark is dark matter?*, *Phys. Rev. D* **83** (Mar, 2011) 063509. doi:10.1103/PhysRevD.83.063509.

[58] X. Chu, T. Hambye and M. H. Tytgat, *The four basic ways of creating dark matter through a portal*, *Journal of Cosmology and Astroparticle Physics* **2012** (2012) 034.

[59] P. Langacker and G. Steigman, *Requiem for a fractionally charged, massive particle*, *Phys. Rev. D* **84** (Sep, 2011) 065040. doi:10.1103/PhysRevD.84.065040.

[60] S. Davidson, S. Hannestad and G. Raffelt, *Updated bounds on milli-charged particles*, *Journal of High Energy Physics* **2000** (2000) 003.

[61] A. D. Dolgov, S. L. Dubovsky, G. I. Rubtsov and I. I. Tkachev, *Constraints on millicharged particles from planck data*, *Phys. Rev. D* **88** (Dec, 2013) 117701. doi:10.1103/PhysRevD.88.117701.

[62] L. W. Jones, *A review of quark search experiments*, *Rev. Mod. Phys.* **49** (Oct, 1977) 717–752. doi:10.1103/RevModPhys.49.717.

[63] A. A. Prinz, R. Baggs, J. Ballam, S. Ecklund, C. Fertig, J. A. Jaros et al., *Search for millicharged particles at slac*, *Phys. Rev. Lett.* **81** (Aug, 1998) 1175–1178. doi:10.1103/PhysRevLett.81.1175.

[64] A. Badertscher, P. Crivelli, W. Fetscher, U. Gendotti, S. N. Gninenko, V. Postoev et al., *Improved limit on invisible decays of positronium*, *Phys. Rev. D* **75** (Feb, 2007) 032004. doi:10.1103/PhysRevD.75.032004.

[65] S. N. Gninenko, N. V. Krasnikov and A. Rubbia, *New limit on millicharged particles from reactor neutrino experiments and the pvlas anomaly*, *Phys. Rev. D* **75** (Apr, 2007) 075014. doi:10.1103/PhysRevD.75.075014.

[66] M. L. Perl, E. R. Lee and D. Loomba, *Searches for fractionally charged particles*, *Annual Review of Nuclear and Particle Science* **59** (2009) 47–65. doi:10.1146/annurev-nucl-121908-122035.

[67] G. S. LaRue, J. D. Phillips and W. M. Fairbank, *Observation of fractional charge of* $(\frac{1}{3})e$ *on matter*, *Phys. Rev. Lett.* **46** (Apr, 1981) 967–970. doi:10.1103/PhysRevLett.46.967.

[68] J. D. Phillips, W. M. Fairbank and J. Navarro, *Recent results in the search for fractional charge at stanford*, *Nuclear Instruments and Methods in Physics Research Section A: Accelerators, Spectrometers, Detectors and Associated Equipment* **264** (1988) 125 – 130. doi:https://doi.org/10.1016/0168-9002(88)91113-8.

[69] P. F. Smith, *Searches for fractional electric charge in terrestrial materials*, *Annual Review of Nuclear and Particle Science* **39** (1989) 73–111. doi:10.1146/annurev.ns.39.120189.000445.

[70] I. T. Lee, S. Fan, V. Halyo, E. R. Lee, P. C. Kim, M. L. Perl et al., *Large bulk matter search for fractional charge particles*, *Phys. Rev. D* **66** (Jul, 2002) 012002. doi:10.1103/PhysRevD.66.012002.

[71] D. C. Joyce, P. C. Abrams, R. W. Bland, R. T. Johnson, M. A. Lindgren, M. H. Savage et al., *Search for fractional charges in water*, *Phys. Rev. Lett.* **51** (Aug, 1983) 731–734. doi:10.1103/PhysRevLett.51.731.

[72] J. Van Polen, R. T. Hagstrom and G. Hirsch, *Search for fractional charges using droplet-jet techniques*, *Phys. Rev. D* **36** (Oct, 1987) 1983–1989. doi:10.1103/PhysRevD.36.1983.

[73] Z.-Q. YIN, A. A. GERACI and T. LI, *Optomechanics of levitated dielectric particles*, *International Journal of Modern Physics B* **27** (2013) 1330018, [https://doi.org/10.1142/S0217979213300181]. doi:10.1142/S0217979213300181.

[74] J. Gieseler, B. Deutsch, R. Quidant and L. Novotny, *Subkelvin parametric feedback cooling of a laser-trapped nanoparticle*, *Phys. Rev. Lett.* **109** (Sep, 2012) 103603. doi:10.1103/PhysRevLett.109.103603.

[75] N. Kiesel, F. Blaser, U. Delić, D. Grass, R. Kaltenbaek and M. Aspelmeyer, *Cavity cooling of an optically levitated submicron particle*, *Proceedings of the National Academy of Sciences* **110** (2013) 14180–14185, [https://www.pnas.org/content/110/35/14180.full.pdf]. doi:10.1073/pnas.1309167110.

[76] W. J. Atkinson, J. H. Young and I. A. Brezovich, *An analytic solution for the potential due to a circular parallel plate capacitor*, *Journal of Physics A: Mathematical and General* **16** (1983) 2837.

[77] K. C. Neuman and S. M. Block, *Optical trapping*, *Review of Scientific Instruments* **75** (2004) 2787–2809, [https://doi.org/10.1063/1.1785844]. doi:10.1063/1.1785844.

[78] J. L. Garbini, K. J. Bruland, W. M. Dougherty and J. A. Sidles, *Optimal control of force microscope cantilevers. i. controller design*, *Journal of Applied Physics* **80** (1996) 1951–1958, [https://doi.org/10.1063/1.363085]. doi:10.1063/1.363085.

[79] D. Vitali, S. Mancini, L. Ribichini and P. Tombesi, *Mirror quiescence and high-sensitivity position measurements with feedback*, *Phys. Rev. A* **65** (May, 2002) 063803. doi:10.1103/PhysRevA.65.063803.

[80] L. R. Rabiner and B. Gold, *Theory and application of digital signal processing*. Prentice-Hall, 1975.

[81] S. S. Wilks, *The large-sample distribution of the likelihood ratio for testing composite hypotheses*, *Ann. Math. Statist.* **9** (03, 1938) 60–62. doi:10.1214/aoms/1177732360.

[82] Supernova Search Team collaboration, A. G. Riess et al., *Observational evidence from supernovae for an accelerating universe and a cosmological constant*, *Astron. J.* **116** (1998) 1009–1038, [astro-ph/9805201]. doi:10.1086/300499.

[83] Supernova Cosmology Project collaboration, S. Perlmutter et al., *Measurements of Omega and Lambda from 42 high redshift supernovae*, *Astrophys. J.* **517** (1999) 565–586, [astro-ph/9812133]. doi:10.1086/307221.

[84] Planck collaboration, P. A. R. Ade et al., *Planck 2015 results. XIII. Cosmological parameters*, 1502.01589.

[85] B. Jain and J. Khoury, *Cosmological Tests of Gravity*, *Annals Phys.* **325** (2010) 1479–1516, [1004.3294]. doi:10.1016/j.aop.2010.04.002.

[86] A. Joyce, B. Jain, J. Khoury and M. Trodden, *Beyond the Cosmological Standard Model*, *Phys. Rept.* **568** (2015) 1–98, [1407.0059]. doi:10.1016/j.physrep.2014.12.002.

[87] S. R. Beane, *On the Importance of Testing Gravity at Distances Less Than 1cm*, *Gen. Rel. Grav.* **29** (Aug., 1997) 945–951, [hep-ph/9702419]. doi:10.1023/A:1018843607120.

[88] D. F. Mota and D. J. Shaw, *Strongly coupled chameleon fields: New horizons in scalar field theory*, *Phys. Rev. Lett.* **97** (2006) 151102, [hep-ph/0606204]. doi:10.1103/PhysRevLett.97.151102.

[89] E. G. Adelberger, J. H. Gundlach, B. R. Heckel, S. Hoedl and S. Schlamminger, *Torsion balance experiments: A low-energy frontier of particle physics*, *Prog. Part. Nucl. Phys.* **62** (2009) 102–134. doi:10.1016/j.ppnp.2008.08.002.

[90] W.-H. Tan, S.-Q. Yang, C.-G. Shao, J. Li, A.-B. Du, B.-F. Zhan et al., *New test of the gravitational inverse-square law at the submillimeter range with dual modulation and compensation*, *Phys. Rev. Lett.* **116** (Mar, 2016) 131101. doi:10.1103/PhysRevLett.116.131101.

[91] C. Burrage, E. J. Copeland and E. A. Hinds, *Probing Dark Energy with Atom Interferometry*, *JCAP* **1503** (2015) 042, [1408.1409]. doi:10.1088/1475-7516/2015/03/042.

[92] J. Khoury and A. Weltman, *Chameleon fields: Awaiting surprises for tests of gravity in space*, *Phys. Rev. Lett.* **93** (2004) 171104, [0309300]. doi:10.1103/PhysRevLett.93.171104.

[93] J. Khoury and A. Weltman, *Chameleon cosmology*, *Phys. Rev. D* **69** (2004) 044026, [0309411]. doi:10.1103/PhysRevD.69.044026.

[94] P. Brax, C. van de Bruck, A. C. Davis, J. Khoury and A. Weltman, *Chameleon Dark Energy*, *AIP Conf. Ser.* **736** (Nov., 2004) 105–110, [astro-ph/0410103]. doi:10.1063/1.1835177.

[95] D. E. Chang, C. A. Regal, S. B. Papp, D. J. Wilson, J. Ye, O. Painter et al., *Cavity opto-mechanics using an optically levitated nanosphere*, *Proc. Natl. Acad. Sci.* **107** (Jan., 2010) 1005–1010, [0909.1548]. doi:10.1073/pnas.0912969107.

[96] O. Romero-Isart, M. L. Juan, R. Quidant and J. I. Cirac, *Toward quantum superposition of living organisms*, *New J. of Phys.* **12** (Mar., 2010) 033015, [0909.1469]. doi:10.1088/1367-2630/12/3/033015.

[97] Z.-Q. Yin, A. A. Geraci and T. Li, *Optomechanics of Levitated Dielectric Particles*, *Int. J. Mod. Phys.* **B27** (2013) 1330018, [1308.4503]. doi:10.1142/S0217979213300181.

[98] J. Gieseler, B. Deutsch, R. Quidant and L. Novotny, *Subkelvin parametric feedback cooling of a laser-trapped nanoparticle*, *Phys. Rev. Lett.* **109** (Sep, 2012) 103603, [1202.6435]. doi:10.1103/PhysRevLett.109.103603.

[99] N. Kiesel, F. Blaser, U. Delic, D. Grass, R. Kaltenbaek and M. Aspelmeyer, *Cavity cooling of an optically levitated submicron particle*, *Proc. Natl. Acad. Sci.* **110** (Aug., 2013) 14180–14185, [1304.6679]. doi:10.1073/pnas.1309167110.

[100] G. Ranjit, D. P. Atherton, J. H. Stutz, M. Cunningham and A. A. Geraci, *Attonewton force detection using microspheres in a dual-beam optical trap in high vacuum*, *Phys. Rev. A* **91** (May, 2015) 051805, [1503.08799]. doi:10.1103/PhysRevA.91.051805.

[101] J. Millen, P. Z. G. Fonseca, T. Mavrogordatos, T. S. Monteiro and P. F. Barker, *Cavity cooling a single charged levitated nanosphere*, *Phys. Rev. Lett.* **114** (Mar, 2015) 123602, [1407.3595]. doi:10.1103/PhysRevLett.114.123602.

[102] P. Z. G. Fonseca, E. B. Aranas, J. Millen, T. S. Monteiro and P. F. Barker, *Nonlinear dynamics and millikelvin cavity-cooling of levitated nanoparticles*, 1511.08482.

[103] A. A. Geraci, S. B. Papp and J. Kitching, *Short-Range Force Detection Using Optically Cooled Levitated Microspheres*, *Phys. Rev. Lett.* **105** (Sept., 2010) 101101, [1006.0261]. doi:10.1103/PhysRevLett.105.101101.

[104] J. Gieseler, L. Novotny and R. Quidant, *Thermal nonlinearities in a nanomechanical oscillator*, *Nat. Phys.* **9** (Dec., 2013) 806–810, [1307.4684]. doi:10.1038/nphys2798.

[105] G. Ranjit, M. Cunningham, K. Casey and A. A. Geraci, *Zeptonewton force sensing with nanospheres in an optical lattice*, 1603.02122.

[106] A. Ashkin and J. M. Dziedzic, *Optical Levitation by Radiation Pressure*, *Appl. Phys. Lett.* **19** (Oct., 1971) 283–285. doi:10.1063/1.1653919.

[107] A. Ashkin, J. M. Dziedzic, J. E. Bjorkholm and S. Chu, *Observation of a single-beam gradient force optical trap for dielectric particles*, *Opt. Lett.* **11** (May, 1986) 288–290. doi:10.1364/OL.11.000288.

[108] S. S. Wilks, *The large-sample distribution of the likelihood ratio for testing composite hypotheses*, *Ann. Math. Statist.* **9** (03, 1938) 60–62. doi:10.1214/aoms/1177732360.

[109] G. Cowan, *Statistical Data Analysis*. Oxford science publications. Clarendon Press, 1998.

[110] A. I. Bishop, T. A. Nieminen, N. R. Heckenberg and H. Rubinsztein-Dunlop, *Optical Microrheology Using Rotating Laser-Trapped Particles*, *Phys. Rev. Lett.* **92** (May, 2004) 198104, [physics/0402021]. doi:10.1103/PhysRevLett.92.198104.

[111] G. J. Simpson, C. F. Wilson, K.-H. Gericke and R. N. Zare, *Coupled electrorotation: Two proximate microspheres spin in registry with an ac electric field*, *ChemPhysChem* **3** (2002) 416–423. doi:10.1002/1439-7641(20020517)3:5<416::AID-CPHC416>3.0.CO;2-K.

[112] J. Millen, T. Deesuwan, P. Barker and J. Anders, *Nanoscale temperature measurements using non-equilibrium Brownian dynamics of a levitated nanosphere*, *Nat. Nano.* **9** (June, 2014) 425–429, [1309.3990]. doi:10.1038/nnano.2014.82.

[113] A. I. Bishop, T. A. Nieminen, N. R. Heckenberg and H. Rubinsztein-Dunlop, *Optical microrheology using rotating laser-trapped particles*, *Phys. Rev. Lett.* **92** (May, 2004) 198104, [physics/0402021]. doi:10.1103/PhysRevLett.92.198104.

[114] D. S. E. jr., L. B. Pires, S. Umrath, D. Martinez, Y. Ayala, B. Pontes et al., *Probing the casimir force with optical tweezers*, *EPL* **112** (2015) 44001, [1511.02106].

[115] D. E. Chang, C. A. Regal, S. B. Papp, D. J. Wilson, J. Ye, O. Painter et al., *Cavity opto-mechanics using an optically levitated nanosphere*, *Proc. Nat. Acad. Sci. USA* **107** (Jan., 2010) 1005–1010, [0909.1548]. doi:10.1073/pnas.0912969107.

[116] J. Millen, P. Z. G. Fonseca, T. Mavrogordatos, T. S. Monteiro and P. F. Barker, *Cavity cooling a single charged levitated nanosphere*, *Phys. Rev. Lett.* **114** (Mar, 2015) 123602, [1407.3595]. doi:10.1103/PhysRevLett.114.123602.

[117] T. M. Hoang, Y. Ma, J. Ahn, J. Bang, F. Robicheaux, Z.-Q. Yin et al., *Torsional optomechanics of a levitated nonspherical nanoparticle*, *Phys. Rev. Lett.* **117** (Sep, 2016) 123604, [1605.03990]. doi:10.1103/PhysRevLett.117.123604.

[118] V. Jain, J. Gieseler, C. Moritz, C. Dellago, R. Quidant and L. Novotny, *Direct measurement of photon recoil from a levitated nanoparticle*, *Phys. Rev. Lett.* **116** (Jun, 2016) 243601, [1603.03420]. doi:10.1103/PhysRevLett.116.243601.

[119] D. Hempston, J. Vovrosh, M. Toroš, G. Winstone, M. Rashid and H. Ulbricht, *Force sensing with an optically levitated charged nanoparticle*, *Appl. Phys. Lett.* **111** (2017) 133111, [1706.09774]. doi:10.1063/1.4993555.

[120] O. Romero-Isart, M. L. Juan, R. Quidant and J. I. Cirac, *Toward quantum superposition of living organisms*, *New J. of Phys.* **12** (Mar, 2010) 033015, [0909.1469]. doi:10.1088/1367-2630/12/3/033015.

[121] R. Kaltenbaek, G. Hechenblaikner, N. Kiesel, O. Romero-Isart, K. C. Schwab, U. Johann et al., *Macroscopic quantum resonators (maqro)*, *Exp. Astron.* **34** (Oct, 2012) 123–164, [1201.4756]. doi:10.1007/s10686-012-9292-3.

[122] A. A. Geraci, S. J. Smullin, D. M. Weld, J. Chiaverini and A. Kapitulnik, *Improved constraints on non-newtonian forces at 10 microns*, *Phys. Rev. D* **78** (Jul, 2008) 022002. doi:10.1103/PhysRevD.78.022002.

[123] M. Mazilu, Y. Arita, T. Vettenburg, J. M. Auñón, E. M. Wright and K. Dholakia, *Orbital-angular-momentum transfer to optically levitated microparticles in vacuum*, *Phys. Rev. A* **94** (Nov, 2016) 053821. doi:10.1103/PhysRevA.94.053821.

[124] G. Ranjit, D. P. Atherton, J. H. Stutz, M. Cunningham and A. A. Geraci, *Attonewton force detection using microspheres in a dual-beam optical trap in high vacuum*, *Phys. Rev. A* **91** (May, 2015) 051805, [1503.08799]. doi:10.1103/PhysRevA.91.051805.

[125] G. Ranjit, M. Cunningham, K. Casey and A. A. Geraci, *Zeptonewton force sensing with nanospheres in an optical lattice*, *Phys. Rev. A* **93** (May, 2016) 053801, [1603.02122]. doi:10.1103/PhysRevA.93.053801.

[126] P. Z. G. Fonseca, E. B. Aranas, J. Millen, T. S. Monteiro and P. F. Barker, *Nonlinear dynamics and strong cavity cooling of levitated nanoparticles*, *Phys. Rev. Lett.* **117** (Oct, 2016) 173602, [1511.08482]. doi:10.1103/PhysRevLett.117.173602.

[127] J. Vovrosh, M. Rashid, D. Hempston, J. Bateman, M. Paternostro and H. Ulbricht, *Parametric feedback cooling of levitated optomechanics in a parabolic mirror trap*, *J. Opt. Soc. Am. B* **34** (Jul, 2017) 1421, [1603.02917]. doi:10.1364/JOSAB.34.001421.

[128] B. Laboratories. http://www.bangslabs.com/. Accessed: 2016-04-16.

[129] Nufern. http://www.nufern.com/pam/fiber_amplifiers/517/NUA-1064-PC-0010-A0/. Accessed: 2017-09-13.

[130] Orbits Lightwave. http://www.orbitslightwave.com/assets/pdf/Etherna_SlowLight_Lasers.pdf. Accessed: 2017-09-13.

[131] A. E. Siegman, *The antenna properties of optical heterodyne receivers*, *Proc. IEEE* **54** (Oct, 1966) 1350–1356. doi:10.1109/PROC.1966.5122.

[132] W. Schottky, *Über spontane stromschwankungen in verschiedenen elektrizitätsleitern*, *Ann. Phys. (Leipzig)* **362** (1918) 541–567. doi:10.1002/andp.19183622304.

[133] A. Ashkin, *Acceleration and trapping of particles by radiation pressure*, *Phys. Rev. Lett.* **24** (Jan, 1970) 156–159. doi:10.1103/PhysRevLett.24.156.

[134] F. Monteiro, S. Ghosh, E. C. van Assendelft and D. C. Moore, *Optical rotation of levitated spheres in high vacuum*, *Phys. Rev. A* **97** (May, 2018) 051802. doi:10.1103/PhysRevA.97.051802.

[135] R. Diehl, E. Hebestreit, R. Reimann, F. Tebbenjohanns, M. Frimmer and L. Novotny, *Optical levitation and feedback cooling of a nanoparticle at subwavelength distances from a membrane*, *Phys. Rev. A* **98** (Jul, 2018) 013851. doi:10.1103/PhysRevA.98.013851.

[136] Q. Wang, A. D. Rider, D. C. Moore, C. P. Blakemore, L. Cao and G. Gratta, *A density staggered cantilever for micron length gravity probing*, *Proc. IEEE ECTC* (June, 2017) 1773–1778. doi:10.1109/ECTC.2017.274.

[137] Q. A. Turchette, Kielpinski, B. E. King, D. Leibfried, D. M. Meekhof, C. J. Myatt et al., *Heating of trapped ions from the quantum ground state*, *Phys. Rev. A* **61** (May, 2000) 063418. doi:10.1103/PhysRevA.61.063418.

[138] G. H. Low, P. F. Herskind and I. L. Chuang, *Finite-geometry models of electric field noise from patch potentials in ion traps*, *Phys. Rev. A* **84** (Nov, 2011) 053425. doi:10.1103/PhysRevA.84.053425.

[139] J. Chiaverini, S. J. Smullin, A. A. Geraci, D. M. Weld and A. Kapitulnik, *New experimental constraints on non-newtonian forces below* 100 μm, *Phys. Rev. Lett.* **90** (Apr, 2003) 151101. doi:10.1103/PhysRevLett.90.151101.

[140] A. B. Churnside and T. T. Perkins, *Ultrastable atomic force microscopy: Improved force and positional stability*, *FEBS Lett.* **588** (Oct, 2014) 3621–3630. doi:10.1016/j.febslet.2014.04.033.

[141] F. Rossi and G. I. Opat, *Observations of the effects of adsorbates on patch potentials*, *Journal of Physics D: Applied Physics* **25** (1992) 1349.

[142] N. A. Robertson, J. R. Blackwood, S. Buchman, R. L. Byer, J. Camp, D. Gill et al., *Kelvin probe measurements: investigations of the patch effect with applications to st-7 and lisa*, *Classical and Quantum Gravity* **23** (2006) 2665.

[143] A. Arvanitaki and A. A. Geraci, *Detecting high-frequency gravitational waves with optically levitated sensors*, *Phys. Rev. Lett.* **110** (Feb, 2013) 071105. doi:10.1103/PhysRevLett.110.071105.

[144] D. Goldwater, B. A. Stickler, K. Hornberger and J. Millen, *Levitated electromechanics: all-electrical cooling of charged nano- and micro-particles*, 2018.

[145] O. Romero-Isart, A. C. Pflanzer, F. Blaser, R. Kaltenbaek, N. Kiesel, M. Aspelmeyer et al., *Large quantum superpositions and interference of massive nanometer-sized objects*, *Phys. Rev. Lett.* **107** (Jul, 2011) 020405. doi:10.1103/PhysRevLett.107.020405.

[146] O. Romero-Isart, *Quantum superposition of massive objects and collapse models*, *Phys. Rev. A* **84** (Nov, 2011) 052121. doi:10.1103/PhysRevA.84.052121.

[147] B. R. Slezak, C. W. Lewandowski, J.-F. Hsu and B. D'Urso, *Cooling the motion of a silica microsphere in a magneto-gravitational trap in ultra-high vacuum*, arXiv:1802.03424. doi:10.1088/1367-2630/aacac1.

[148] A. T. M. A. Rahman and P. F. Barker, *Laser refrigeration, alignment and rotation of levitated yb3+:ylf nanocrystals*, *Nature Photonics* **11** (2017) 634–638. doi:10.1038/s41566-017-0005-3.

[149] J. Ahn, Z. Xu, J. Bang, Y.-H. Deng, T. M. Hoang, Q. Han et al., *Optically levitated nanodumbbell torsion balance and ghz nanomechanical rotor*, *Phys. Rev. Lett.* **121** (Jul, 2018) 033603. doi:10.1103/PhysRevLett.121.033603.

[150] R. Reimann, M. Doderer, E. Hebestreit, R. Diehl, M. Frimmer, D. Windey et al., *Ghz rotation of an optically trapped nanoparticle in vacuum*, *Phys. Rev. Lett.* **121** (Jul, 2018) 033602. doi:10.1103/PhysRevLett.121.033602.

[151] S. Kuhn, A. Kosloff, B. A. Stickler, F. Patolsky, K. Hornberger, M. Arndt et al., *Full rotational control of levitated silicon nanorods*, *Optica* **4** (Mar, 2017) 356–360. doi:10.1364/OPTICA.4.000356.

[152] Y. Arita, A. W. McKinley, M. Mazilu, H. Rubinsztein-Dunlop and K. Dholakia, *Picoliter rheology of gaseous media using a rotating optically trapped birefringent microparticle*, *Analytical Chemistry* **83** (Dec, 2011) 8855–8858. doi:10.1021/ac2024365.

[153] Y. Arita, E. M. Wright and K. Dholakia, *Optical binding of two cooled micro-gyroscopes levitated in vacuum*, *Optica* **5** (Aug, 2018) 910–917. doi:10.1364/OPTICA.5.000910.

[154] Y. Arita, M. Mazilu and K. Dholakia, *Laser-induced rotation and cooling of a trapped microgyroscope in vacuum*, *Nature Communications* **4** (Aug, 2013) 2374 EP –.

[155] H. He, M. E. J. Friese, N. R. Heckenberg and H. Rubinsztein-Dunlop, *Direct observation of transfer of angular momentum to absorptive particles from a laser beam with a phase singularity*, *Phys. Rev. Lett.* **75** (Jul, 1995) 826–829. doi:10.1103/PhysRevLett.75.826.

[156] J. S. Bennett, L. J. Gibson, R. M. Kelly, E. Brousse, B. Baudisch, D. Preece et al., *Spatially-resolved rotational microrheology with an optically-trapped sphere*, *Scientific Reports* **3** (May, 2013) 1759 EP –.

[157] W. Li, N. Li, Y. Shen, Z. Fu, H. Su and H. Hu, *Dynamic analysis and rotation experiment of an optical-trapped microsphere in air*, *Appl. Opt.* **57** (Feb, 2018) 823–828. doi:10.1364/AO.57.000823.

[158] M. Rashid, M. Toroš, A. Setter and H. Ulbricht, *Precession motion in levitated optomechanics*, *Phys. Rev. Lett.* **121** (Dec, 2018) 253601. doi:10.1103/PhysRevLett.121.253601.

[159] W. Stöber, A. Fink and E. Bohn, *Controlled growth of monodisperse silica spheres in the micron size range*, *Journal of Colloid and Interface Science* **26** (1968) 62 – 69. doi:https://doi.org/10.1016/0021-9797(68)90272-5.

[160] P. Nagornykh, J. E. Coppock, J. P. J. Murphy and B. E. Kane, *Optical and magnetic measurements of gyroscopically stabilized graphene nanoplatelets levitated in an ion trap*, *Phys. Rev. B* **96** (Jul, 2017) 035402. doi:10.1103/PhysRevB.96.035402.

[161] M. E. J. Friese, T. A. Nieminen, N. R. Heckenberg and H. Rubinsztein-Dunlop, *Optical alignment and spinning of laser-trapped microscopic particles*, *Nature* **394** (Jul, 1998) 348 EP –.

[162] R. C. Jones, *A new calculus for the treatment of optical systems. description and discussion of the calculus*, *J. Opt. Soc. Am.* **31** (Jul, 1941) 488–493. doi:10.1364/JOSA.31.000488.

[163] Kurt Lesker. https://www.lesker.com/newweb/gauges/convection_kjlc_2.cfm. Accessed: 2018-12-19.

[164] M. Frimmer, K. Luszcz, S. Ferreiro, V. Jain, E. Hebestreit and L. Novotny, *Controlling the net charge on a nanoparticle optically levitated in vacuum*, *Phys. Rev. A* **95** (Jun, 2017) 061801. doi:10.1103/PhysRevA.95.061801.

[165] A. La Porta and M. D. Wang, *Optical torque wrench: Angular trapping, rotation, and torque detection of quartz microparticles*, *Phys. Rev. Lett.* **92** (May, 2004) 190801. doi:10.1103/PhysRevLett.92.190801.

[166] C. P. Blakemore, A. D. Rider, S. Roy, Q. Wang, A. Kawasaki and G. Gratta, *Three-dimensional force-field microscopy with optically levitated microspheres*, *Phys. Rev. A* **99** (Feb, 2019) 023816. doi:10.1103/PhysRevA.99.023816.

[167] O. Romero-Isart, A. C. Pflanzer, F. Blaser, R. Kaltenbaek, N. Kiesel, M. Aspelmeyer et al., *Large quantum superpositions and interference of*

massive nanometer-sized objects, *Phys. Rev. Lett.* **107** (Jul, 2011) 020405. doi:10.1103/PhysRevLett.107.020405.

[168] J. Chaste, A. Eichler, J. Moser, G. Ceballos, R. Rurali and A. Bachtold, *A nanomechanical mass sensor with yoctogram resolution*, *Nat. Nanotechnol.* **7** (Apr, 2012) 301.

[169] G. P. C. A. W. S. Francesco Ricci, Marc T. Cuairan and R. Quidant, *Accurate mass measurement of a levitated nanomechanical resonator for precision force sensing*, 1812.11645.

[170] T. A. Nieminen, V. L. Y. Loke, A. B. Stilgoe, G. Knöner, A. M. Brańczyk, N. R. Heckenberg et al., *Optical tweezers computational toolbox*, *J. Opt. A - Pure Appl. Op.* **9** (2007) S196.

[171] N. K. Pavlis, S. A. Holmes, S. C. Kenyon and J. K. Factor, *An earth gravitational model to degree 2160: Egm2008*, in *Gen. Assem. EGU*, (Vienna, Austria), April, 2008.

[172] F. Laermer and A. Schilp, *Method of anisotropic etching of silicon*, *US Patent 6 531 068* (Mar, 2003) .

[173] Corning Incorporated. [https://www.corning.com/].

[174] S. R. Parnell, A. L. Washington, A. J. Parnell, A. Walsh, R. M. Dalgliesh, F. Li et al., *Porosity of silica stöber particles determined by spin-echo small angle neutron scattering*, *Soft Matter* **12** (2016) 4709–4714. doi:10.1039/C5SM02772A.

[175] J. D. Jackson, *Classical Electrodynamics*. John Wiley & Sons, New York, 1962.

[176] I. H. Malitson, *Interspecimen comparison of the refractive index of fused silica∗,†*, *J. Opt. Soc. Am.* **55** (Oct, 1965) 1205–1209. doi:10.1364/JOSA.55.001205.

[177] T. Okamoto, S. Kawata and S. Minami, *Fourier transform spectrometer with a self-scanning photodiode array*, *Appl. Opt.* **23** (Jan, 1984) 269–273. doi:10.1364/AO.23.000269.

[178] S. Magonov, V. Elings and M.-H. Whangbo, *Phase imaging and stiffness in tapping-mode atomic force microscopy*, *Surface Science* **375** (1997) L385 – L391. doi:https://doi.org/10.1016/S0039-6028(96)01591-9.

Alexander Rider

Alexander Rider

I certify that I have read this dissertation and that, in my opinion, it is fully adequate in scope and quality as a dissertation for the degree of Doctor of Philosophy.

(Giorgio Gratta) Principal Adviser

I certify that I have read this dissertation and that, in my opinion, it is fully adequate in scope and quality as a dissertation for the degree of Doctor of Philosophy.

(Mark Kasevich)

I certify that I have read this dissertation and that, in my opinion, it is fully adequate in scope and quality as a dissertation for the degree of Doctor of Philosophy.

(John Fox)

Approved for the Stanford University Committee on Graduate Studies